Dissertation zur Erlangung des Doktorgrades
der Fakultät für Chemie und Pharmazie
der Ludwig-Maximilians-Universität München

Thin Films

from

Porous Nanoparticles

von

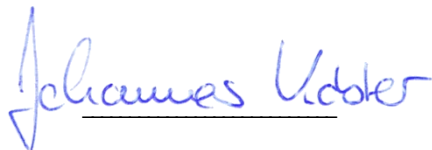Johannes Georg Kobler

aus

München

2008

Erklärung

Diese Dissertation wurde im Sinne von § 13 Abs. 3 der Promotionsordnung vom 29. Januar

1998 von Herrn Professor Dr. Thomas Bein betreut.

Ehrenwörtliche Versicherung

Diese Dissertation wurde selbstständig, ohne unerlaubte Hilfe erarbeitet.

München, am 5. 11. 2008

_____
(Unterschrift des Autors)

Dissertation eingereicht am: 10. 11. 2008

1. Gutachter: Prof. Dr. Thomas Bein

2. Gutachter: Prof. Dr. Konstantin Karaghiosoff

Mündliche Prüfung am: 08. 12. 2008

ABSTRACT

Porous materials in the nanometer range are interesting materials in many fields of science and technology. Especially in terms of colloidal suspensions, these materials are promising candidates for applications such as gas sensing, host-guest chemistry, drug delivery and coatings in the semiconductor industry. In this work, syntheses of monodisperse, stable, colloidal suspensions of different materials for the preparation of porous thin films were described.

Colloidal suspensions of zeolite Beta nanocrystals with low aluminum content were prepared and the crystallization kinetics was studied. The crystalline Beta was stabilized in colloidal suspensions by addition of inorganic silica-based binders and applied for the preparation of films by a spin-on process. The thickness of the films was controlled by repeated coating steps, speed of deposition and Beta concentration of the coating suspensions. The Beta films exhibit good mechanical properties, smooth surfaces and show a low refractive index, which is typical for highly porous silica based materials.

Additionally, a synthetic approach for the preparation of colloidal mesoporous silica spheres and functionalized colloidal suspensions of nanoscale mesoporous materials with high yields from concentrated solutions is presented. Narrow particle size distributions in the range of about 50 to 150 nm were established with Dynamic Light Scattering measurements and electron microscopy before and after template extraction. Discrete nanoscale mesoporous particles with functionalized pore surfaces resulted when adding functional organoalkoxysilanes directly to the initial silica precursor

solutions. Nitrogen sorption analysis indicated that the functional groups were located at the inner surfaces of the mesoporous channel systems.

By further decreasing the diameter of these mesoporous silica spheres, their scattering ability for visible light was also drastically decreased. We have demonstrated the synthesis of extremely small mesoporous silica nanoparticles via a specific co-condensation process with phenyl groups. If the size of the particles falls below about 1/10 of the wavelength of the incoming light ($0.1\ \lambda$), the colloidal suspensions show optical transparency. Because of an easy handling and a good reproducibility, the suspensions are ideal for the production of thin film by spin-coating. The films showed excellent optical qualities, exhibited good diffusion properties and a highly accessible pore system. Thanks to the small particle size and the resulting low surface roughness, the formation of multilayers was possible without transmitting defects on the surface with every following coating step. The availability of such homogeneous porous thin films made it possible to use ellipsometry as analysis method. Ellipsometric porosimetry (EP) is a convenient method to determine the effective porosity of a thin film on its original support without destroying it. It was possible to record sorption isotherms of the thin films with ellipsometry and to correlate the data with nitrogen sorption data of dried powders of the same material. The thin films showed very low refractive indices around 1.2 in the case of both, zeolites and functionalized mesoporous silica nanoparticles.

Besides, a synthesis procedure for TiO_2 particles in an acidic medium by a simple sol-gel process was investigated. The material showed a high surface area and the thin films

ABSTRACT _____

prepared from the colloidal suspensions had a high refractive index combined with a certain porosity. Thus, the preparation of wavelength specific Bragg mirrors could be realized by a simple and reproducible spin-coating approach using colloidal suspensions of functionalized porous silica nanoparticles and titania sols. The Bragg reflectors show a sensitivity towards specific relative pressures of organic vapors like isopropanol or toluene.

TABLE OF CONTENTS

TABLE OF CONTENTS

1. INTRODUCTION

Nanosystems are already playing a major role in information technology: the electronic components in computers and communication technology are becoming smaller and smaller. However, this development cannot go on forever, once the nanometer scale has been reached. At that level, novel physical phenomena often arise that may present potential problems for conventional uses – and an opportunity for innovations and new applications. Micro- and nanosystems are also becoming increasingly important in life science and medicine. They can be introduced into living organisms, for instance to bring a cancer medication to tumor cells. The increasing interest in this field can be illustrated by simply typing the four letters "nano" into the research discovery tool SciFinder and sort the publications in chronological order:
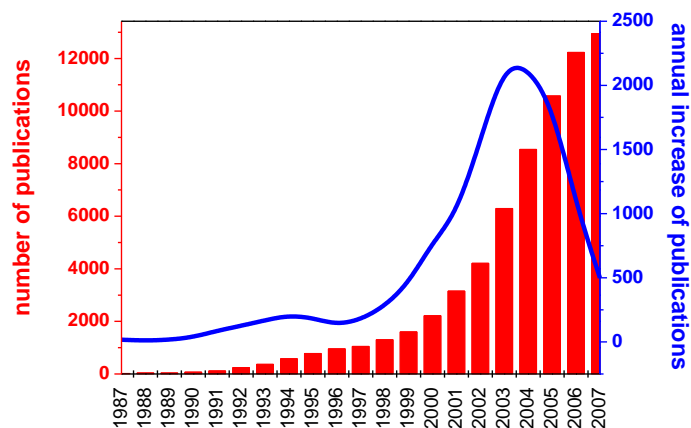
Fig. 1: Occurrence of the word "nano" in SciFinder from 1987 to 2007

Nanotechnology

One nanometer (nm) is one billionth, or 10^{-9} of a meter. For comparison, a DNA double-helix has a diameter around 2 nm and the smallest cellular life forms, the bacteria of the genus Mycoplasma, are around 200 nm in length. The term "nanotechnology" was defined by Tokyo Science University Professor Norio Taniguchi in 1974 as follows: "Nano-technology mainly consists of the processing of, separation, consolidation, and deformation of materials by one atom or by one molecule."[1] In the 1980s the basic idea of this definition was explored in much more depth by Dr. K. Eric Drexler, who promoted the technological significance of nano-scale phenomena and devices through speeches and books.[2, 3] The first distinguishing concepts in nanotechnology (but predating use of that term) were elaborated in "There's Plenty of Room at the Bottom", a talk given by physicist Richard Feynman at an American Physical Society meeting at Caltech on December 29, 1959. Feynman described a process by which the ability to manipulate individual atoms and molecules might be developed, using one set of precise tools to build and operate another proportionally smaller set, so on down to the needed scale. In the course of this, he noted, scaling issues would arise from the changing magnitude of various physical phenomena: gravity would become less important, surface tension and Van-der-Waals-attraction would become more important, etc.

Nanotechnology and nanoscience got started in the early 1980s. The driving force for nanotechnology came from a renewed interest in colloid science coupled with a new generation of analytical tools that allow observing and characterizing the materials or

devices even in the sub-nanometer domain. The invention of the scanning tunneling microscope (STM), the discovery of fullerenes in 1986 and carbon nanotubes a few years later as well as the synthesis of semiconductor nanocrystals (quantum dots) or the atomic force microscope (AFM) can be mentioned as milestones in the early years.

Nanotechnology today is a field of applied science and technology covering a broad range of topics. The main unifying theme is the control of matter on a scale smaller than one micrometer, normally approximately 1 to 100 nanometers, as well as the fabrication of devices of this size. It is a highly multidisciplinary enterprise, drawing from fields such as applied physics, materials science, colloid science, device physics, supramolecular chemistry, and mechanical and electrical engineering. Nanoscience can be seen as an extension of existing sciences into the nanoscale (or sometimes as a recasting of existing sciences using a newer, more modern term).

Two main approaches are used in nanotechnology. In the "top-down" approach, nano-objects are constructed from larger entities without atomic-level control. Many technologies originating from conventional solid-state silicon processing methods for fabricating microprocessors are capable of creating features much smaller than 100 nm, thus falling under the definition of nanotechnology. A complementary, and from a chemical point of view much more challenging strategy is the "bottom-up" approach. The materials and devices are built from molecular components or other nano-objects by an appropriate combination of driving forces such as molecular recognition, self-assembly, hydrogen bonding, etc.

Self-Assembly

Self-assembly can be defined as spontaneous and reversible organization of molecular units or other nano-objects into ordered structures by non-covalent interactions. The interactions responsible for the formation of the self-assembled system act on a strictly local level - in other words, the nanostructure builds itself.[4]

There are at least three features that distinguish self-assembly from common chemical reactions driving atoms and molecules to assemble into larger structures. First, the self-assembled structure must have a higher order than the isolated components. The second important aspect of self-assembly is the key role of weak interactions, e.g., Van-der-Waals-, capillary-, $\pi-\pi$-, or hydrogen bonds. The third distinctive feature is that the building blocks can be not only atoms and molecules, but span a wide range of nano- and mesoscopic structures, with different chemical compositions, shapes, and functionalities. Examples of self-assembly in materials science include the formation of colloidal crystals, lipid bilayers, phase-separated polymers, or self-assembled monolayers.

Another characteristic that is common to nearly all self-assembled systems is their thermodynamic stability. In covalent synthesis and polymerization, the scientist links atoms together in any desired conformation. In order for self-assembly to take place without the intervention of external forces, the process must lead to a lower Gibbs energy, thus self-assembled structures are thermodynamically more stable than the single, un-assembled components. A direct consequence is the general tendency of self-assembled structures to be relatively free of defects.

By choosing precursors with suitable physicochemical properties, it is possible to exert a fine control on the formation processes in order to obtain complex architectures. Popular examples for such self-organizing units are surfactant micelles - aggregates of surface-active molecules dispersed in a liquid.
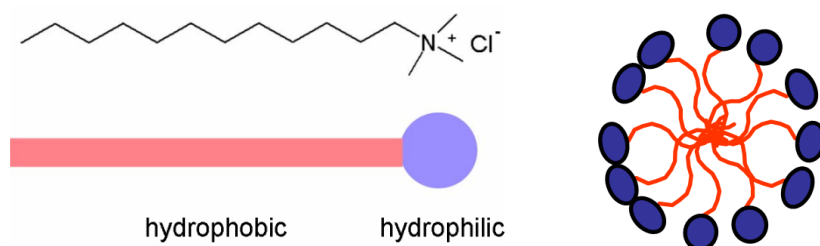
Fig. 2: Surfactant molecule and micelle

A typical micelle in aqueous solution forms an aggregate with the hydrophilic "head" regions in contact with surrounding solvent, sequestering the hydrophobic tail regions in the micelle centre. The shape and size of a micelle is a function of the molecular geometry of its surfactant molecules and solution conditions, such as surfactant concentration, temperature, pH, and ionic strength. Such micelles are already simple examples for nano-objects.

Nanoparticles

Nanoparticles are often defined as microscopic particles with at least one dimension less than 100 nm. A nanoscopic film, for example, has vertical dimensions in the range of 0.1–100 nm according to the IUPAC definition.[5] Due to a wide variety of potential applications in biomedical, optical, and electronic fields, nanoparticles are of great

scientific interest as they are effectively a bridge between bulk materials and atomic or molecular structures.

A bulk material should have constant physical properties regardless of its size, but a number of physical phenomena can noticeably change as the size of the system decreases. The properties of materials change as their size approaches the nanoscale and as the percentage of atoms at the surface of a material becomes significant. These include quantum mechanical effects, for example, the "quantum size effect" where the electronic properties of solids are altered with great reductions in particle size. This effect does not come into play by going from macro to micro dimensions, but it does become dominant when the nanometer size range is reached.

Additionally, a number of physical properties change when compared to macroscopic systems, thus enabling unique applications. For instance, the melting point of gold is shifted to lower temperatures.[6] Much of the fascination with nanoscience stems from these unique quantum and surface phenomena that matter exhibits at the nanoscale.

A unique aspect of nanoscience is the vastly increased ratio of surface area to volume present in many nanoscale materials that opens new possibilities in surface-based science, such as catalysis. Colloid science has given rise to many materials that may be useful in nanotechnology, for instance, carbon nanotubes and nanometer-sized metal oxide particles. At the small end of the size range, nanoparticles are often referred to as clusters. Metal, dielectric, and semiconductor nanoparticles have been formed, as well as hybrid structures, e.g., core-shell particles. Nanoparticles made of semiconducting material may also be labeled quantum dots if they are small enough (typically sub

10 nm) for quantization of electronic energy levels to occur. Such nanoscale particles are used in biomedical applications, e.g., as imaging agents. Semi-solid and soft nanoparticles have been manufactured. A prototype nanoparticle of semi-solid nature is represented by the liposomes. Various types of liposomes or other types of porous nanoparticles are currently explored clinically as delivery systems for anticancer drugs and vaccines.[7, 8]

But nanoparticles also present possible dangers, both medically and environmentally. Most of these are due to the high surface to volume ratio, which can make the particles very reactive or catalytically active. They may also be able to pass through cell walls in organisms, and their interactions with the body are relatively unknown. However, free nanoparticles in the environment quickly tend to agglomerate and thus leave the nano-regime, and nature itself presents many nanoparticles to which organisms on earth may have evolved immunity, such as terpenes from plants[9] or dust from volcanic eruptions.

Colloid Science

As mentioned above, much of the knowledge in today's nanoscience derives from colloidal science. Sol-gel chemistry, for example, is a typical "bottom-up" approach. The Scottish scientist Thomas Graham introduced this field of study in 1861. Many familiar substances, including butter, milk, smoke, paints, and glues are colloids.

A colloid or colloidal dispersion is a type of homogeneous mixture. It consists of two separate phases: a dispersed phase and a continuous phase; the dispersed phase is made of very small particles or droplets that are distributed evenly throughout the continuous

phase. According to IUPAC, the size of the dispersed phase particles is between 1 and 1000 nm in at least one dimension. Homogeneous mixtures with a dispersed phase in this size range may be called colloidal aerosols, colloidal emulsions, colloidal foams, colloidal dispersions or hydrosols. The dispersed particles or droplets are largely affected by the surface chemistry present in the colloid. Homogeneous suspensions of nanoparticles are possible if the interaction of the particle surface with the solvent is strong enough to overcome differences in density, which usually result in a material either sinking or floating in a liquid.

Fig. 3 shows the free energy E as a function of the particle distance r. (k_B = Boltzmann constant, T = absolute temperature). The free energy reaches its minimum when the particle distance $r = \delta$. This approach is only possible if the energy barrier ΔE_c is of the same order of magnitude as the thermal energy $k_B T$; in this case the dispersion is kinetically unstable. In contrast, in case of a stable colloidal dispersion the energy barrier is so high that the particles can not converge enough to coagulate.
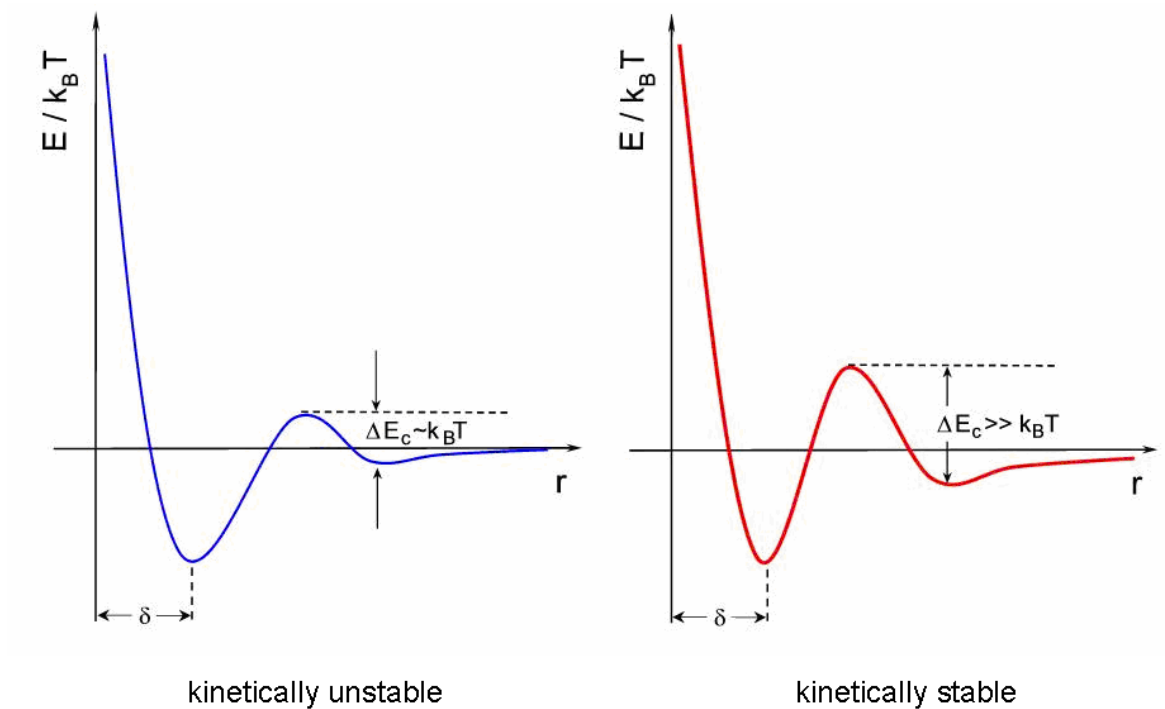
Fig. 3: Kinetic stability of colloidal dispersions

The following forces play an important role in the interactions of colloid particles and thus the height of the energy barrier:

Excluded volume repulsion: This refers to the impossibility of any overlap between hard particles.

Electrostatic interaction: Colloidal particles often carry an electrical charge (zeta potential) and therefore attract or repel each other. The charges of both the continuous and the dispersed phase, as well as the mobility of the phases are factors affecting this interaction.

Van-der-Waals-forces: This is due to interactions between two dipoles that are either permanent or induced. Even if the particles do not have a permanent dipole, fluctuations of the electron density give rise to a temporary dipole in the particle. This temporary dipole induces a dipole in particles nearby. The temporary dipole and the induced dipoles are then attracted to each other.

Entropic forces: According to the second law of thermodynamics, a system progresses to a state in which entropy is maximized.

Steric forces between polymer-covered surfaces or in solutions containing non-adsorbing polymer can modulate interparticle forces, producing an additional repulsive steric stabilization force or attractive depletion force between them.

The two main mechanisms to prevent colloids from aggregating are steric stabilization and electrostatic stabilization. Electrostatic stabilization is based on the mutual repulsion of like electrical charges. Different phases generally have different charge affinities, so that a double-layer of charges forms at any interface. Small particle sizes lead to enormous surface areas, and this effect is greatly amplified in colloids. In a stable colloid, the mass of the individual particles in a dispersed phase is so low that their kinetic energy is too small to overcome their electrostatic repulsion.

Unstable colloidal dispersions form flocks as the particles aggregate due to interparticle attractions. This can be accomplished by different methods:

Adding salts or solvents to a suspension or changing the pH of a suspension to effectively neutralize the surface charge of the dispersed particles can accomplish removal of the electrostatic barrier that prevents aggregation of the particles. This removes the repulsive forces that keep colloidal particles separate and allows for coagulation due to Van-der-Waals-forces.

Addition of a charged polymeric flocculant can bridge individual colloidal particles by attractive electrostatic interactions. For example, negatively charged colloidal silica particles can be flocculated by the addition of a positively charged polymer.

A stable colloidal suspension often appears opalescent because of the Tyndall effect, which is the scattering of light by particles in the colloid. By decreasing the size of the dispersed particles, their ability to scatter light is also decreased.

Fabrication of Nanoparticles

There are several methods for creating nanoparticles. In attrition, macro or micro scale particles are ground in a ball mill, a planetary ball mill, or other size reducing mechanism. But the minimum particle size is strongly limited. In pyrolysis, an organic precursor (liquid or gas) is forced through a nozzle at high pressure and burned. Thermal plasma can also deliver the energy necessary to cause evaporation of small micrometer size particles. The thermal plasma temperatures are at the order of 10000 K, such that a solid powder easily evaporates. Nanoparticles are formed upon cooling

while exiting the plasma region. The radio frequency induction plasma method has been used to synthesize, for example, various ceramic nanoparticles. In sol-gel chemistry, smaller components are arranged into more complex assemblies.[10, 11]

Sol-gel Chemistry

The sol-gel process is a wet-chemical technique for the fabrication of materials, typically a metal oxide, starting from a chemical solution containing colloidal precursors (sol). Typical precursors are metal alkoxides and metal chlorides, which undergo hydrolysis and polycondensation reactions to form a colloid. The sol evolves then towards the formation of an inorganic network containing a liquid phase (gel). A well-known synthesis in sol-gel chemistry is the Stöber process,[12] in which the silica precursor is hydrolyzed in a solution of ammonia, water, and an alcohol.

Precursor Chemistry

Very common precursors in silicate chemistry are tetraalkoxysilanes, because the released alcohols usually have no negative effects on the reaction and can be removed easily. The precursor can hydrolyze in an either acidic or basic aqueous medium and afterwards condense to an inorganic network of amorphous silica. The concepts shown in Fig. 4 can help to control the size and morphology of the synthesized particles.
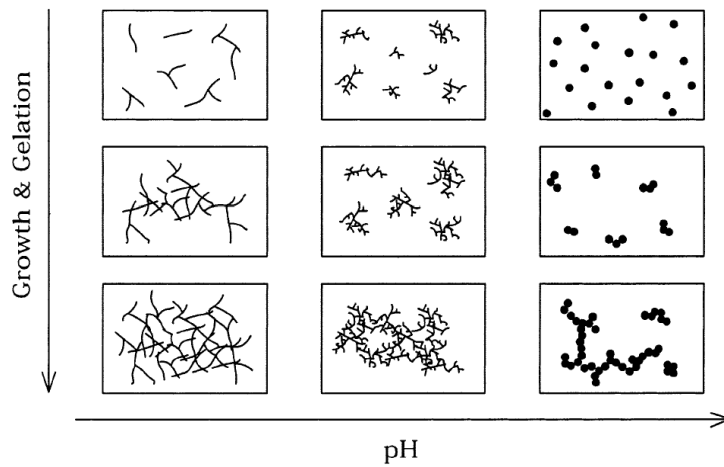
Fig. 4: Influence of the pH and precursor concentration in sol-gel chemistry[11]

A high pH in combination with a decreased precursor concentration can result in a colloidal dispersion of discrete spheres with a monodisperse particle size distribution. Decreasing the pH normally leads to smaller particles but at the same time to a higher degree of crosslinking.

In combination with an increased precursor concentration, the gelation process is supported. In order to direct the synthesis towards the formation of small discrete particles, the nucleation rate at the beginning should be high. Thus, a multitude of seeds that can further grow is formed. A very common model for the formation of nanoparticles in sol-gel chemistry is described with the LaMer-diagram[13] shown Fig. 5.
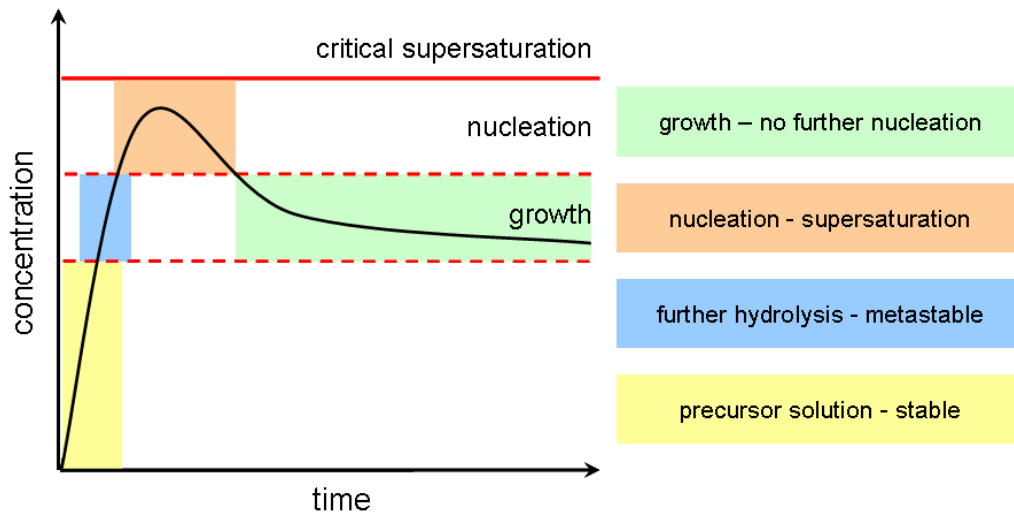
Fig. 5: LaMer-diagram for the formation of colloidal dispersions

The concentration of the precursor that forms the dispersed phase increases due to some chemical or physical process. At a certain degree of supersaturation, nucleation occurs, either heterogeneously on impurity centers or homogeneously through spontaneous nucleation. The growth of these nuclei causes the concentration to fall below the nucleation concentration, below which no more particles are created. The particles continue to grow, however, until the concentration falls to the saturation concentration.

The requirements for monodispersity are evident from the LaMer diagram:

The rate of nucleation must be high enough so that the concentration does not continue to increase.

On the one hand, the growth rate of these nuclei must be fast enough to reduce the concentration below the nucleation concentration quickly. In this way only a limited number of particles are created.

On the other hand, the growth rate must be slow enough that the growth period is long compared to the nucleation period. This usually narrows the size distribution

As already mentioned, a material consisting of nanoparticles can reach very high surface areas, a fact that plays an important role, e.g., in catalysis. Another possibility to increase the specific surface area is the introduction of an inherent porosity. In this context, the synthesis of nanostructured porous materials has become an important topic in the field of materials science.

Porous Materials

The unique property of porous materials is the very high surface-to-mass ratio along with a high absorption capacity. They can be used in many applications, including catalysis, as adsorbents in separation processes or, depending on the framework charge, as ion exchangers. Depending on the type of material, the specific surface area can reach several thousand square meters per gram. The morphology of the particles, the pore size and their surface chemistry can be varied depending on the application. Porous materials are classified by their pore sizes in three categories, namely micro- ($d < 2$ nm), meso- (2 nm $< d <$ 50 nm) and macroporous ($d > 50$ nm).[14]

Common macroporous materials are porous glasses, silica gels, and activated carbon. In these materials the pore system is often based on the space between particles, which often varies in a certain range and is difficult to control.

Important microporous materials are zeolites, which offer well-defined pore diameters in the range between about 0.25 and 1.2 nm.

Zeolites

Zeolites are minerals that have a microporous structure. More than 150 zeolite structure types have been synthesized and 48 naturally occurring zeolites are known.[15] Natural zeolites form where volcanic rocks and ash layers react with alkaline groundwater; they are often contaminated to varying degrees by other minerals, metals, quartz or other zeolites. For this reason, naturally occurring zeolites are excluded from many important commercial applications where uniformity and purity are essential. There are several types of synthetic zeolites that form by a process of slow crystallization of a silica-alumina gel in the presence of alkali, and sometimes organic structure-directing agents (SDA) or templates. The most important processes to carry out zeolite synthesis belong to sol-gel chemistry. The product properties depend on the composition of the reaction mixture, pH, temperature, reaction time or templates present. Synthetic zeolites hold some key advantages over their natural analogs. They can be manufactured in a uniform, phase-pure state. It is also possible to synthesize desirable structures that do not appear in nature, e.g., Zeolite A. Zeolites are widely used as ion-exchange beds in domestic and commercial water purification or softening. In chemistry, zeolites are used as "molecular sieves". The term refers to a particular property of these materials, i.e., the ability to selectively sort molecules based primarily on a size exclusion process. This is due to the very regular pore structure of molecular dimensions, which is conventionally defined by the ring size of the aperture. For example, the term "12-ring" refers to a closed loop that is built from 12 tetrahedrally coordinated silicon (or aluminum) atoms and 12 oxygen atoms (Fig. 6).
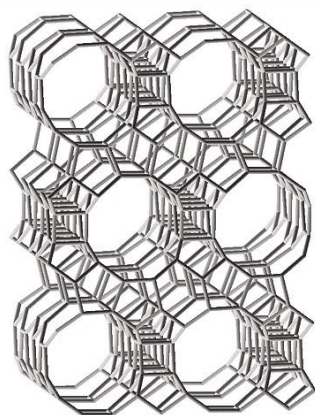
Fig. 6: Structure of zeolite BEA (projection viewed along [100])[16]

The largest outlet for synthetic zeolite is the global laundry detergent market. But synthetic zeolites are also well established as catalysts in the petrochemical industry, for instance in fluid catalytic cracking and hydro-cracking. Zeolites confine molecules in small spaces, which causes changes in their structure and reactivity. The hydrogen forms of zeolites (prepared by ion-exchange) are powerful solid-state acids, and can facilitate acid-catalyzed reactions, such as isomerization, alkylation, and cracking.

Zeolites or zeo-type materials can also be used as solar thermal collectors and for adsorption refrigeration. In these applications, their hygroscopic property coupled with an inherent exothermic reaction when transitioning from a dehydrated to a hydrated form (heat of adsorption) make zeolites effective in the storage of heat energy. Due to their high porosity in combination with a good thermal conductivity, zeolites are also being explored as dielectric thin films in low-*k* technology.[17]

Regardless of the variety, the maximum pore size of zeolites and thus their use is limited. Therefore researchers tried to find materials with a well-ordered pore system that exhibit pore diameters of more than 2 nm.

Mesoporous Silica

In 1992 scientists of the Mobil Research and Development Corporation discovered the first ordered mesoporous silica. The synthesis was realized through a condensation of a silica precursor in the presence of self-organizing surfactant molecules acting as template. Depending on the reaction conditions, different modifications of mesoporous silica can be synthesized. A very common material is the so-called MCM-41 (Mobil Composition of Matter No. 41) with a hexagonal pore structure. Other known types are, e.g., the cubic MCM-48, lamellar MCM-50 or disordered worm-like mesoporous silica (Fig. 7).
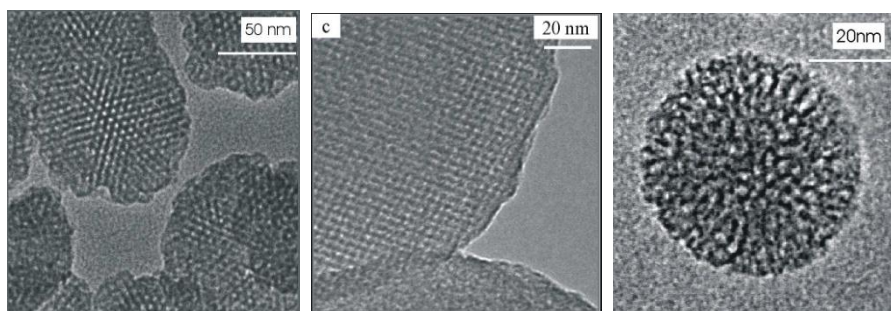
Fig. 7: TEM-micrographs of MCM-41, MCM-48 and worm-like mesoporous silica

In general four reagents are needed for the synthesis of mesoporous silica: water, a surfactant, a silica precursor, and an agent catalyzing the hydrolysis. The product features can be controlled by the parameters temperature, pH or batch composition.

A widely accepted model for the formation mechanism of mesoporous silica is shown in Fig. 8. This cooperative templating model shows the formation of nanocomposite biphasic arrays. [18]
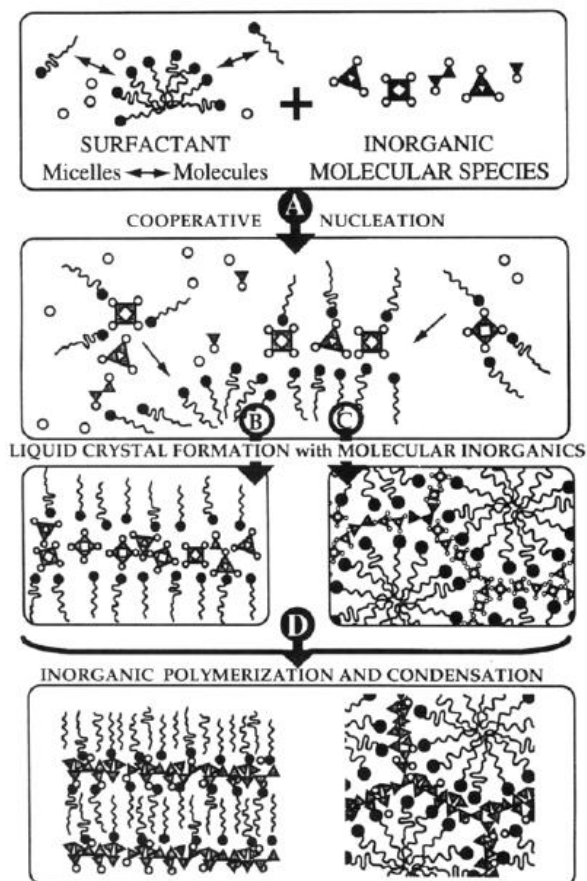
Fig. 8: Cooperative silicate-template-mechanism[18]

The formation of mesoporous silica via the S^+I^- synthesis route can be described as follows:

Single-chain surfactant cations (S^+) react with silicate polyanions, e.g., dimers, double three and four rings (I^-). Micelles serve as a source for surfactant molecules or are rearranged according to the anion charge density and shape requirements.

Nucleation and rapid precipitation of organized arrays takes place with configurations determined by the cooperative interactions of ion-pair charges, geometries and Van-der-Waals-forces.

Condensation of the silicate phase with increasing time and temperature takes place. The silicate framework charge decreases during this process; this may lead to liquid crystal-like phase transitions as the surfactant phase tries to reorganize the changing interface charge density.

The framework becomes more and more stable through further condensation of silicate anions into the inorganic network,.

Control over the pore size and pore topology can be achieved by using, e.g., templates with varying chain lengths or block-copolymers. Thus, pore diameters between about 1.5 to 20 nm can be realized. This universally applicable model can also be transferred to the synthesis of other mesoporous metal oxides like titania.[19]

Evaporation Induced Self Assembly (EISA)

The above model is also valid for the formation of mesoporous films by the so called EISA approach.[20] In general, thin films are thin material layers ranging from fractions of a nanometer to several micrometers in thickness. The EISA process (Evaporation Induced Self Assembly) typically starts with a homogeneous solution of silica precursor and surfactant prepared in ethanol/water with an initial surfactant concentration much below the critical micelle concentration. A preferential evaporation of ethanol concentrates the surfactant and silica species in the remaining liquid phase. The progressively increasing surfactant concentration drives self-assembly of silica-surfactant micelles and their further organization into liquid-crystalline mesophases (Fig. 9).
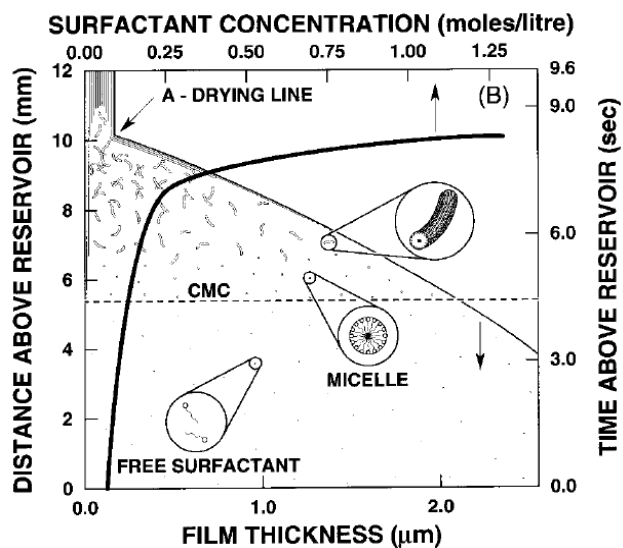
Fig. 9: Mesophase formation during EISA thin film synthesis[20]

Pre-existing, incipient silica-surfactant mesostructures serve to nucleate and orient mesophase development. This results in the rapid formation of thin film mesophases that are highly oriented with respect to the substrate surface. It is possible to obtain different final mesostructures through variation of the initial alcohol/water/surfactant ratios.

Functionalization

For some applications it can be interesting to modify the surface of the porous structure - either bulk material or film. By introducing, for example, organic groups, the hydrophobicity of the materials can be reduced (Fig. 10). In general, two approaches for the modification of the mesoporous silica are followed. The introduction of the organic moieties can be accomplished either after synthesis (grafting)[21] or during the synthesis via co-condensation.[22-24]
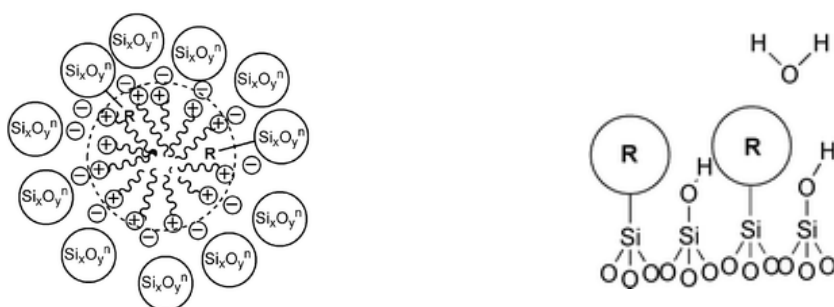
Fig. 10: Functionalization of mesoporous silica with organic groups and the resulting hydrophobicity[25]

Grafting:[26]

The post-synthetic grafting is achieved with organotrialkoxysilanes or organotrichlorosilanes. The template-free mesoporous silica is dispersed mostly in non-polar anhydrous solvents to avoid a reaction of the organosilanes with anything but the silica material. The reaction takes place between the silanol groups on the surface and the organoalkoxysilanes / organotrichlorosilanes. Studies showed that silanols located on the exterior surface and near the pore openings are kinetically more accessible than silanols on the interior pore wall. Thus, most organic functional groups are located there. It is possible to preferentially functionalize the surface of mesoporous silica particles. This is especially the case when the grafting is performed before the surfactant is removed from the mesopores. After the grafting has been performed, the surfactant can be removed. This control over the location of functional groups may enable the interaction of the porous particle with the environment through the surface functionalization while not influencing the pore surface properties.

The second important method for the synthesis of organically functionalized mesoporous silica materials is the co-condensation. In this direct, "one-pot" synthesis method, tetraalkoxysilanes together with an organo-substituted trialkoxysilane are added to the aqueous surfactant solution. Hydrophobic groups are supposed to interact with the hydrocarbon tails of the surfactant templates, and thereby evenly distribute across the pore surface. Furthermore, the organic moieties are linked through multiple siloxane bridges (Fig. 11).
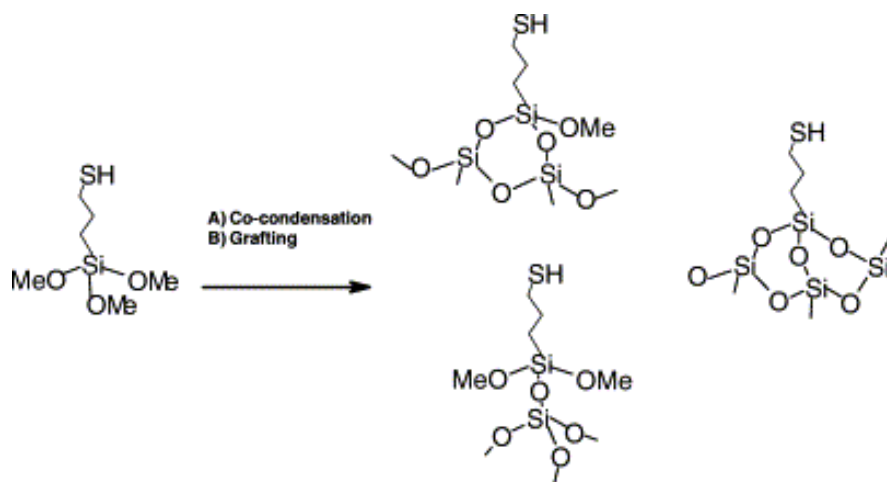
Fig. 11: Method for the functionalization of silica with an alkoxysilane [27]

Additionally, this synthetic approach allows one to control the morphology of the particles. The influence of the organoalkoxysilanes on particle morphology depends upon the abilities to stabilize or destabilize the micelles.[28]

A great number of commercial available siloxanes can be introduced. The register of possible functional groups can be extended, e.g., through a post-synthetic modification after the co-condensation (Fig. 12).
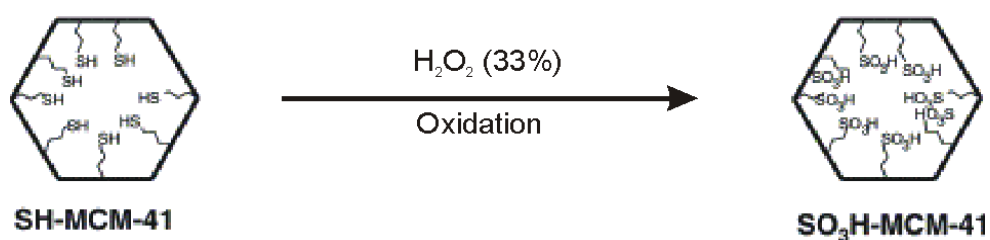
Fig. 12: Post-synthetic modification of mesoporous organo-silica material[27]

Extraction

In order to obtain a porous material after the templated synthesis, the surfactant has to be removed. This can be realized either by calcination or extraction. In the case of most functionalized materials, the template cannot be removed by calcination, unless the organic groups are sufficiently thermally stable.[29] In the literature one can find different possibilities for the removal of the template by extraction – mainly complex procedures, such as extraction with supercritical carbon dioxide[30] or treatment with microwave radiation.[31] The most common method is some kind of ion-exchange in alcoholic media, e.g., with a mixture of ethanol and hydrochloric acid. The material is refluxed for several hours and thus protons replace the template cations. It is also possible to use more gentle extraction procedures, e.g., a solution of ammonium nitrate in ethanol.[32]

Mesoporous Titania

After the discovery of the templated synthesis of mesoporous silica, much effort was made to adapt the synthesis principle to the formation of mesoporous titania – however, this turned out to be more challenging than for the silica system. While the EISA-approach is effective,[20] the synthesis of ordered mesoporous bulk material or nanoparticles similar to MCM-41 is often less successful. Synthesis problems are mainly associated with the weak interaction between the cationic template molecules and the inorganic phase and the faster hydrolysis of titania precursors.[33, 34] Further difficulties emerge from the preferred hexagonal coordination of Ti atoms often

resulting in lamellar structures,[33] and the tendency to reorganize into stable crystalline phases at relatively low temperatures, e.g., as anatase or rutile.

However, there is a substantial interest in nanostructured titania films, especially for photocatalytic and photovoltaic applications. The excellent electrical and mechanical properties of porous nanostructured titania make it an ideal material for dye-sensitized solar cells (DSSC).[35] While DSSCs are cheaper to manufacture than silicon-based cells, they are still less efficient. For the production of efficient DSSCs, a semiconducting layer with a high surface area is required to ensure a high loading with a sensitizing dye. Already a relatively thin film of titania nanoparticles doped with an appropriate dye can produce a significant electric current.

Optical Properties of Thin Films

In thin film deposition, a thin layer of material is prepared on a substrate or previously deposited layer. "Thin" is a relative term, since a film may look operationally thin or thick, according to the procedure applied, e.g., optically thin or thick compared to the wavelength of the light used. The most famous example for optically thin films may be iridescent soap bubbles.

Besides the thickness, the refractive index is the second important variable in thin films for optical applications. The refractive index n of a medium is a measure for how much the speed of light is reduced when traveling through it. For example, glass has a refractive index of around 1.5, which means that light travels at $1 / 1.5 = 0.67$ times the speed in vacuum.

Dispersion and absorption

The effect that n varies with frequency (except in vacuum, where all frequencies travel at the same speed) is known as dispersion, and it is what causes a prism to divide white light into its constituent spectral colors. In real materials, the polarization does not respond instantaneously to an applied field. This causes dielectric loss, which can be expressed by a permittivity that is both complex and frequency dependent. Real materials are not perfect insulators either, i.e., they have non-zero direct current conductivity. Taking both aspects into consideration, a complex index of refraction can be defined:

$$\tilde{n} = n - i\kappa$$

Here, n is the refractive index indicating the phase velocity as above, while κ is called the extinction coefficient, which indicates the amount of absorption loss when the electromagnetic wave propagates through the material. Both n and κ are dependent on the wavelength. In regions of the spectrum where the material does not absorb, the real part of the refractive index tends to increase with frequency. Near absorption peaks, the curve of the refractive index is a complex form given by the Kramers-Kronig relations, and can decrease with frequency.

Since the refractive index of a material varies with the frequency (and thus wavelength) of light, it is common to specify the corresponding vacuum wavelength at which the refractive index is measured. Typically, this is done at a well-defined spectral emission line; for example, the sodium D line at 589 nm (n_D).

Two common properties of transparent materials are directly related to the difference in the refractive index of the materials. Light is bended when it crosses the interface and it reflects partially from surfaces.

In thin film interference, this phenomenon causes the characteristic colors, like in the case of soap bubbles or tarnished metals.[36] Fig. 13 shows the dependence of the interference colors on the thickness of a SiO_2 film on silicon at a view angle of 45°.
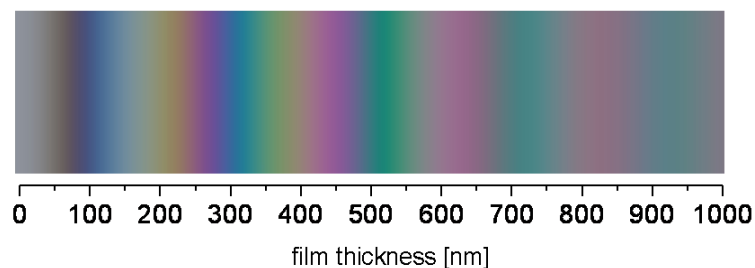
Fig. 13: Calculated interference colors of a silica film on silicon[37]

Stacking thin layers with different refractive indices can enforce this effect. These multilayer reflectors or so-called Bragg stacks can also be observed in nature, when chitin layers are alternated with different refractive index layers in order to control the apparent color in a wide variety of animals.[38] In the laboratory, these special thin films can be prepared, for example, by alternation of low refractive index SiO_2 with highly refractive TiO_2 films. Regarding porous thin films, the possible change of the interference color upon adsorption of volatile species comes to mind. This sensing effect of porous films has already been reported in several publications,[39-43] also in combination with the Bragg-stacks.[44]

2. MOTIVATION

In summary it can be ascertained that porous materials are of great interest in many fields of science and technology. There are numerous publications on the synthesis of all kinds of porous materials. Meanwhile, there is also a rapidly growing literature on synthesis procedures for porous nanoparticles. We then ask if it could be interesting to synthesize porous materials at the nanometer scale and how could they be of use in nanotechnology.

As already mentioned, nanoparticles exhibit a multitude of interesting properties. In combination with the characteristics of the zeolite materials, the resulting nanoparticles are ideal candidates for numerous applications.[45]

However, zeolites are often restricted by the small pore diameter. Especially in the liquid phase, diffusion plays a major role. The reactants need to diffuse rapidly towards and away from catalytically active sites. Due to the larger pore diameter and the resulting improved diffusion properties of the mesoporous materials, they are good candidates for catalysis and sensing applications. In order to obtain selectivity towards different adsorbates or reactants, the materials can be modified with various functional groups.[39]

In some domains the particle size and the existence of single particles is essential. Colloidal suspensions of discrete mesoporous silica nanoparticles, which can be synthesized in nearly every dimension and additionally functionalized with a multitude of organic groups, are ideal candidates for demanding application areas like drug delivery.[26] The loading and release of the drug can be controlled by selectively functionalizing the inner surface of the particle, whereas the outer surface can be

modified with bioactive groups. It is also imaginable to use porous particles as host system for other materials, such as quantum dots or dyes for biolabeling.[46, 47] Encapsulating of sensitive dyes in the porous particles[48, 49] could be useful for the incorporation in polymer matrices.

Especially in the case of producing thin films, homogeneous dispersions of nanoparticles for the preparation, e.g., by spin-coating are of great interest. Electronic semiconductor devices and optical coatings are the main applications for thin film construction. For example, the use as low-k materials is intensively investigated. And porous titania films are a basic necessity in today's dye sensitized solar cells (DSSCs).

The preparation of thin films with porous nanoparticles has a range of advantages over the common EISA approach for mesoporous films and the growth of zeolite films on substrates:

It is believed that the porous thin films made of (porous) nanoparticles exhibit improved diffusion properties and a highly accessible pore system.[50]

Additionally one can work with stable suspension of already extracted nanoparticles assuring facile handling and good reproducibility.

The coating of sensitive substrates is facilitated due to the mild conditions.

Control over the thickness can be attained by varying concentration or by introducing multiple step coating.

Intricate template removal procedures between the coating steps are needless

The adhesion to different surfaces can be influenced by the addition of binders to the coating suspensions.

It could be also feasible to combine suspensions containing different kinds of nanoparticles in order to assemble hybrid thin films.

Finally, the material is easier to characterize when bulk samples are available.

Porous nanoparticles and thin films are viewed to have a tremendous potential in various applications. Thus, the goal of this work was the synthesis of porous nanoparticles as monodisperse colloidal suspensions. These suspension were used for the preparation of porous thin films. Thorough characterization of the nanostructures is necessary to establish understanding and control of their synthesis and applications.

3. CHARACTERIZATION METHODS

The characterization of porous nanoparticles can be done by using a variety of different techniques, mainly drawn from materials science. Common techniques are electron microscopy (TEM, SEM), atomic force microscopy (AFM), dynamic light scattering (DLS), powder x-ray diffractometry (XRD), and vibrational spectroscopy (IR, Raman). The determination of the inherent or interparticle porosity of the materials can be achieved with different methods. As the sorption plays a key role in many application areas, the characterization of the materials by their sorption properties is one of the most important methods.

Sorption

Gas adsorption is a prominent method to obtain a comprehensive characterization of porous materials with respect to their specific surface area or pore size distribution. In a common gas sorption measurement, the sample is attached to a vacuum manifold and distinct relative pressures ($p\, p_0^{-1}$) of the probe gas are adjusted. During the measurement the adsorbed and desorbed volumes of gas (in $cm^3\, g^{-1}$) on the sample surface (apparent outer surface and accessible pore surface) is calculated for varying relative pressures at a constant temperature. From the obtained isotherms one can draw conclusions about the size and morphology of pores. The isotherms are categorized according to IUPAC[51] as shown in Fig. 14.
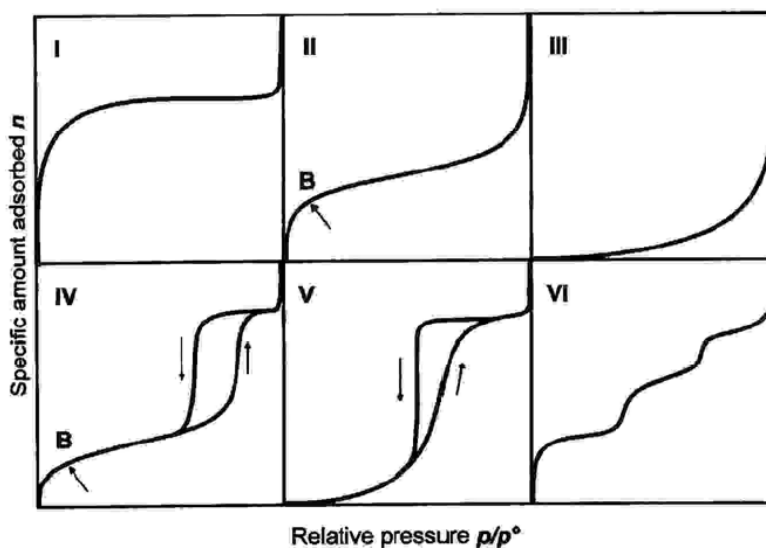
Fig. 14: The six isotherms defined by the IUPAC[51]

Type I is typical for microporous materials and shows a plateau after the filling of the small pores at low relative pressures.

Type II isotherms describe the formation of multilayers after the monolayer is completed at point B. This shape in combination with the complete reversibility upon desorption is typical for non-porous materials.

Type III and V are rarely observed and reflect a low interaction energy between adsorbate and adsorbent.

Type IV isotherms are typical for mesoporous samples. The original IUPAC classification defined the hysteresis as characteristic feature of mesoporous materials.

Type VI shows an example isotherm for samples with a stepwise multilayer absorption of a non-porous material.

In Fig. 15, a typical isotherm for nanometer-sized mesoporous materials (Type IV) with fields for the individual sorption steps is shown.
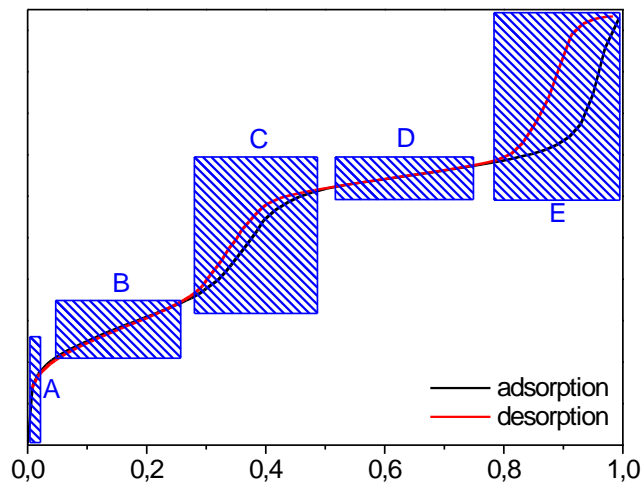
Fig. 15: Typical isotherm for a bulk sample of mesoporous nanoparticles

The steps A to E can be attributed to the following processes:

A: At low relative pressures $p\,p_0^{-1}$ a monolayer of adsorbate molecules is forming on the high inner surface of the material

B: Multilayers are established

C: Filling of the mesopores occurs (capillary condensation)

D: The remaining outer surface is covered (plateau)

E: In samples with very small particles, the adsorbate condenses in the interparticle pores

The most common sorption method is nitrogen sorption, because of a suitable heat of adsorption (5-25 kJ mol^{-1}) and a good access of nitrogen molecules (0.354 nm) into small pores. An evacuated sample cooled with liquid nitrogen is loaded with gaseous nitrogen. Due to the low temperature, the nitrogen is adsorbed on the sample surface, resulting in equilibrium between adsorbed film and gas phase at constant temperature. The isotherm shows the adsorbed amount of gas as a function of the pressure. Different models can describe the adsorption.

BET-surface area

In contrast to the Langmuir model, the method developed by Brunauer, Emmet and Teller[52] allows the formation of multilayers. For low partial pressures ($p\,p_0^{-1} < 0.3$) the BET-equation can be transformed into a linear correlation:

$$\frac{\dfrac{p}{p_0}}{n\left(1-\dfrac{p}{p_0}\right)} = \frac{C-1}{n_m \cdot C} \cdot \frac{p}{p_0} + \frac{1}{n_m \cdot C}$$

n : adsorbed gas quantity

n_m : monolayer adsorbed gas quantity

C   : BET-constant

p : equilibrium pressure

p_0 : saturation pressure

With this equation an adsorption isotherm can be plotted as a straight line with $n^{-1}[(p_0 \, p^{-1}) - 1]^{-1}$ on the y-axis and $p \, p_0^{-1}$ on the x-axis according to experimental results. This plot is called a BET plot. The linear relationship of this equation is typically maintained only in the range of $0.05 < p \, p_0^{-1} < 0.3$.

With the required cross-section of an adsorbate molecule, the monolayer adsorbed gas quantity n_m (mol g^{-1}) and the BET-constant C, the specific surface area can be calculated.

Pore diameter

If gas molecules are introduced into a pore system, their physical properties change. Capillary condensation into the curved surface can occur long before the saturation vapor pressure is reached. The Kelvin equation provides a thermodynamic correlation between the relative pressure $p \, p_0^{-1}$ and the reduced radius (Kelvin radius) r_k during pore condensation:

$$r_k = \frac{-2\gamma V_L}{RT \cdot \ln\left(\dfrac{p}{p_0}\right)}$$

γ : adsorbate surface tension

V_L : molar volume
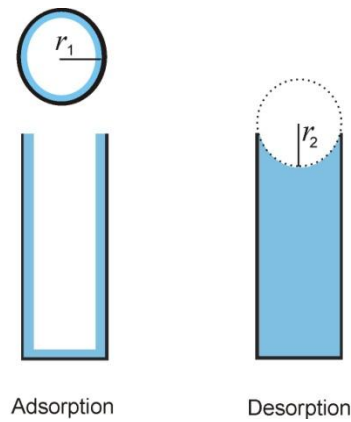
Fig. 16: Adsorption and desorption in a pore

The reduced radius r_k describes the curvature of the adsorbate film onto the surface and is composed of pore radius r_1 and the meniscus radius r_2 in the filled pore (Fig. 16)

$$\frac{2}{r_k} = \frac{1}{r_1} + \frac{1}{r_2}$$

In adsorption r_2 is infinite and thus r_k is $2r_1$. In desorption $r_1 = r_2 = r_k$. For this reason, the desorption branch is commonly used for the determination of the pore diameter.

BJH-Method

The pore radius can be determined with a method developed by Barrett, Joyner, and Halenda (*BJH*). The radius of the cylindrical pore r_p is composed of the Kelvin radius r_k and the thickness t of the adsorbed monolayer:

$$r_p = r_K + t$$

The thickness t has to be calculated using the density of the adsorbed liquid. The De Boer equation associates the thickness of the adsorbed layer with the relative pressure in nitrogen sorption isotherms:

$$t = \frac{K}{\log\left(\dfrac{p}{p_0}\right) + 0.034}$$

K : Constant

The *BJH*-method as classical macroscopic concept based on the Kelvin equation is linked to the pore condensation phenomena. It is applicable for mesopore size analysis, but fails to correctly describe both the pore filling of micropores and of narrow mesopores. In contrast, the Density Functional Theory (DFT) or methods of molecular simulation such as Monte Carlo simulation or Molecular Dynamics provide a microscopic model of adsorption based on a more realistic description of the thermodynamic properties of the intra-pore fluid.[53]

Other sorption measurements

Nitrogen sorption is a standard method for bulk materials. Besides the common adsorptives such as nitrogen, argon or krypton, it can be also interesting to investigate the sorption properties of other gases like alkanes.[54] Especially when investigating sorption properties of thin films, other methods have to be used. One possibility is the sorption measurement using a quartz crystal microbalance.

Quartz Crystal Microbalance

In a quartz crystal microbalance (QCM), the changes in the resonance frequency of a piezoelectric quartz crystal are correlated to mass changes deposited onto the crystal surface. Due to the high precision in frequency measurements, it is possible to measure very small mass changes. For the correlation between mass and frequency changes, the Sauerbrey equation is used:

$$\Delta f = \frac{-2\Delta m f_0^2}{A\sqrt{\rho_q \mu_q}} = -\frac{2 f_0^2}{A \rho_q \upsilon_q} \Delta m$$

It gives the change Δf in the oscillation frequency of a piezoelectric quartz crystal as a function of the mass Δm added to the crystal. Here, f_0 is the resonant frequency of the crystal, A is the active area between the electrodes, ρ_q is the density of quartz, μ_q is the shear modulus of quartz, and υ_q is the shear wave velocity in quartz.

The Sauerbrey equation was developed for oscillation in air and only applies to rigid masses attached to the crystal, for example, thin films.

For a certain quartz-crystal, the material constants can be combined to a factor C_f and thus the equation is reduced to:

$$\Delta f = -C_f \cdot \Delta m$$

For a 10 MHz quartz crystal (Fig. 17), a loading of 1 ng per cm^2 correlates with a decrease in the resonant frequency by 0.226 Hz.

Fig. 17: 10 MHz quartz crystal microbalance

Depositing porous films onto the QCM makes it possible to investigate the mass changes associated with sorption and thus recording isotherms. If the density of a homogeneous coating is known one could also calculate the film thickness.

An alternative investigation of the thickness and additionally of the optical properties of thin films can be done by a versatile and powerful optical technique called ellipsometry.

Ellipsometry

Ellipsometry measures the change of polarization of light upon the interaction with matter. The name stems from the fact that the reflected light will, in general, be elliptically polarized. Ellipsometry can yield information about layers that are thinner than the wavelength of the probing light itself, even down to a single atomic layer. It can probe the complex refractive index or dielectric function tensor, which gives access to fundamental physical parameters and is related to a variety of sample properties, including morphology, crystal quality, chemical composition, or electrical conductivity. Ellipsometry is commonly used to characterize film thickness for single layers or complex multilayer stacks ranging from a few tenths of a nanometer to several micrometers.

Experimental setup

Electromagnetic radiation is emitted by a light source and linearly polarized before it falls onto the sample. After reflection, the now elliptically polarized light passes a second polarizer - the analyzer - and falls into the detector (Fig. 18).
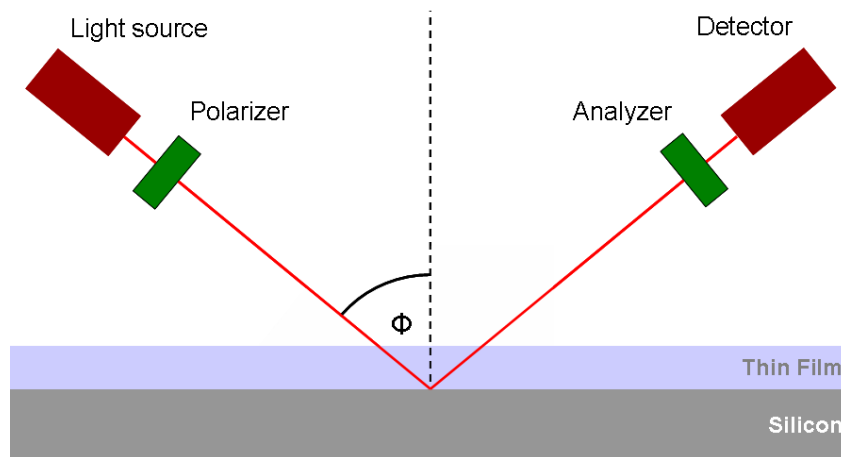
Fig. 18: Schematic setup of an ellipsometry experiment

Ellipsometry measures two of the four Stokes parameters, which are conventionally denoted by Ψ and Δ. The incident and the reflected beam span the plane of incidence. Light that is polarized parallel or perpendicular to the plane of incidence, is called p or s polarized, respectively. The amplitudes of the s and p components, after reflection and normalization to their initial values, are denoted by r_s and r_p, respectively (Fig. 19).
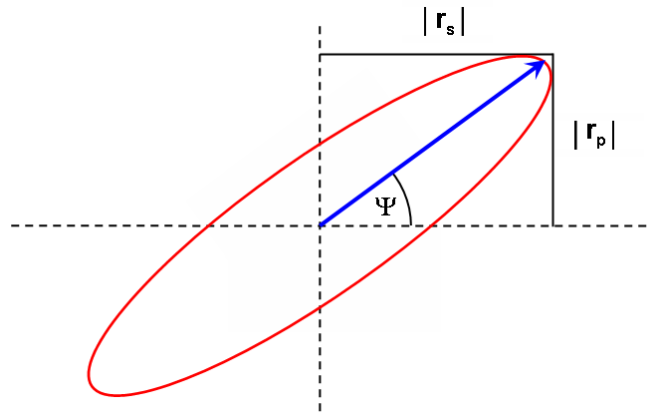
Fig. 19: The quantities r_s and r_p in elliptically polarized light

The ratio of r_s and r_p is described by the fundamental equation of ellipsometry:

$$\frac{r_p}{r_s} = \tan(\Psi)e^{i\Delta}$$

Thus, $\tan \Psi$ is the amplitude ratio upon reflection, and Δ is the phase shift (difference). Since ellipsometry is measuring the ratio of two values, it is very accurate and reproducible, relatively insensitive to scattering and fluctuations, and requires no standard sample or reference beam.

Data analysis

Ellipsometry is an indirect method, i.e., in general the measured Ψ and Δ cannot be converted directly into the optical constants of the sample. Normally, a layer model must be established, which considers the optical constants (refractive index or dielectric function tensor) and thickness parameters of all individual layers of the sample including the correct layer sequence. Using an iterative procedure (least-squares

minimization), the unknown optical constants and thickness parameters are varied, and Ψ and Δ values are calculated using the Fresnel equations. The calculated Ψ and Δ values that match the experimental data best, provide the optical constants and thickness parameters of the sample. In spectroscopic ellipsometry (SE) a broad-band light sources is employed, which covers a certain spectral range in the infrared, visible or ultraviolet region. Thus the complex refractive index or the dielectric function tensor in the corresponding spectral region can be obtained, which gives access to a number of fundamental physical properties.

Ellipsometric porosimetry

Regarding porous, transparent thin films, ellipsometric porosimetry[55, 56] can be used to describe the change of the optical properties that are associated with the sorption of volatile species. The method uses the Lorentz-Lorenz formula, which is based on the Clausius-Mossotti equation:

$$\frac{\varepsilon_{rel} - 1}{\varepsilon_{rel} + 2} \cdot \frac{M}{\rho} = \frac{N_A \cdot \alpha}{3\varepsilon_0}$$

It describes the relation between the macroscopic measurable relative dielectric constant ε_{rel} and the electric polarizability α. N_A is the number of molecules in one mole (Avogadro constant) and ε_0 is the vacuum permittivity.

$M \cdot \rho^{-1}$ is the molar volume V_m, which can also be described as $N_A \cdot N^{-1}$ (N is the number density of molecules):

$$V_m = \frac{M}{\rho} = \frac{N_A}{N}$$

Thus, the Clausius-Mossotti equation can be written as:

$$\frac{\varepsilon_{rel} - 1}{\varepsilon_{rel} + 2} = \frac{N \cdot \alpha}{3\varepsilon_0} \quad \text{with} \quad \frac{N \cdot \alpha}{3\varepsilon_0} = P_v$$

P_v is the volume polarizability. In a certain range of frequencies (visible and UV), the Maxwell theory relates the refractive index of a substance with its relative dielectric constant. With $\varepsilon_{rel} = n^2$, the Clausius-Mossotti equation can be converted into the Lorentz-Lorenz function:

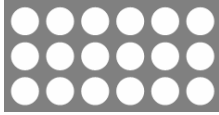$$\frac{n^2 - 1}{n^2 + 2} = P_v$$

The Lorentz-Lorenz equation is used for the characterization of porous substrates with ellipsometric porosimetry. The individual components act additive in the following approximation:

A dense substrate with the refractive index n_d:

$$P_{vd} = \frac{n_d^2 - 1}{n_d^2 + 2}$$

An empty porous substrate with the refractive index n_e ($n_{air} = 1$, V = volume of open pores):

$$P_{ve} = \frac{n_e^2 - 1}{n_e^2 + 2} = V \cdot \frac{n_{air}^2 - 1}{n_{air}^2 + 2} + (1 - V) \cdot \frac{n_d^2 - 1}{n_d^2 + 2} = (1 - V) \cdot \frac{n_d^2 - 1}{n_d^2 + 2}$$

A filled porous substrate with the refractive index n_f (n_{ads} = refr. index of the adsorbate):
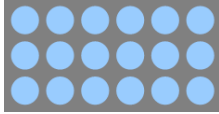
$$P_{vf} = \frac{n_f^2 - 1}{n_f^2 + 2} = V \cdot \frac{n_{ads}^2 - 1}{n_{ads}^2 + 2} + (1 - V) \cdot \frac{n_d^2 - 1}{n_d^2 + 2}$$

When the refractive index of the filled and empty porous substrate is known, one can determine the porosity of the material without knowing the refractive index of the dense material:

$$P_{vf} - P_{ve} = \frac{n_f^2 - 1}{n_f^2 + 2} - \frac{n_e^2 - 1}{n_e^2 + 2} = V \cdot \frac{n_{ads}^2 - 1}{n_{ads}^2 + 2}$$

Therefore, the volume V of the open pores can be determined as follows:

$$V = \left(\frac{n_f^2 - 1}{n_f^2 + 2} - \frac{n_e^2 - 1}{n_e^2 + 2} \right) \bigg/ \frac{n_{ads}^2 - 1}{n_{ads}^2 + 2}$$

Light Scattering

Mie Scattering

For the description of the scattering ability of particles similar to or larger than the wavelength of light, the Mie theory or discrete dipole approximation can be used. The Mie solution, also called Mie theory, is a complete analytical solution of Maxwell's equations for the scattering of electromagnetic radiation by spherical particles. In contrast to Rayleigh scattering, the Mie solution to the scattering problem is valid for all possible ratios of diameter to wavelength, although the technique results in numerical summation of infinite sums. Although scattering of light by a homogeneous sphere may seem to be a simple process, the Mie solution is very complex and not easy to understand. In its original formulation it assumed a homogeneous, isotropic, and optically linear material irradiated by an infinitely extending plane wave. Currently, the term "Mie solution" is also used in broader contexts, for example, when discussing solutions of Maxwell's equations for scattering by stratified spheres or by infinite cylinders. If particles are much smaller than the wavelength of the incoming light, their scattering ability can be described according to Rayleigh.

Rayleigh Scattering

Rayleigh scattering describes the scattering of light or other electromagnetic radiation by particles much smaller than the wavelength of the light. It occurs when light travels in transparent solids and liquids, but is most prominently seen in gases. The amount of

Rayleigh scattering that occurs to a beam of light is dependent upon the size of the particles and the wavelength of the light.

The intensity of light scattered by a single small particle from a beam of unpolarized light of wavelength λ and intensity I_0 is given by:

$$I = I_0 \frac{1+\cos^2\theta}{2R^2}\left(\frac{2\pi}{\lambda}\right)^4\left(\frac{n^2-1}{n^2+2}\right)^2\left(\frac{d}{2}\right)^6$$

Here, R is the distance to the scattering particle, θ is the scattering angle, n is the refractive index of the particle, and d is the diameter of the particle. In simple terms, the scattering coefficient - the intensity of scattered light - on small particles can be described with the following dependencies:

$$I \sim \frac{1}{\lambda^4} \text{ and } I \sim r^6$$

The wavelength dependence of the scattering means that blue light is scattered much more than red light. In the atmosphere; this results in blue light being scattered to a greater extent than red light, and so one sees blue light coming from all regions of the sky. As a rule of thumb, due to the strong dependence on the particle size, a colloidal suspension is expected to become transparent when the particle size is decreased below 1/10 of the wavelength of the incoming light. Thus a potential transparent colloidal dispersion ideally contains nanoparticles smaller than about 40 nm in diameter.

Dynamic Light Scattering in Colloidal Suspensions

Dynamic light scattering (DLS), also known as quasi elastic laser light scattering, is a powerful technique in physics, which can be used to determine the size distribution profile of small particles dispersed in a liquid phase. When light hits small particles it is scattered in all directions. If the light source is a laser, and thus is monochromatic and coherent, then one observes a time-dependent fluctuation in the scattering intensity. These fluctuations are due to the fact that the small particles in suspensions are undergoing Brownian motion and thus the distance between the scattering centers in the solution is constantly changing. The scattered light interferes either constructively or destructively. These intensity fluctuations contain information about the time scale of the particle movement. The smaller the particles are, the faster they diffuse and thus the faster the intensity changes. These fluctuations are correlated across microsecond time scales by an autocorrelation function, i.e., a function that describes how a given measurement relates to itself in a time-dependent manner. The second order autocorrelation curve (g^{II}) can be directly derived from the intensity trace:

$$g^{II}(q;\tau) = \frac{\langle I(t)I(t+\tau)\rangle}{\langle I(t)^2\rangle}$$

q : wave vector

τ : delay time

I : intensity

At short time delays, the correlation is high because the particles do not have a chance to move to a great extent from the initial state that they were in. As the time delays become longer, the correlation starts to exponentially decay to zero, meaning that after a long time period, there is no correlation between the scattered intensity of the initial and final states. This exponential decay is related to the diffusion coefficient. To fit the autocorrelation function, numerical methods are used. If the sample is monodisperse then the decay is simply a single exponential. The Siegert equation relates the second order autocorrelation function (g^{II}) with the first order autocorrelation function (g^{I}) as follows:

$$g^{II}(q;\tau) = 1 + \beta \left[g^{I}(q;\tau) \right]^2$$

β : correcting factor

Once the autocorrelation data have been generated, different mathematical approaches can be employed to determine the *z*-averaged translational diffusion coefficient (*D*). In case of a monodisperse sample, a single exponential function is obtained for the decay of the autocorrelation function, where Γ is the decay rate:

$$g^{I}(q;\tau) = \exp(-\Gamma\tau) \quad \text{with} \quad \Gamma = Dq^2 \quad \text{and} \quad q = \frac{4\pi n_0}{\lambda} \sin\left(\frac{\theta}{2}\right)$$

λ is the incident laser wavelength, n_0 is the refractive index of the sample and θ is angle at which the detector is located with respect to the sample cell. The Stokes-Einstein

equation describes the dependency of the diffusion coefficient D on the radius r of a spherical particle in a liquid phase with the viscosity η at a certain temperature T:

$$D = \frac{kT}{6\pi\eta r}$$

Electron Microscopy

As the maximum resolution of light microscopes is determined by the wavelength of the photons that are being used to probe the sample, imaging of nanoparticles becomes difficult. Like all matter, electrons have both wave and particle properties (as proposed by de Broglie), and their wave-like properties mean that a beam of electrons can be focused by electrical and magnetic fields onto the sample. As the wavelength is dependent on their energy, it can be tuned by adjustment of accelerating fields resulting in a much smaller wavelength than that of light. The wavelength of electrons accelerated by 200 kV is only 2.51 pm, but the theoretical resolution is limited to about 0.1 nm because of the aberration in today's electron lenses.

In transmission electron microscopy (TEM), the beam of electrons is transmitted through a specimen. Then an image is formed, magnified and directed to appear either on a fluorescent screen, a layer of photographic film, or a CCD camera.

With a Scanning Electron Microscope (SEM) it is possible to produce high-resolution images of a sample surface with a characteristic three-dimensional appearance. In a typical SEM, the emitted electrons are focused into a very fine focal spot sized 1 nm to

5 nm. The beam passes through pairs of scanning coils in the objective lens, which deflect the beam horizontally and vertically so that it scans in a raster fashion over a rectangular area of the sample surface. When the primary electron beam interacts with the sample, the electrons lose energy by repeated scattering and absorption. The energy exchange between the electron beam and sample results in the emission of electrons and electromagnetic radiation which can be detected to produce an image.

Thermogravimetric Analysis

Thermogravimetric Analysis (TGA) determines the changes in weight in relation to changes in temperature by raising the temperature gradually and plotting weight against temperature. The weight loss curve may require transformation before results can be interpreted. The first derivative of the weight loss curve is used to find the points at which weight-loss is most rapid. TGA is commonly employed to determine characteristics of materials, such as degradation temperatures, absorbed moisture, the proportions of inorganic and organic components in materials, and solvent residues. Additionally, Differential Scanning Calorimetry (DSC) provides data on thermodynamic effects by measuring the time-dependent heat flow between the sample and a reference.

Powder X-ray Diffraction

Powder XRD uses x-ray diffraction on powder or microcrystalline samples for the structural characterization of materials. It is based on the elastic scattering of electromagnetic waves on lattice planes, or more precisely at the electronic shells of regularly arranged atoms. Ideally, every possible crystalline orientation is represented equally in a powdered sample. The Bragg equation is a simple method to determine the distance d of lattice planes. To derive the Bragg equation one considers the lattice planes of a crystal as semitransparent mirrors partly reflecting an incoming beam (Fig. 20).
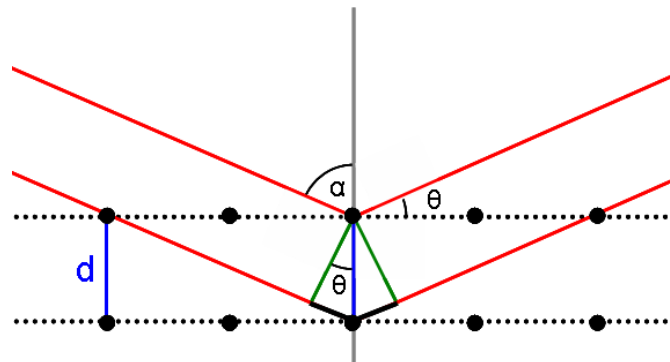
Fig. 20: Sketch to construct the Bragg equation

For a monochromatic beam the reflected rays interfere constructively or destructively depending on the angle of incidence θ and the lattice diameter d. Two reflected monochromatic beams interfere if the path difference is an integer multiple of the wavelength λ. This results in the Bragg equation for constructive interference:

$$n\lambda = 2d \sin \theta \ \text{ with } n = 1, 2, 3, \ldots$$

When the scattered radiation is collected on a flat plate detector the averaging due to random orientations of the particles leads to smooth diffraction rings around the beam axis rather than the discrete Laue spots as observed for single crystal diffraction. The angle between the beam axis and the ring is called the scattering angle and in x-ray crystallography denoted as 2θ.

Solid-State NMR

A nuclear spin can interact with a magnetic or electric field. Spatial proximity or a chemical bond between two atoms can give rise to interactions. In general, these interactions are orientation dependent. In media with no or little mobility (e.g., crystal powders, large membrane vesicles, molecular aggregates), anisotropic interactions have a substantial influence on the behavior of a system of nuclear spins. In contrast, in a classical solution-state NMR experiment, Brownian motion leads to an averaging of anisotropic interactions. In such cases, these interactions can be neglected on the time-scale of the NMR experiment. Examples of anisotropic nuclear interactions commonly found in solid-state NMR are the chemical shift anisotropy and the internuclear dipolar

coupling. Anisotropic interactions modify the nuclear spin energy levels (and hence the resonance frequency) of all sites in a molecule, and often contribute to a line-broadening effect in NMR spectra. High-resolution conditions in solids can be established using magic angle spinning (MAS), which facilitates averaging of interactions in real space.

In ^{29}Si MAS NMR of functionalized silica samples, typically five peaks can be observed. Q^n-peaks are related to Si-atoms linked to two, three or four other Si-atoms by an oxygen bridge, and to hydroxyl groups. T^n-peaks derive from Si-atoms carrying one organic moiety:

$[Q^4]$: **Si**(OSi)$_4$

$[Q^3]$: **Si**(OSi)$_3$(OH) $\qquad\qquad$ $[T^3]$: R**Si**(OSi)$_3$

$[Q^2]$: **Si**(OSi)$_2$(OH)$_2$ $\qquad\qquad$ $[T^2]$: R**Si**(OSi)$_2$(OH)

The chemical shift of the T-peaks depends on the nature of the Si-C bond. Thus different functional groups can be distinguished. Depending on the area of these peaks, one can make statements about the linkage in the solid state.

IR and Raman Spectroscopy

FT-IR and FT-Raman spectroscopy are methods to investigate the vibrational modes of a sample by absorption or scattering of radiation, respectively. Both techniques are appropriate for the identification of specific functional groups, especially in organic moieties. In inorganic solids, hydroxyl groups or characteristic Raman active centers

can be detected. If a chemical group changes its dipole moment during vibration, it can be detectable in infrared spectroscopy. The moieties of a molecule (for instance, a methyl group) can be identified by their specific absorption bands in the infrared spectrum. In Raman spectroscopy, energy transfer from incident coherent laser light induces vibrations of molecules, and the scattered light from the sample is analyzed. The energy for exciting the molecular vibrations is taken from the photon energy (Stokes frequencies) or the energy of the vibrations is transmitted to the photons (Anti-Stokes frequencies), respectively. During vibration, the polarizability of the molecule has to change in order to observe Raman-active modes.

4. RESULTS AND DISCUSSION

4.1 High Silica Zeolite Beta: From Stable Colloidal Suspensions to Thin Films

Introduction

Zeolites and zeolite-like materials with their uniform pore sizes, unique structural topology and composition, well defined acidity and good thermal stability are viable commercial catalysts, selective ion exchangers and absorbers. Although many different crystalline molecular sieves are already known, there is a continuing need for zeolites with new properties and a continuing search for new zeolite applications. More recent efforts have focused on exploring the possibilities of synthesizing zeolites in the nanosized range by application of highly supersaturated precursor solutions.[45, 57] By using organic additives during the synthesis procedure, colloidal solutions were formed and used for the preparation of different nanosized molecular sieves.[58-64] Several microporous materials including MFI, LTA, FAU, BEA and LTL in the form of stable colloidal suspensions with narrow particle size distribution (100 nm) are described in the literature. Intriguingly, among the nanosized zeolites the pure silica forms were only reported for the MFI, MEL and BEA structure types.[65-67]

BEA is a large-pore microporous material characterized by three sets of mutually perpendicular channels with 12-membered ring apertures, which can be prepared from classical aluminosilicate gels with a wide range of Si/Al ratios.[68] The main features of this structure make the material suitable for numerous applications such as heterogeneous catalysis, sensors, membranes, *etc*.[67, 69-71] The number of acid sites and the hydrophobicity of the microporous materials can be tuned by controlling the Si/Al ratios in the final crystallites.

One important application of purely siliceous microporous zeolites exhibiting a high degree of hydrophobicity and a high micropore volume is in the field of nanoscale layers with low dielectric constant (low-k) for microelectronic applications, as well as for the preparation of hard coatings with unique properties.[72, 73] Pure silica zeolite BEA was synthesized by Corma and co-workers, using tetraethylammonium hydroxide (TEAOH) as a template and fluoride ions at near neutral pH.[74] In addition, BEA crystals were recently prepared *via* a solid–solid transformation method,[69, 75] and the synthesis of colloidal siliceous BEA from highly templated precursor solutions was reported.[76] One of the focused applications of the pure silica BEA type molecular sieve is in the preparation of highly porous and hydrophobic layers, which can exhibit variable optical and electronic properties depending on the method of preparation. Several strategies have been applied for the formation of microporous films, and recently a very effective method was established for deposition of ultrathin pure siliceous MFI type films on two-dimensional supports *via* spin-coating of stable colloidal suspensions.[65] Due to their unique properties, particles at the nanometer scale are of great interest in a number of advanced applications. Homogeneously dispersed in a solvent, these colloidal suspensions show similarities to real solutions, which make them suitable for the preparation of thin homogeneous and transparent films by spin-coating. As a result of their crystallinity, the coatings have high mechanical stability and resistance to many solvents. Additionally, decreasing the crystal size of particles below 100 nm produces substantial changes in the physicochemical properties of the zeolite,

particularly in the external surface of the crystals, as well as the ability of such nanocrystals to pack closely in the film during spin-coating.[77]

The aim of this paper is to describe a complete route for the synthesis of zeolite Beta from templated precursor solutions with emphasis on the crystallization kinetics, stabilization of the nanosized crystallites in coating suspensions, and the assembly in thin films exhibiting variable physicochemical properties.

Experimental

Synthesis of nanosized zeolite Beta

The composition of the precursor solution used for synthesis of nanosized zeolite Beta crystals was 25 SiO_2 : 1 Al_2O_3 : 15 TEAOH : 375 H_2O. The initial compounds were mixed in one pot until a clear solution was obtained: Cab-o-sil M5 (Riedel-DeHäen) as silica source, aluminum sec-butoxide (Aldrich) as aluminum source, tetraethylammonium hydroxide (TEAOH, 35 wt %, Aldrich) as organic template, and deionized water were used. The hydrothermal (HT) treatment of the precursor mixtures was performed in an oven at 140 °C under static conditions using steel autoclaves with 18 ml Teflon liners. Every 24 hours one autoclave was taken out and the product was purified by a series of centrifugation steps (1 h at 47,800 g RCF) and subsequently redispersed in water under sonication (1 h in ice) till the pH of the solution reached 10. A part of the final crystalline zeolite Beta was dealuminated according to the procedure described in Ref.[78] The Si/Al ratio of the as-synthesized and dealuminated zeolite Beta was 32 and 100, respectively.

Stabilization of Beta nanoparticles in coating suspensions

The as-prepared and dealuminated zeolite Beta nanoparticles were treated with an aqueous solution of diluted ammonium chloride and then washed with ethanol two times in order to prepare stable zeolite suspensions and to prevent fast agglomeration. After washing and redispersion, the colloidal suspensions were centrifuged at 12000 g (RCF) for 5 min, and the sediment was separated by decanting in order to eliminate the larger agglomerates formed during the purification process. The final solid concentration of zeolite Beta nanoparticles was adjusted to 4 wt % in ethanolic suspension, and further applied for the preparation of thin films.

Three types of binders were used to improve the mechanical stability of the porous films: (1) aqueous colloidal silica suspension Nalco 2326 (SiO_2, ~15 wt %, particle size ~ 5 nm) was diluted with ethanol to reach a concentration of 2 wt %; (2) pre-hydrolyzed tetraethylorthosilicate (TEOS) in a mixture of ethanol, water and HCl in the ratio of 1 TEOS : 0.06 HCl : 27 H_2O : 60 EtOH, and (3) pre-hydrolyzed TEOS with cetyltrimethylammonium bromide (CTAB) in the following ratio 1 TEOS : 0.1 CTAB : 0.06 HCl : 27 H_2O : 60 EtOH. The size of the amorphous silica particles formed in TEOS-based binders (solutions 2 and 3) was kept constant, e.g., about 2 nm in diameter determined from dynamic light scattering (DLS) measurements. The silica nanoparticles in the binding solutions 2 and 3 were stable for about 10 days, while afterwards a slight increase in size was measured.

Deposition of thin Beta films on silicon wafers

The ethanolic zeolite suspension was either used directly for the film deposition or it was mixed with the same volume of one of the three binders prior to spin-coating. No additional functionalization of the zeolite nanoparticles was carried out. In order to ensure the preparation of smooth and homogeneous films, the coating suspensions were filtrated through syringe filters (450 nm) prior to spinning.

The nanoporous films were deposited on polished silicon wafers by spin-coating (Laurell WS-400B-6NPP-Lite-AS) with a rate of 3000 rpm (acceleration 5000 rpm s^{-1}) for 30 s. All substrates were pre-cleaned with ethanol and acetone for 10 s under spinning at 3000 rpm. In order to prepare thick Beta films, the spin-coating procedure was repeated up to 6 times. After each coating step, the films were calcined at 450 °C for about 30 min.

From the numerous films prepared with different thickness the following will be discussed in detail: pure Beta film free of binder (Beta-pure), Beta crystals stabilized with prehydrolyzed TEOS (Beta-TEOS) and Beta crystals stabilized with amorphous silica (Beta-SiO$_2$) (see Table 1). No significant differences were observed between the samples prepared with the two types of TEOS binders (solutions 2 and 3), and therefore only binder 2 will be discussed.

Table 1: Zeolite Beta films deposited on silicon wafers.

film	binder	deposition steps	thickness	refractive index	porosity (% void)
Beta-pure	no	3	475 nm	1.10	77
Beta-TEOS	TEOS	3 and 6	440 and 680 nm	1.13	70
Beta-SiO$_2$	SiO$_2$	1 and 6	185 and 950 nm	1.15	70

Characterization

The degree of crystallinity of the zeolite materials was determined based on X-ray diffraction patterns collected from purified powders with a STOE Stadi P diffractometer using monochromatic Cu-K$_\alpha$-radiation in transmission geometry. Additionally, the degree of crystallinity, size and morphology of the zeolite particles was proven by collecting transmission electron micrographs (TEM) on a JEOL JEM 2011 instrument with LaB$_6$ cathode at 200 kV. Samples were prepared on Plano holey carbon coated copper grids by evaporating one droplet of the purified zeolite suspensions diluted with water in the ratio of 1 : 100. Besides, the evaluation of the particle size in the suspensions was determined by DLS. The DLS data were collected with an ALV-NIBS/HPPS High Performance Particle Sizer in PMMA cuvettes at 25°C under continuous scans and analyzed according to the cumulant and distribution function analysis (DFA). The polydispersity index (PDI) calculated for all samples was used as an indication for a multi-modal particle size distribution. The powder Beta samples

were subjected to thermogravimetric analysis (TGA) after purification and freeze drying. The powders were heated in corundum crucibles from 30 to 900 °C (10 °C/min) in a flow of synthetic air (25 ml/min) using a Netzsch STA 449 C Jupiter thermobalance. The amount of organic template and water in the framework type Beta zeolite was determined in the samples prepared from 1 to 10 days of HT treatment. The surface features of the nanoparticles deposited in thin films were investigated with scanning electron microscopy (Philips 40 XL) and ellipsometry. The ellipsometric measurements were performed on a Woollam M2000D at different angles (65°, 70°, and 75°) in the entire spectral range of 190-1000 nm. The data were fitted in the range between 250-1000 nm using the Cauchy model for layered materials or using the EMA layer (Bruggeman effective medium approximation) of SiO_2 and introducing additional voids.[79]

Results and Discussion

Suspensions of Beta nanoparticles: kinetic study and stabilization

In order to follow the crystallization kinetics of nanosized zeolite Beta, the initial solution with an Si/Al ratio of 25 ratio was heated under hydrothermal conditions and the crystallization process was interrupted at various times; the solid phases extracted at the different stages of crystallization were subjected to comprehensive characterization. The change in the solid products was followed with X-ray diffraction, DLS, TEM and TGA. The XRD patterns depicted in Fig. 21 show that the amorphous precursor

solutions transformed into crystalline zeolite Beta particles after 7 days, and the
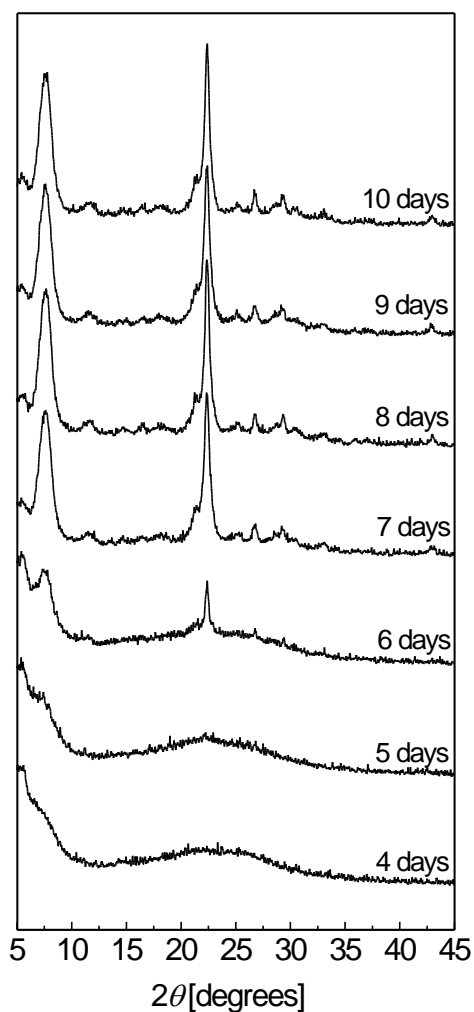prolonged hydrothermal treatment did not change the degree of crystallinity.

Fig. 21: XRD pattern of the Beta samples synthesized under hydrothermal conditions

The first Bragg reflection at 6.2° 2θ occurs with a very low intensity in the sample after
heating for five days. The low intensity of the Bragg reflection is possibly due to the
very small crystalline particles (< 5 nm) that are present in the solid samples extracted

from the reacting solutions, or to the low amount of crystalline particles in comparison to the amorphous matter. It is important to note that the width of the Bragg reflections did not change significantly, which proves that no substantial change in the final particle sizes occurred during the prolonged heating of the reaction systems (see samples crystallized for 6 and 10 days).

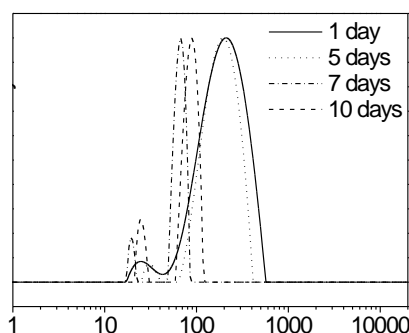The generation of amorphous and crystalline particles in the precursor solutions was measured by DLS (see Fig. 22).

Fig. 22: DLS data of purified suspensions, hydrothermally treated from 1 and 10 days.

It is important to note that the clear precursor solutions turned into dense transparent gels after 24 h aging and kept the same texture even after hydrothermal treatment up to six days. A fluid translucent suspension is obtained after seven days of heating. The DLS curves of the samples treated for 1 and 2 days show a very broad particle size distribution even after substantial dilution with water (PDI > 0.5; the curves are not shown here). This confirms the presence of unstable amorphous nanoparticles in the

suspensions, and the continuous dynamics of agglomeration and disintegration in the reacting aluminosilicate species in the crystallizing system. After three days of heating, two generations of particles, one with an average hydrodynamic diameter of about 20-60 nm and another of about 80 - 200 nm are detected in the precursor mixture. It is also observed that with increasing crystallization time, only the width of the particle size distribution curves is diminishing, while the mean size does not change significantly. This observation can be explained with the higher stability of the growing particles in the samples crystallized from 3 to 6 days. However, the colloidal zeolites tend to agglomerate and at the same time disintegrate under purification of the reacting mixture and redispersion in water or ethanol under sonication. In the suspensions with a pH lower than 8 and solid concentration above 6 wt %, a significant increase in the particle diameter is observed. Based on the DLS data, one can conclude that the aggregates are formed in the crystalline and intermediate suspensions, and they are measured instead of the individual particle grains. This statement is proven by the TEM study, where it can be seen that the nanoparticles tend to agglomerate and do not exist as separated crystals (Fig. 23).
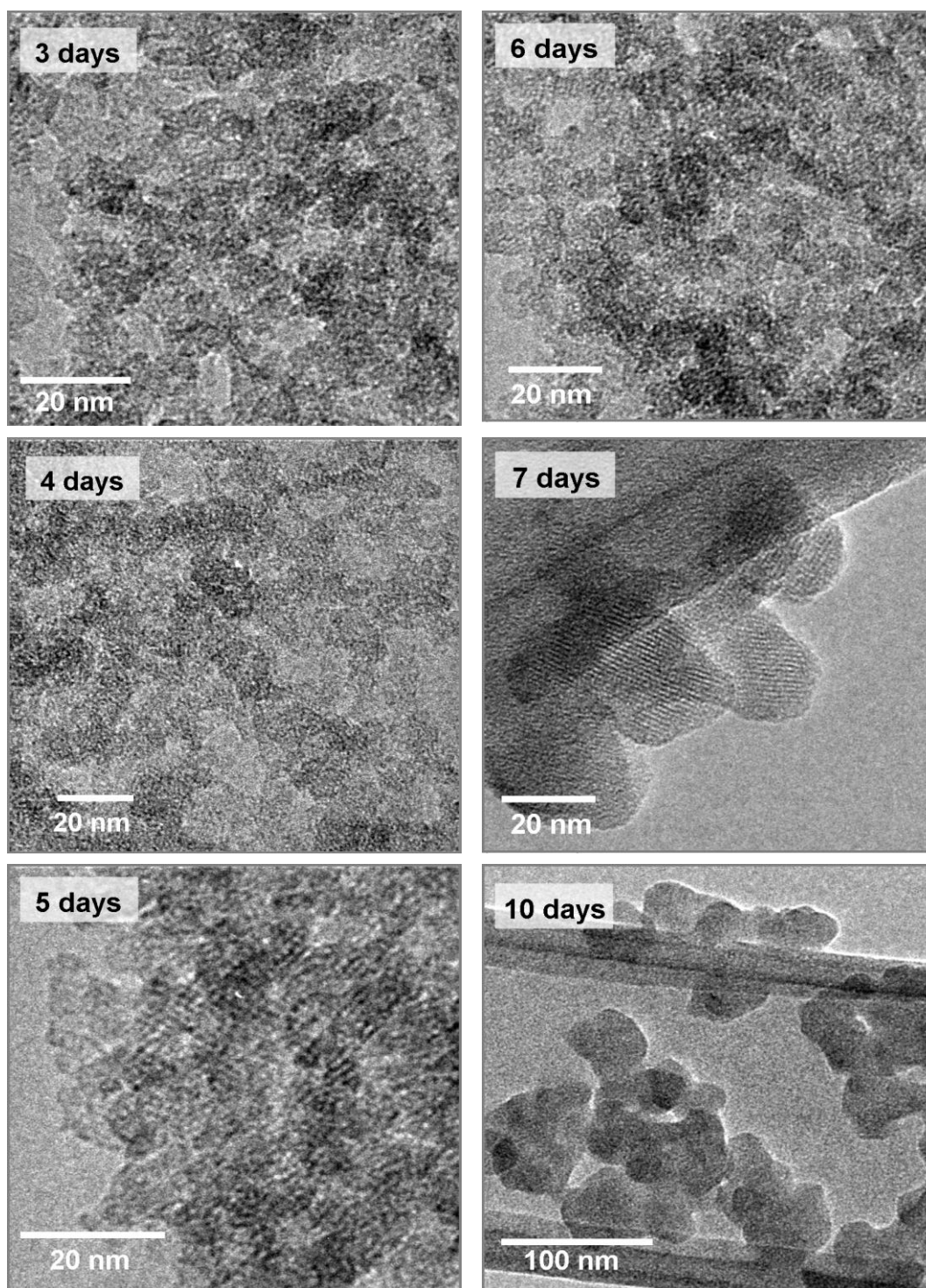
Fig. 23: TEM images of nanoparticles extracted from suspensions after a hydrothermal treatment between 3 and 10 days.

The aggregation process is also accelerated with prolonging the time of hydrothermal treatment (8 days), and the mean size of the zeolite domains in the particles is increased from 20 up to 40 nm according to the TEM data. At a very early time of HT treatment, any separation of the crystalline from the amorphous particles was not possible. Crystalline fringes representing the Beta crystalline phase in the mostly spherical amorphous particles can be seen in the samples treated for 5 and 6 days. The crystalline particles have the same size and shape as the amorphous ones. In many cases a good alignment between several crystalline fringes in the particles is observed. This process is accelerated at the end of the hydrothermal treatment. According to the TEM micrographs, particles with size in the range 8 - 15 nm were present during the entire process of crystallization. However, after 5 days some of the particles contain crystalline fringes and some of them appear amorphous. After 6 days the fraction of crystalline particles is increased while the number of amorphous particles is decreased, which is confirmed by both the XRD and DLS data (see Fig. 21 and Fig. 22). The sample heated for 7 days contains fully crystalline nanoparticles, which appear more disintegrated in comparison to the ones heated for 10 days. A slight increase in the size of the individual particles and additional agglomeration is observed in the sample heated for 10 days due to the longer crystallization time.

The transformation of the amorphous aluminosilicate species into crystalline zeolite Beta was also followed by TG analysis. The amount of organic template and water is changing depending on the degree of the samples' crystallinity. As can be seen from

Fig. 24, the weight loss due to desorption of water and combustion of TEAOH is decreased with increasing degree of crystallinity of the samples.
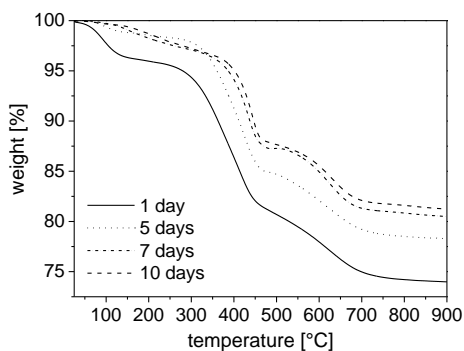

Fig. 24: TG data of the solid samples recovered from precursor solutions subjected to hydrothermal treatment from 1 to 10 days.

The samples heated for 7 and 10 days have almost the same amount of template and an almost negligible amount of water, which is expected for highly siliceous molecular sieves. In contrast, in the partially crystalline sample (5 days HT treatment), the amount of water and TEAOH is higher than in the crystalline Beta. This can be explained with an extra amount of template adsorbed on the surface and in the mesoporous aluminosilicate amorphous grains. Thus the weight loss of the washed and dried products is decreased in the crystalline samples, and the combustion of the template is shifted to higher temperatures. This is due to the different location of the template in the amorphous or crystalline matrix, i.e. the TEA^+ cations are encapsulated in the zeolite channels instead of the surface or in the mesopores. In conclusion, the amount of water

and template encapsulated in the material is decreased, while the temperature of decomposition is increased with higher crystallinity.

Beta nanocrystals stabilized in coating suspensions and films

The interfacial chemistry between the binders and the zeolite particles was studied. Dynamic light scattering measurements were performed in pure zeolite suspensions as well as in binder-containing coating suspensions in order to study the stability prior to film deposition. The Beta crystals used for preparation of thin films were obtained according to the procedure described above (140 ºC, 10 days) after dealumination. The XRD pattern from the solid sample synthesized in a larger amount (500 ml, solid concentration of 6 wt %) shows the presence of pure BEA-type zeolite (Fig. 25).
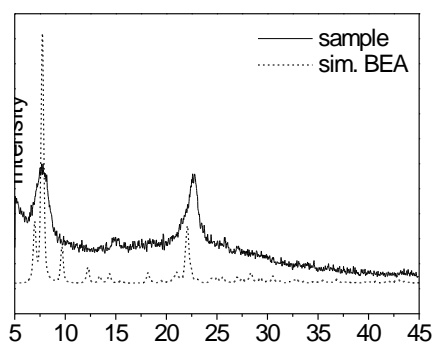

Fig. 25: XRD patterns of pure zeolite Beta nanocrystals from the coating suspension used for preparation of thin films in comparison with the simulated pattern

The dynamic light scattering results of the same Beta-pure suspension reveals particles with a hydrodynamic diameter in the range of 20 - 80 nm (Fig. 26), which are attributed to the zeolite Beta in the form of single crystals and probably as agglomerates in a comparable amount. This conclusion is based on the different presentations of the scattering intensity (mass-weighted and unweighted). As can be seen, the ratio between the two classes of particles with size of 20 nm and 80 nm is increased substantially when the scattering is expressed as mass-weighted. It is known that this method better represents the real picture (TEM investigations) in a suspension containing particles with the same density, crystallinity and chemical composition. The particle size distribution of this coating mixture does not change with time (at least one week); this confirms its colloidal stability at ambient temperature (see Fig. 26, left image).
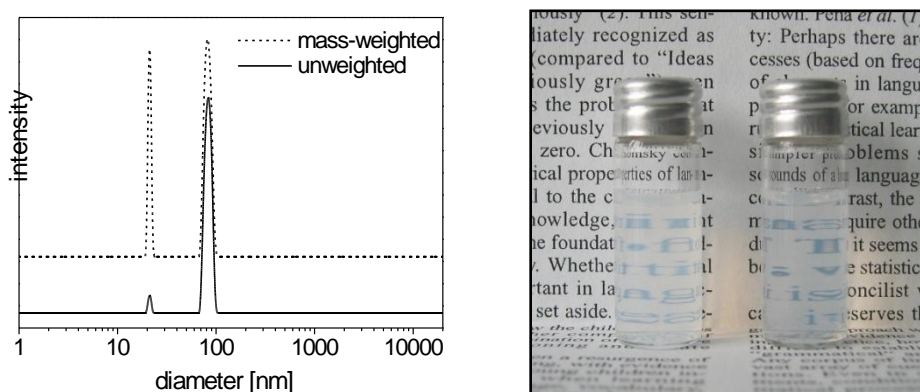

Fig. 26: DLS curves of zeolite coating suspension: Beta-pure expressed as mass-weighted and unweighted particle size distribution (a) and picture representing the coating Beta-pure (right) and Beta-TEOS suspension (left)

This coating suspension was mixed with the three binders and remained stable with no sedimentation during one week at ambient conditions. All suspensions with the three binders appear transparent with minor scattering, similar to the ones shown in Fig. 26. The thin Beta films prepared with the above suspensions appear homogeneous and transparent to the eye. The thickness of the films is increased by several deposition steps of the coating suspensions, resulting also in a change of the defined interference color of the films (Fig. 27).
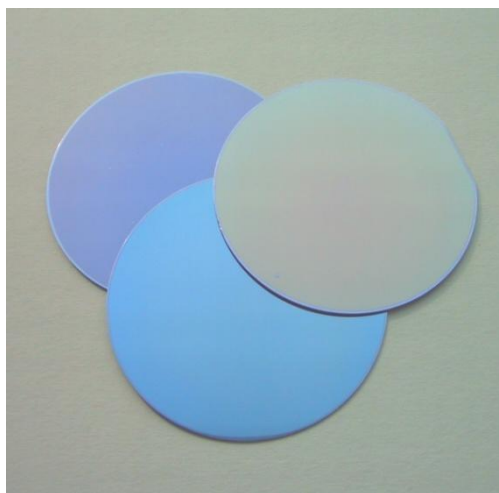

Fig. 27: Picture of silicon wafers with Beta-TEOS films prepared by one step (l.), two step (m.) and three step deposition (r.)

SEM investigations of the Beta-pure, Beta-TEOS and Beta-SiO2 were performed in order to investigate the thickness of the layers, their surface morphology and homogeneity. In general, the films prepared with binder exhibit a smooth surface and do not show big differences (Fig. 28).
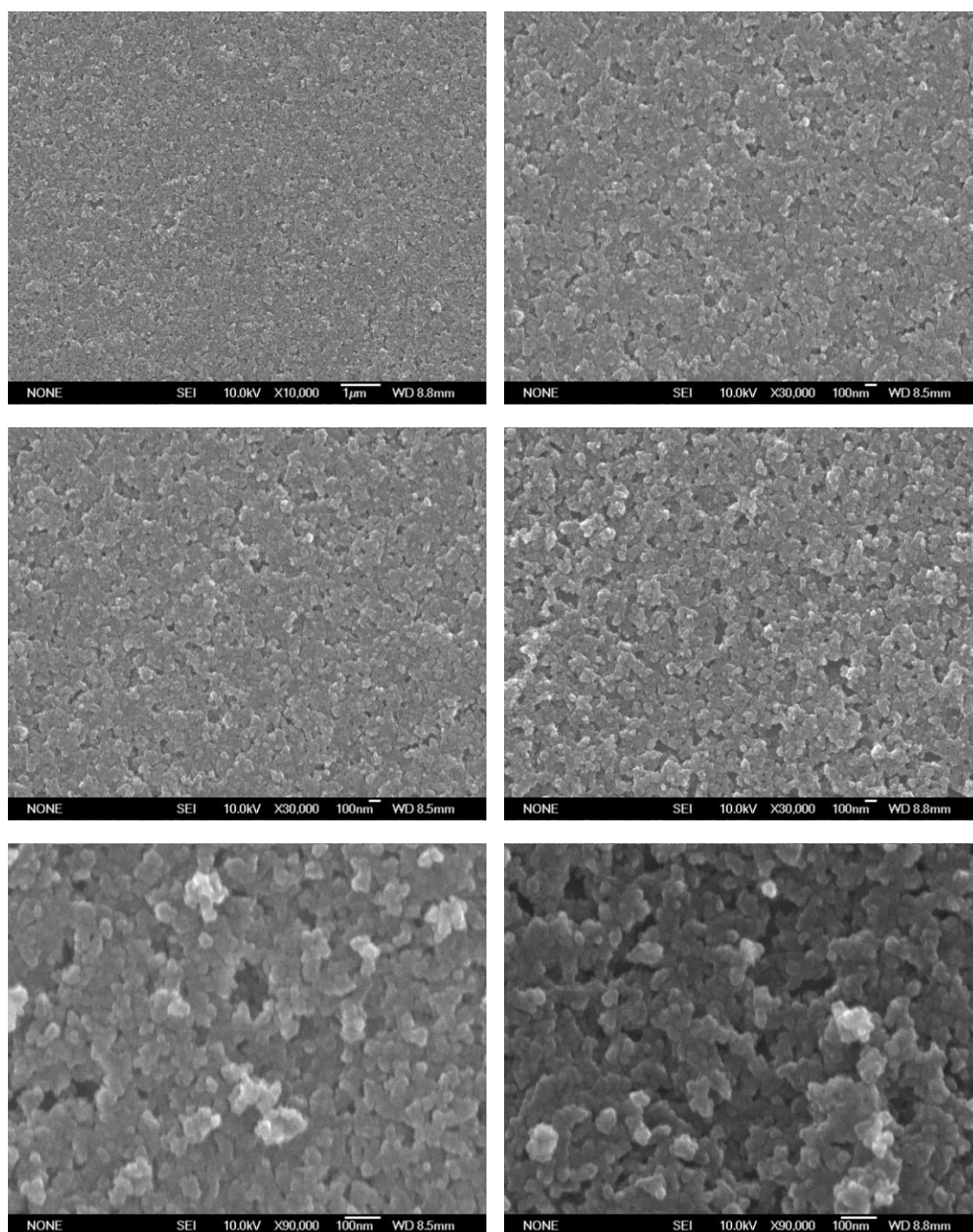
Fig. 28: SEM pictures of films deposited on silicon wafers based on zeolite Beta without binder (Beta-pure, left) and with binder (Beta-SiO2, right) at different magnifications

Homogeneous and continuous films at a centimeter scale were obtained by one- to six-step spin-coatings, and the homogeneity of the deposited layer is preserved by the close packing of the Beta nanocrystals surrounded by the binding agents. The individual crystallites in the films prepared from Beta-SiO2 and Beta-TEOS suspensions are more closely packed in comparison with pure Beta suspensions. Besides, the Beta-pure film has lower adhesion in comparison to the films with added binder.. An increased surface roughness of the multilayered films is observed in all films. This can be explained by the higher surface roughness of the intermediate porous layers in comparison to the bare Si-wafer, which is propagated and amplified with each coating step. The smoothness of the films could be improved by the application of smaller particles. However, small particles tend to agglomerate faster than the bigger ones and therefore the stabilization of zeolite grains with a size less then 10 nm could be a great challenge (provided they could be made). Another possibility is to use an additional top layer of binder to fill all gaps between the crystalline particles deposited in Beta-pure films. However, this will influence the surface chemistry and more specifically the hydrophilicity of the entire film, which will increase, whereas the porosity will decrease.

Introducing porosity into a thin film strongly influences the optical properties compared to a dense film of the same material. The refractive index decreases with an increasing proportion of voids in the material (see Bruggemann effective medium approximation, EMA). For ellipsometric data analysis, the theoretical model was based on the assumption that the film consists of nanoparticles and a certain fraction of void. The model layer system was designed as follows: 0: the silicon substrate is infinitely thick (1

mm); 1: a typical layer of 2 nm thermal oxide (SiO_2) is presumed; 2: the porous film is described with a Cauchy layer. Starting with a guessed film thickness, the subsequent fitting of the thickness and the Cauchy parameters resulted in a very good overlap with the experimental data as shown in Fig. 29.
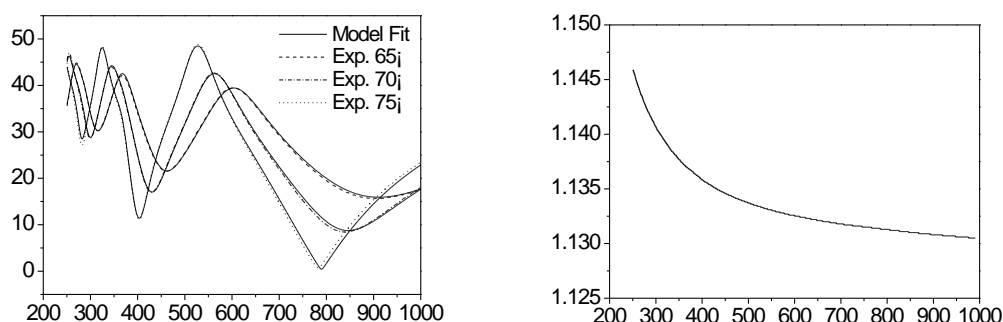

Fig. 29: Ellipsometry data of Beta-TEOS film after 6 coating steps

The determined thicknesses of the films reflect the values detected with SEM. Based on the ellipsometric data, the refractive index (*n*) of the films prepared with and without binders was determined. The *n*-values at 589 nm were used for comparison of the films. All films showed a very low refractive index, which is typical for porous silica films. Fig. 29 shows the data of a film composed of microporous particles and a binder (Beta-TEOS) prepared by spin-coating 6 times. Although the film appears dense to the eye, a refractive index of only 1.133 (589 nm) was found for this sample. Equal results concerning thickness and refractive index were achieved by replacing the Cauchy layer with an EMA layer consisting of SiO_2 and void. The total porosity was found to be 70 % in this case.

The mechanical properties of all films were investigated by tape tests. In all films except Beta-pure, the mechanical stability was very high and the film could not be removed from the silicon wafer with the tape. The highest adhesion was diagnosed in films prepared with amorphous SiO_2 binder. The efficiency of the binders mainly depends on the size of the binding particles. Small particles of SiO_2 with a high external surface are able to form many bonds (Si-O-Si) with the zeolite crystals and with the thermal SiO_2 on the silicon wafer.

Conclusion

Colloidal suspensions of zeolite Beta nanocrystals with low aluminum content were prepared and the crystallization kinetics were studied. The crystallization process was completed within seven days, and the size and the shape of the first crystalline particles detected in the crystallizing suspensions resemble the ones in the amorphous suspensions. Upon prolonged crystallization, an agglomeration in the crystallizing suspensions is observed, however the size of the crystalline zeolite Beta particles did not exceed 80 nm. The crystalline Beta was stabilized in colloidal suspensions by addition of inorganic silica-based binders and applied for the preparation of films by a spin-on process. The thickness of the films varied from 140 to 950 nm, controlled by repeating the number of coating steps, speed of deposition and Beta concentration of the coating suspensions. The Beta films exhibit good mechanical properties, smooth surfaces and show a low refractive index, which is typical for highly porous silica based materials. The refractive index of the films prepared with binders is increased slightly

due to additional amorphous silica introduced in the film, which is leading to the formation of denser layers. The spin-coating approach presented here allows for the preparation of films with variable hydrophilicity, thickness and mechanical stability on supports with different shapes and size.

4.2 Synthesis and Characterization of Functionalized Mesoporous Silica Nanoparticles

Introduction

Various synthetic methods have been developed for the preparation of periodic mesoporous materials,[80] leading to different types of morphologies, such as spheres,[81] fibers[82] or vesicles.[83] The large internal surface of these materials can be modified following two main strategies, i.e., post-synthesis functionalization (grafting)[84, 85] or in-situ functionalization (co-condensation),[22-24] thus extending the use of mesoporous materials to a wide range of applications.[86] Compared to the modification by grafting, the co-condensation reaction can be expected to improve the degree of bonding between the organic groups and the pore walls, and to result in a more homogeneous distribution of the organic groups throughout the pore structure.[27]

Common synthesis routes for mesoporous silica materials lead to particles with typical diameters of 500 nm to several microns. The synthesis of nanosized mesoporous materials has only recently received attention. Such mesoporous nanoparticles offer interesting features that are useful in a number of applications, such as chemical sensors,[87] chromatography,[88] catalysis,[89] drug delivery,[90] or polymer fillers.[91] If the particles are homogeneously dispersed in a solvent, these colloidal suspensions exhibit unique properties, for example, optical transparency. Furthermore, the utilization of very small particles improves the mass transfer of molecules into or out of the pore system. The molecular functionalization of the large internal surface of these materials can extend the range of possible applications, for example, towards selective (ad)sorption or specific catalytic activity.

The preparation of nanosized particles can be realized through various methods. Brinker et al. described an aerosol-based process resulting in a solid dry product.[92] Another strategy utilizes the addition of a non-ionic surfactant as a suppressant of particle growth through encapsulation, leading to a gel of agglomerated small particles.[93] Amoros et al.[94] presented a facile method leading to nanosized mesoporous silica using water, tetraethylorthosilicate (TEOS), and cetyltrimethylammonium cations in combination with triethanolamine (TEAH) which is supposed to act as a hydrolysis-retarding agent. However, the final product of this procedure is a gel of fused particles which cannot be redispersed.

There are only few publications describing synthesis methods that lead to colloidal suspensions of periodic mesoporous materials.[95-99] Their synthesis typically relies on procedures applying high dilutions; this can result in time-consuming subsequent processing steps. For instance, truly colloidal suspensions of well-defined mesoporous particles were obtained by Mann et al.[18, 100] by diluting and quenching the condensation reaction of TEOS in aqueous alkaline solution with a large excess of water. They could manipulate the particle size by varying the time interval for quenching. In a recent publication, Rathousky et al.[96] also describe a method for the preparation of colloidal MCM-41, working with even higher dilutions. The utilization of the polyalcohol triethanolamine can result in non-aggregated, colloidal suspensions of mesoporous silica (CMS) from concentrated solutions.[98] Round particles with wormhole structures and diameters of about 100 nm with very narrow particle size distributions were obtained in the form of stable suspensions. Tuning the reaction

conditions allowed controlling particle size down to 50 nm. Colloidal stability was even sustained after template extraction, which resulted in surface areas of about 1000 m^2 g^{-1}. Extraction of the template − in contrast to calcination − is the method of choice when organic moieties are introduced in the wall structure by a co-condensation procedure.

The method can be extended towards the generation of functionalized, hydrophilic as well as hydrophobic colloidal mesoporous silica with high yields. As described in the following, various alkoxysilanes bearing organic moieties can be incorporated into the pores of the colloidal nanoparticles using this general method.

Experimental

Two slightly different synthesis methods were used, as already described in our recent publication about the synthesis of nanosized pure mesoporous silicates,[98] and adapted for functionalization with organic moieties. All chemicals were reagent grade (98 % or higher) purchased from Sigma-Aldrich and used without further purification. The water was deionized.

Pure siliceous CMS-1: 14.3 g (96 mmol) TEAH and 2 ml (9 mmol) TEOS were combined in a 125 ml polypropylene bottle with a lid. The two-phase mixture was heated in an oil bath at 90 °C for 20 min without stirring. Immediately after taking the mixture out of the oil bath, 26.7 g of an aqueous solution (2.5 wt %) of CTAC which had been heated to 60 °C was added and the final mixture was stirred (600 rpm) for at least 3 h at 23 °C. The molar composition of CMS-1 is: 0.75 Si : 8 TEAH : 0.17 CTAC : 120 H$_2$O.

Functionalized mesoporous silica CMS-R: 14.3 g (96 mmol) TEAH and a mixture of 2.23 ml (10 mmol) TEOS plus the corresponding quantity of 2 mmol (Table 1) of organotriethoxysilane (RTES) were combined in a 125 ml polypropylene bottle with lid. The two-phase mixture was heated in an oil bath at 90 °C for 20 min without stirring. Immediately after taking the mixture out of the oil bath, 26.7 g of an aqueous solution (2.5 wt %) of CTAC which had been heated to 60 °C was added and the final mixture was stirred (600 rpm) for at least 3 h at 23 °C. The molar composition of these functionalized materials is: 1 Si : 8 TEAH : 0.17 CTAC : 120 H_2O.

Table 1: Type and amount of functionalized organotriethoxysilane used in the co-condensation

sample	RTES	M (g mol-1)	n (mmol)	m (g)
CMS-VI	vinyltriethoxysilane	190.3	2	0.381
CMS-PH	phenyltriethoxysilane	240.4	2	0.481
CMS-BZ	benzyltriethoxysilane	254.4	2	0.509
CMS-CP	3-cyanopropyltriethoxysilane	231.4	2	0.463
CMS-MP	3-mercaptopropyltriethoxysilane	238.4	2	0.477

Extraction of template from the mesoporous silica: 50 ml of ethanol were added to the translucent, colloidal aqueous suspension of the mesoporous material. The resulting precipitate was centrifuged for 20 min at 40.000 RCF (g). After decanting, the sediment was redispersed through vigorous stirring in 50 ml of an ethanolic solution of ammonium nitrate (20 g l^{-1}) and then treated for 20 min in an ultrasonic bath (35 kHz).

Alternatively the mixture can be refluxed for 1 h. This procedure was repeated until the sediment after centrifugation was completely transparent, normally one or two times. In order to replace the ammonium ions in the structure, this operation was repeated with a solution of concentrated hydrochloric acid in ethanol (5 g l^{-1}). After washing with pure ethanol, the transparent gelatinous cake obtained after centrifugation can be redispersed in ethanol, leading to a colloidal suspension of the extracted product in ethanol.

Characterization

Dynamic light scattering (DLS) data were collected with an ALV-NIBS/HPPS High Performance Particle Sizer in PMMA cuvettes at 25 °C. Raman spectroscopy was performed with a He-Ne laser (633 nm) on a LabRAM HR UV-Vis (HORIBA Jobin Yvon) Raman Microscope (Olympus BX41) equipped with a Symphony CCD detection system. The spectra were baseline-corrected. For thermogravimetric analysis (TGA) 10 mg of dry powder were heated in corundum crucibles from 30 to 800 °C (10 °C min^{-1}) in a flow of synthetic air (25 ml min^{-1}) using a Netzsch STA 449 C Jupiter thermobalance. For the SEM analysis, films were prepared on a gold-covered glass slide by spin-coating, using ethanolic suspensions of the extracted material. Shape and dimensions of the particles were determined with a JEOL JSM-6500F scanning electron microscope (SEM) equipped with an Oxford EDX analysis system. Transmission electron microscopy (TEM) was carried out on a JEOL JEM 2011 instrument with LaB$_6$ cathode at 200 kV. Samples were prepared on a Plano holey carbon coated copper grid by evaporating one droplet of diluted ethanolic suspension of the extracted material.

Cross-polarized ^{29}Si-MAS-NMR measurements were performed on a Bruker DSX Avance500 FT spectrometer in a 4 mm ZrO_2 rotor. Nitrogen sorption isotherms (77 K) were obtained using a Quantachrome NOVA 4000e Surface Area & Pore Size Analyzer. Surface area calculations were made using the Brunauer-Emmett-Teller (BET) equation in the range from $p\,p_0^{-1} = 0.05 - 0.25$. Pore-size distributions were determined using the DFT-method (NLDFT equilibrium model, cylindrical pores, N_2 on oxygen). The pore volume was determined for meso- and micropores for $p\,p_0^{-1} < 0.8$.

Results and Discussion

Colloidal mesoporous silica was prepared in the form of non-functionalized pure-silica MCM-like material (CMS) and as functionalized mesoporous materials carrying five different organic groups (R) in the pore walls (CMS-R; see Table 1).
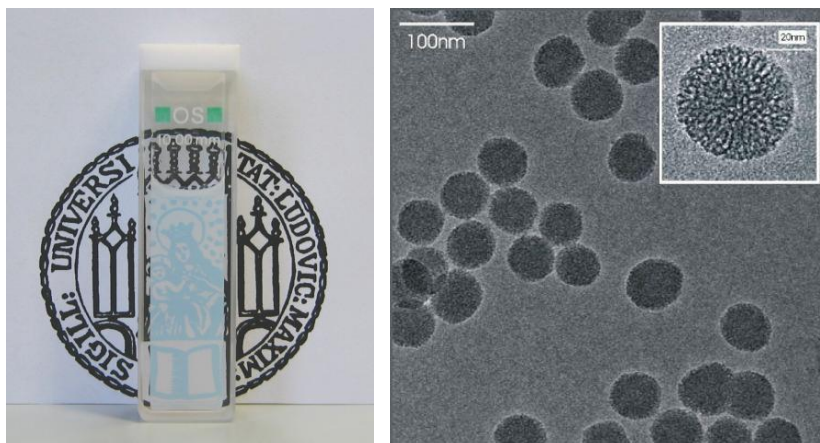
Fig. 30: Translucent colloidal suspension and TEM micrograph of functionalized mesoporous nanoparticles

The materials were obtained as colloidal suspensions with relatively uniform particle sizes between 40 and 150 nm (Fig. 30). Tetraethylorthosilicate (TEOS) and organotriethoxysilanes (RTES) form the MCM-like material in combination with cetyltrimethylammonium cations (CTMA$^+$) as structure directing agent in a co-condensation process (Fig. 31).
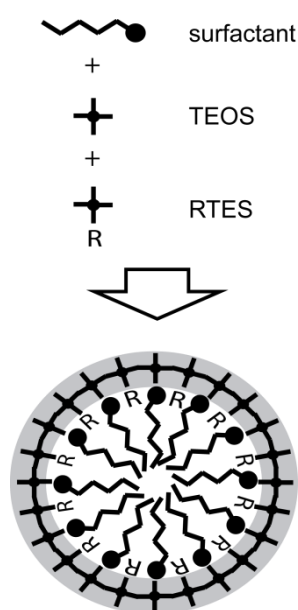

Fig. 31: Scheme of the co-condensation reaction of alkoxysilanes with a micelle-forming surfactant

This S$^+$I$^-$ assembly takes place in an alkaline aqueous medium, with triethanolamine (TEAH) as basic reactant. TEAH can also act as a complexing agent that retards the hydrolysis of the alkoxides.[101-103] The large excess of TEAH probably keeps the seeds separated from each other during the condensation process giving finally rise to a large number of particles with relatively small diameters.

The morphology and particle size of the synthesized materials was analyzed with dynamic light scattering (DLS) and electron microscopy (TEM and SEM). In the TEM micrographs discrete, near-spherical particles with a disordered, worm-like pore arrangement are observed. The particles show a narrow particle size distribution with a polydispersion index (PDI) of around 0.1. This narrow size distribution is maintained after extraction of the template by an ion-exchange method using an ethanolic solution of ammonium nitrate (Fig. 32).
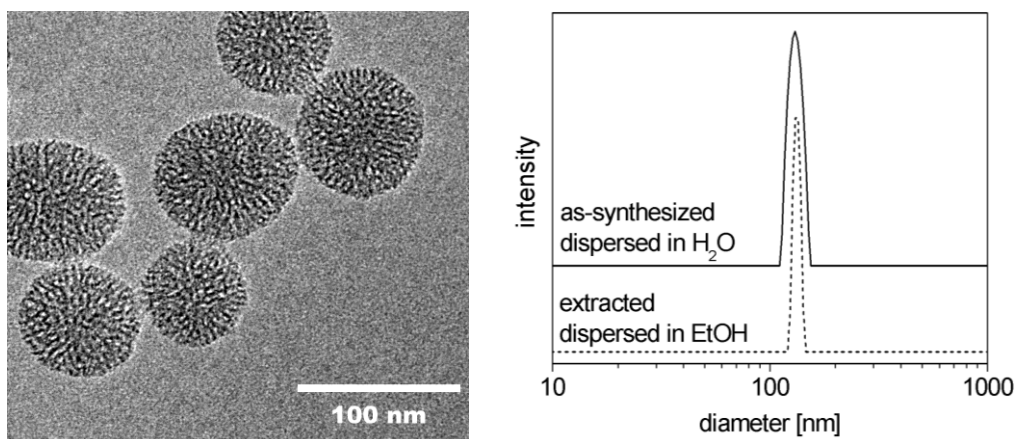
Fig. 32: TEM-micrograph and particle size distribution of sample CMS-1 determined by dynamic light scattering

The synthesis procedure developed for pure siliceous nanoparticles was extended towards a simultaneous reaction of TEOS and a variety of organotriethoxysilane precursors to obtain functionalized surfaces. Hybrid mesoporous materials incorporating the following organic groups, i.e., vinyl- (CMS-VI), benzyl- (CMS-BZ) , phenyl- (CMS-PH), cyanopropyl- (CMS-CP) and mercaptopropyl- (CMS-MP) residues were

thus synthesized. These surface-modified mesoporous organosilicas often show an even narrower size distribution than the pure silica parent materials (Fig. 33).
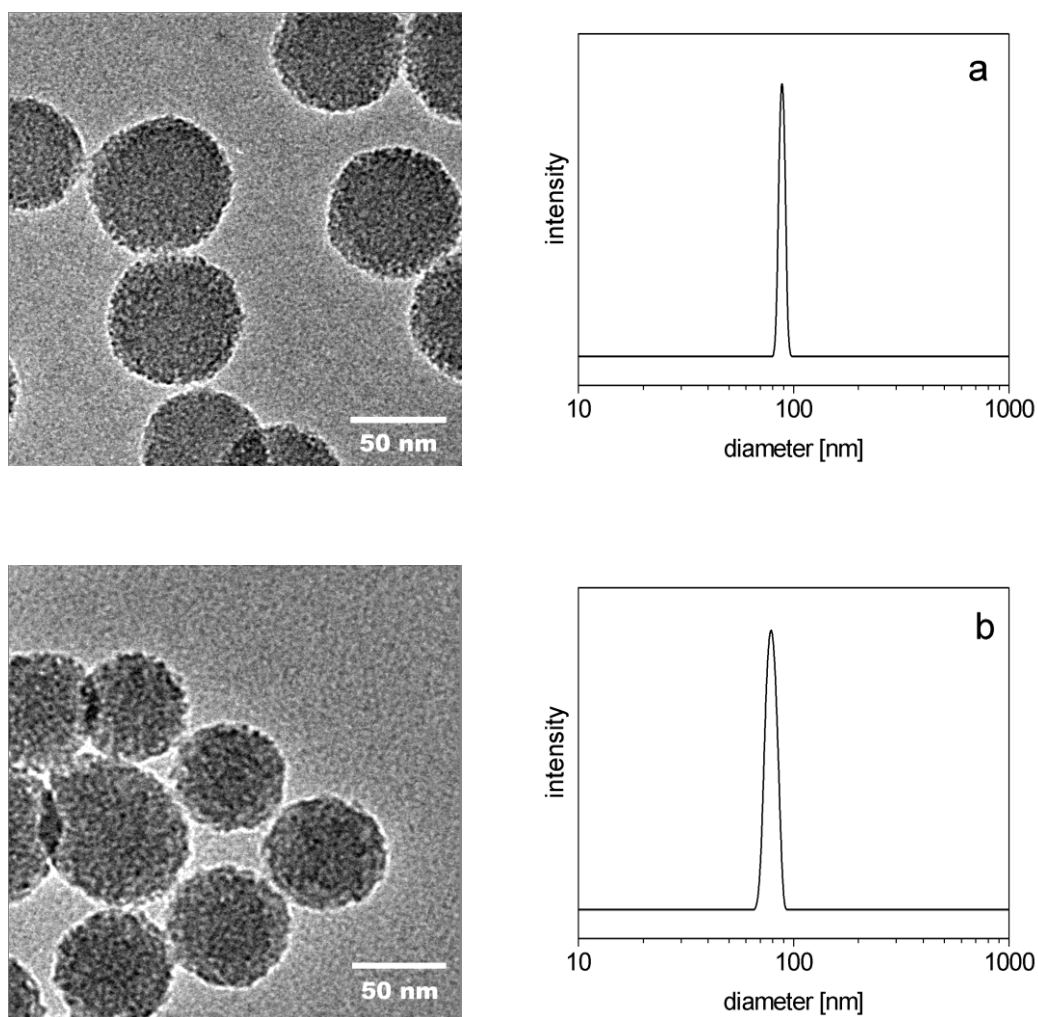

Fig. 33: TEM-micrographs and particle size distributions calculated from DLS-data of samples CMS-MP (a) and CMS-PH (b)

The observed mean particle size obtained from DLS measurements varies in most cases from about 50 to 150 nm, depending on the incorporated functional group and the

synthesis method employed. The particle size observed with electron microscopy is often slightly smaller than the hydrodynamic diameter measured by DLS. This observation can be explained with occasional weak aggregation of the particles. The discrepancy is seen clearly in the case of the organically modified materials, especially, if hydrophobic aromatic groups, such as phenyl residues are incorporated in the structure (Table 2).

Table 2: Properties of colloidal mesoporous materials as analyzed with different methods

sample	Particle size		TGA data	N$_2$ sorption data		
	diameter DLS (nm)	diameter TEM (nm)	T at DTG$_{max}$ (°C)	surface area (m^2 g^{-1})	pore volume at $p\,p_0^{-1} < 0.8$ (cm^3 g^{-1})	pore diameter (nm)
CMS-1	100	80–120	-	1150	1.0	4.0
CMS-VI	120	50–100	290	1230	0.74	3.4
CMS-CP	130	80–150	350	1200	0.72	3.3
CMS-MP	90	50–70	350	970	0.63	3.4
CMS-PH	80	40–60	610	1040	0.73	2.8
CMS-BZ	110	50–100	470	1120	0.65	3.2

The products with incorporated organic groups, especially CMS-PH or CMS-MP, appear as nearly perfect spheres with diameters of about 50 nm. The narrow particle size distribution of the mesoporous materials can also be confirmed with scanning

electron microscopy (Fig. 34). Here, a stable colloidal suspension of extracted CMS-BZ was used for spin-coating a gold-sputtered glass plate resulting in a homogeneous coverage of mesoporous particles. The benzyl-modified mesoporous spheres have diameters in the range of 50 to 80 nm.
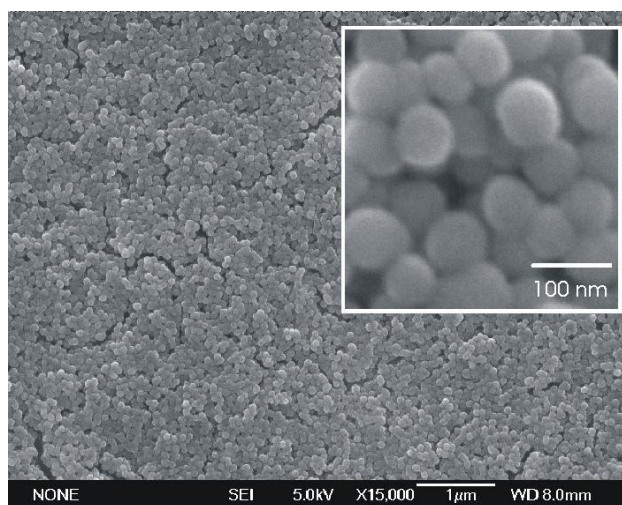

Fig. 34: SEM-micrograph of a mesoporous film prepared by spin-coating, using a colloidal suspension of CMS-BZ

An influence of organic functional surface groups upon the morphology of mesoporous materials was also observed by Huh et al.[24] They found a strong increase of the particle size when using hydrophilic organosilanes, especially with amino-containing residues, while hydrophobic residues stimulated the formation of smaller particles. They concluded that hydrophobic groups are able to align with the organic tails of the template, while hydrophilic residues would disturb the Gouy-Chapman region thus causing a different growth behavior. The results for the hydrophobic functional groups

support their findings. Weakly acidic mercapto residues also stimulate the formation of small spherical particles.[99]

The presence of the organic functional groups can be verified with several methods. Thermogravimetric analysis (TGA) shows the decomposition behavior during the heating of the samples in air. The decomposition temperature, more precisely the temperature when the first derivative of the weight loss reaches a maximum, varies over a rather wide range for the different functional groups (Fig. 35 and Fig. 36).
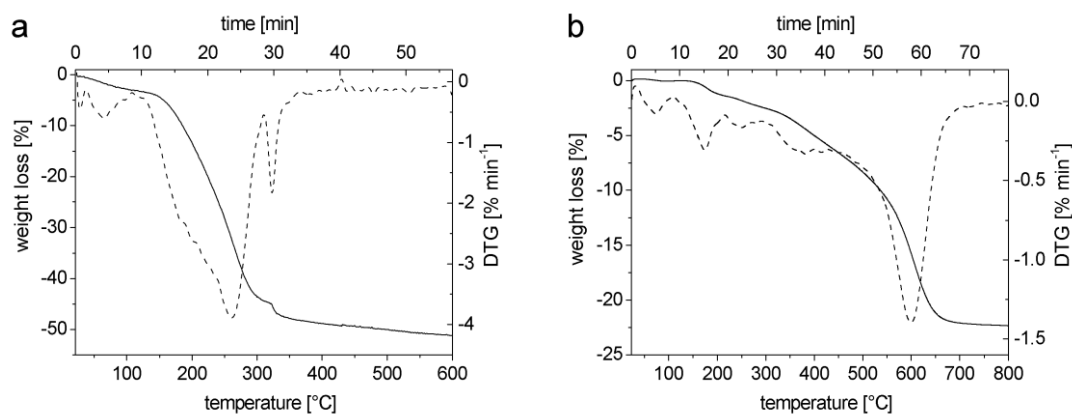
Fig. 35: Thermogravimetric analysis (TG-DTG) of washed CMS-1 with template (a), and phenyl modified, extracted mesoporous silica CMS-PH (b)

Fig. 35a shows the weight-loss of the washed non-functionalized sample CMS-1, still containing the template inside the pores with a maximum around 250 °C. This decomposition process of the template is completed well before the decomposition of the phenyl-residue in sample CMS-PH starts. Fig. 35b shows the decomposition of this group around a temperature of 600 °C in a sample that was previously template-extracted. This extreme stability is not observed for the other functional groups. They

start to decompose at a lower temperature, which makes a clear separation from the degradation of the template difficult (Fig. 36). However, when non-functionalized samples were analyzed with TGA after template extraction, a weight loss of around 4-7 wt % between 100 and 500 °C is still observed. Residual template fragments that were detected by elemental analysis of non-functionalized samples can account for about 3 % weight loss. Additionally, the dehydroxylation of surface hydroxyl groups should be considered. Usually up to 3 SiOH groups per nm^2 are found in mesoporous materials.[97, 104] With surface areas of about 1000 m^2 g^{-1} one can estimate a maximum 5 wt % loss due to water release from these samples by dehydroxylation.
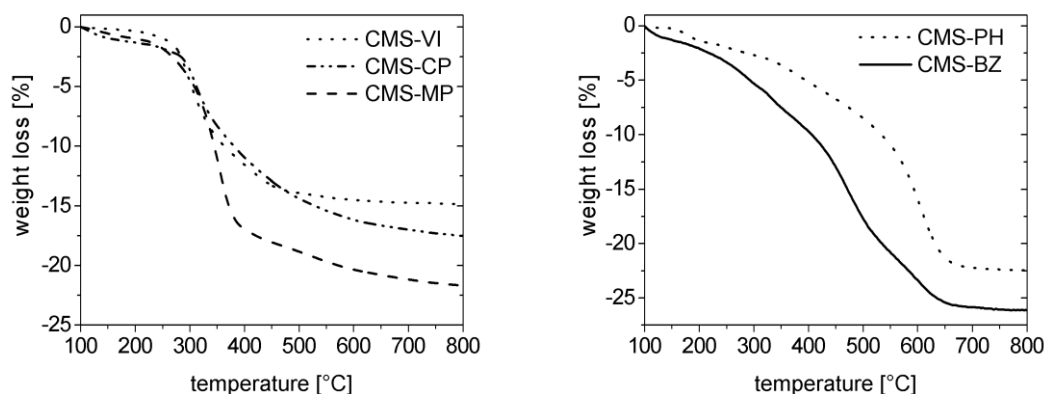
Fig. 36: Thermogravimetric analysis of the surface-modified and extracted mesoporous
silica materials (starting at 100 °C to compensate for different water losses)

This loss must be taken into account when the amount of organic residue is determined from TGA measurements. Usually a TGA weight loss between $15-25$ wt % in template-extracted functionalized samples occurs (above 100 °C).

The connectivity of the functional organic groups to the silica framework is best demonstrated by cross-polarized ^{29}Si-MAS-NMR spectroscopy (Fig. 37).
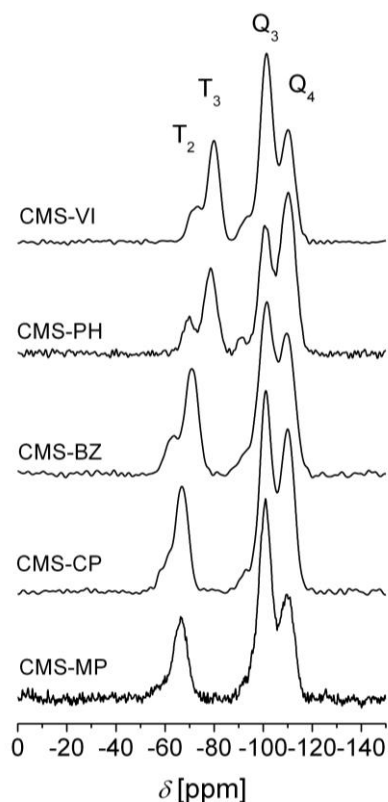

Fig. 37: Cross-polarized ^{29}Si-MAS-NMR spectra of the functionalized mesoporous materials

The spectra show peaks at -110 ppm (Q^4) and -102 ppm (Q^3) [$Q^n = Si(OSi)_n(OH)_{4-n}$], n = 2–4 representing the fully condensed silica and silica with one terminal hydroxyl group. Geminal hydroxyls are barely present in these samples (resonance at -92 ppm; Q^2). One or two additional peaks are observed due to the T^2 and T^3 resonances of the incorporated organosiloxanes [$T^m = RSi(OSi)_m(OH)_{3-m}$], m = 2–3 at values commonly

observed in functionalized mesoporous materials. Propyl-bridged functional groups display shifts around -67 and -60 ppm, while directly bound residues with C=C bonds show resonances at more negative values (Table 3).[24] The prevalence of the T^3 peak, i.e., the threefold coordination of the siloxane indicates (near) complete condensation of the functional groups into the wall structure of the nanoparticles.

Table 3: Cross-polarized ^{29}Si-MAS-NMR spectroscopy data of functionalized mesoporous materials

sample	chemical shift			
	Q^4	Q^3	T^3	T^2
CMS-VI	-110	-101	-80	-73
CMS-PH	-110	-101	-79	-70
CMS-BZ	-110	-101	-71	-63
CMS-CP	-110	-101	-67	-58
CMS-MP	-110	-101	-67	-

The characteristic vibrational modes of the incorporated functional groups are clearly displayed in their Raman spectra, which are not obscured by hydroxyl vibrations of the host as in IR spectroscopy (Fig. 38). Intensive peaks of the phenyl- and benzyl-substituted samples CMS-PH and CMS-BZ, originating from the in-plane C-H deformation vibrations of the aromatic ring, are seen at about 1000 cm-1. Additionally, these samples show the typical peaks for aromatic C-H and ring C=C stretching vibrations at 3060 and 1590 cm-1, respectively.[105]

In the vinyl-modified sample (CMS-VI) we find the alkene C-H vibrations and the C=C stretching vibrations at 3070 and 1605 cm^{-1}, respectively. The nitrile group of CMS-CP causes a characteristic narrow band at 2250 cm^{-1}. The typical peak for the S-H group in the mercaptopropyl-containing CMS-MP occurs at 2580 cm^{-1}, and additionally we find a band at 657 cm^{-1} due to the C-S vibration. Both Raman bands indicate that the mercapto groups are intact and that no disulfide bridges have formed.[106]
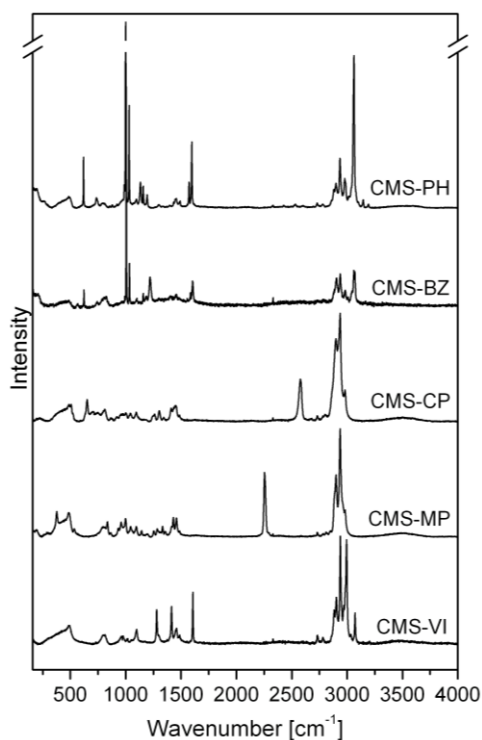
Fig. 38: Raman spectra of template-extracted functionalized mesoporous materials

After extraction of the surfactant, the functionalized porous materials show high surface areas and pore volumes. The sorption properties were determined using nitrogen

adsorption-desorption at 77 K. In case of the unmodified materials CMS-1, a typical type IV isotherm with a clear hysteresis from filling of the cylindrical pores is observed. Textural pores of ~20 nm, originating from the closely packed nanospheres in the powders are visible above a relative pressure of $0.8 \, p \, p_0^{-1}$. The entire surface area calculated according to the BET-theory is 1150 $m^2 \, g^{-1}$ for CMS-1. The product exhibits a high pore volume of 1 $cm^3 \, g^{-1}$ (for $p \, p_0^{-1} < 0.8$) and a narrow pore size distribution with an average diameter of 4 nm as determined with the DFT method (Fig. 39). Calcined CMS-1 shows an even higher surface area of 1400 $m^2 \, g^{-1}$ with pore volumes of 1.1 $cm^3 \, g^{-1}$.
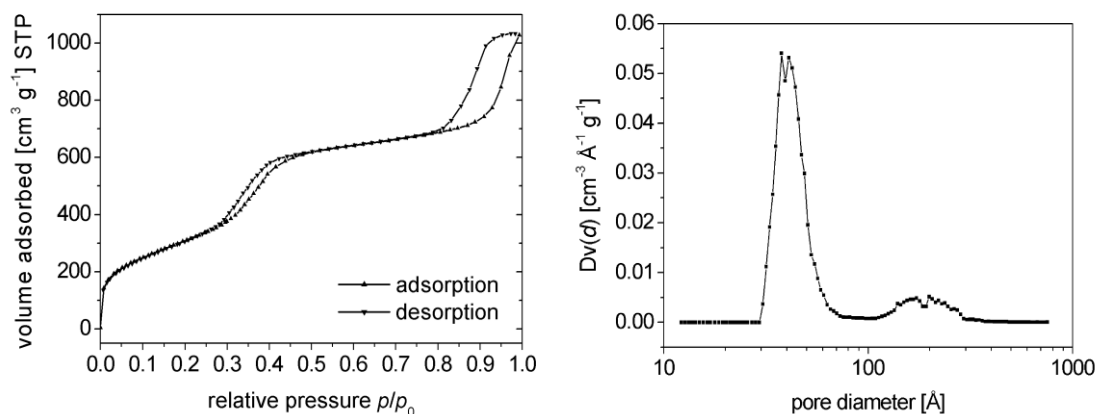
Fig. 39: Nitrogen sorption isotherm (left) and pore size distribution (right) according to the DFT theory of mesoporous silica CMS-1

The type of adsorption isotherm is unchanged in the functionalized nanosized materials, and the inclusion of the functional groups does not significantly affect the overall surface area of the materials (Fig. 40).
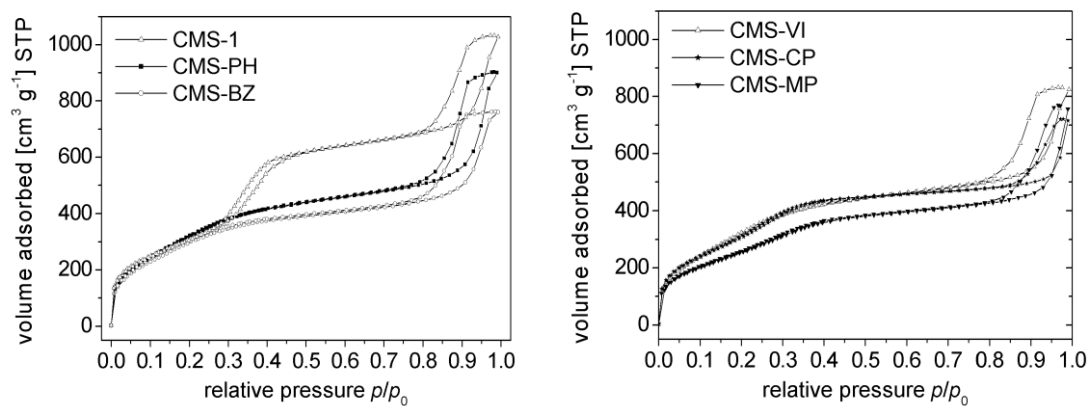
Fig. 40: Nitrogen sorption isotherms of reference and co-condensed materials

To some extent the size of the functional groups influences the shrinkage of the pore diameter. While the unmodified mesoporous silica has an average pore diameter of 4.0 nm, in vinyl-functionalized materials (CMS-VI) we find pores with a mean diameter of 3.4 nm, and the bulky nature of the benzyl group in CMS-BZ causes a reduction to 3.2 nm (Fig. 41).
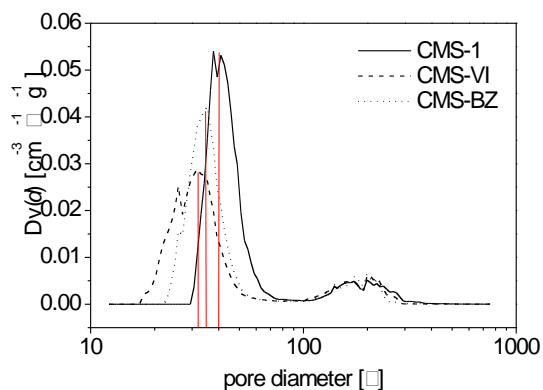
Fig. 41: Changes in the pore size distribution with increasing size of the incorporated organic moieties in mesoporous silica

The surface coverage of functional groups in the nanoscale mesoporous samples can be estimated from thermogravimetric measurements in conjunction with the surface area presuming that all organic groups are located on the surface. For example, the weight-loss of CMS-PH due to the decomposition of the organic group is about 20 %. The calculated surface area according to BET-theory is 1040 m^2 g^{-1}. From these data, a surface coverage of 2.6 mmol g^{-1} or 1.5 phenyl groups per nm^2 can be calculated.

Conclusion

The synthetic approach presented here can serve as a general method for the preparation of both colloidal mesoporous silica spheres (CMS) and functionalized colloidal suspensions of nanoscale mesoporous materials with high yields from concentrated solutions. Narrow particle size distributions in the range of about 50 to 150 nm were established with Dynamic Light Scattering (DLS) measurements and electron

microscopy before and after template extraction. Discrete nanoscale mesoporous particles with functionalized pore surfaces result when adding functional organoalkoxysilanes directly to the initial silica precursor solutions. Nitrogen sorption analysis and indicates that the functional groups are located at the inner surfaces of the mesoporous channel systems.

4.3 Porous Thin Films of Functionalized Mesoporous Silica Nanoparticle

Introduction

Porous materials in the nanometer range already attract a great deal of interest in many fields of science and technology. Especially in terms of colloidal suspensions, these materials are promising candidates for applications such as gas sensing, host-guest chemistry, drug delivery and coatings in the semiconductor industry. The preparation of monodisperse, stable colloidal suspensions of mesoporous silica particles has been recently developed.[98, 99] The synthesis parameters were gradually modified in order to realize even smaller particles in the range below 40 nm. As reported in the previous publications, the introduction of functional groups during the co-condensation reaction has a great influence on the particle shape and size.[24] The synthesis with phenyltriethoxysilane led to particles with a smallest diameter of only 50 nm.[107] Additionally, the phenyl-modified particles are thermally more stable, easy to characterize and tend to peptize (disperse) more easily due to their sterically demanding and inert aromatic rings.

By further decreasing the diameter of these mesoporous silica spheres, their scattering ability for visible light is also drastically decreased. If the size of the particles falls below about 1/10 of the wavelength of the incoming light (0.1 λ), their scattering ability can no longer be described with the Lorenz-Mie-solution but with Rayleigh scattering. The colloidal suspensions thus show optical transparency when the particle size is small enough. Due to this optical transparency, such nanoparticles would allow spectroscopic investigations of physical processes or chemical reactions in a confined space. Furthermore, it is possible to encapsulate sensitive dyes [108-111] or to facilitate the

dispersion of the particles in certain media. Modifying the spheres with appropriate functionalities such as caps or fluorescence markers would make them interesting candidates for drug delivery[7, 108] or would permit observing their way into a cell.[112, 113] Another very promising area of application is thin film technology.[114, 115] The synthesis of mesoporous thin films is often achieved with the so-called "Evaporation Induced Self Assembly" (EISA) process.[20] The EISA process for mesoporous silica thin films starts with a homogeneous solution of silica precursor and surfactant prepared in ethanol/water with an initial surfactant concentration much below the critical micelle concentration.[20] Upon dip-coating or spin-coating, the preferential evaporation of ethanol concentrates the surfactant and silica species. The progressively increasing surfactant concentration drives self-assembly of silica-surfactant micelles and their further organization into liquid-crystalline mesophases. This approach represents a versatile strategy for the formation of mesoporous silica and other oxide thin films with different pore sizes, pore topologies and elemental composition.[116]

However, there are several issues that suggest the development of complementary strategies. The precursor is normally highly acidic which can cause problems on sensitive substrates. Removal of the template by extraction or calcination might also be critical. If the surfactant is removed thermally, cracks can occur in thicker films, and it is known that the humidity has a great influence on the film formation. Thus, if the orientation of the pores is less important, the alternative preparation of thin films with mesoporous nanoparticles can address several of these issues. It is believed that a porous thin film made of porous nanoparticles can exhibit improved diffusion properties

and a highly accessible pore system.[50] Additionally, one can work with stable suspensions of already extracted nanoparticles, thus ensuring an easy handling and good reproducibility. The coating of sensitive substrates is facilitated due to the mild conditions. Control over the thickness can be attained by varying the concentration or by multiple step coating. It could be also feasible to combine suspensions containing different kinds of nanoparticles in order to assemble hybrid thin films. Finally, the material is easier to characterize when bulk samples are available. The synthesis of completely transparent suspensions even after template extraction would be a great improvement for the formation of homogeneous thin films with a low surface roughness. Especially for the formation of multilayers, it is advantageous if the film is very smooth. Otherwise the defects on the surface are transmitted and amplified with every following coating step. Furthermore, the availability of such homogeneous porous thin films makes it possible to use ellipsometric porosimetry as an analysis method. This method has a set of advantages compared to conventional sorption methods, which are specified in a work of Eslava et. al:[56]

For an accurate determination of sorption isotherms of porous coatings via gravimetric or volumetric methods, an extremely sensitive device is needed. The tiny amount of porous material and the weight increase due to adsorption in the thin film can be detected with a surface acoustic wave (SAW) device or a quartz crystal microbalance (QCM). In both cases, the coating has to be applied to the measuring device itself, which might have an influence on properties such as the orientation of the crystals, the presence of grain boundaries, and the film thickness. Scraping off from their supports

and collecting a sufficient quantity of powdery sample for a conventional determination is a drastic intervention. The determination of sorption isotherms of a thin film via ellipsometric porosimetry (EP) is a convenient method to determine the effective porosity and pore size distribution of a thin film on its original support without destroying it.

Thus, the aim of this work was the synthesis of monodisperse colloidal suspensions of porous nanoparticles with a particle size small enough for the preparation of homogeneous thin films. Additionally, the porosity of the final thin films is determined with different methods.

Experimental

All chemicals were purchased from Sigma-Aldrich with reagent grade (98 % or higher) and used without further purification. The water was deionized. In order to guarantee the same conditions for all samples, the syntheses were carried out in a heatable high-throughput magnetic stirrer (1000 rpm) in 100 ml glass test tubes (diameter: 2.5 cm). Although it is necessary that the synthesis mixture be well stirred, building of foam should be avoided in order to prevent the formation of inhomogeneities. The following solutions were prepared and used for all syntheses: **S1** (surfactant): 30.0 g aqueous solution of cetyltrimethylammonium chloride (25 wt %) and 270.0 g deionized water. **C1** (catalyst): 1.0 g triethanolamine (TEAH) and 9.0 g deionized water. **P1** (precursor): 20.8 g (0.1 mol) tetraethylorthosilicate (TEOS) and 2.4 g (0.01 mol) phenyltriethoxysilane (PTES). **E1** (extraction): 50 g concentrated hydrochloric acid

(37% HCl) in 500 ml ethanol. **E2** (extraction): 10 g ammonium nitrate in 500 ml ethanol.

Samples CMS-P*xy*

20.0 g **S1** and 0.20 g (CMS-P2*y*), 0.40 g (CMS-P4*y*) or 0.80 g (CMS-P8*y*) **C1** were heated under stirring to 60 °C (CMS-P*x*6), 70 °C (CMS-P*x*7) or 80 °C (CMS-P*x*8). The amount of 1.60 ml **P1** was added and stirring was continued in the test tube for 1 h. The vessel was kept open in order to evaporate parts of the ethanol that were formed during the condensation. For a better overview, all samples are listed in Table 4:

Table 4: Prepared samples and synthesis conditions:

sample	synthesis temperature	amount TEAH (g)
CMS-P26	60 °C	0.02
CMS-P46	60 °C	0.04
CMS-P86	60 °C	0.08
CMS-P27	70 °C	0.02
CMS-P47	70 °C	0.04
CMS-P87	70 °C	0.08
CMS-P28	80 °C	0.02
CMS-P48	80 °C	0.04
CMS-P88	80 °C	0.08

Extraction

The resulting colloidal suspension was flocculated with 20 ml **E1** and the cloudy precipitate was centrifuged for 5 min at 40000 g (RCF). After decanting, the sediment was redispersed through vigorous stirring in 20 ml **E2**. The clear suspension was treated for 10 min in an ultrasonic bath. After flocculating with 20 ml deionized water, the precipitate was again centrifuged, the sediment was redispersed in 20 ml **E1** and again sonicated. After flocculation with 20 ml deionized water and centrifugation, the sediment can be redispersed in ethanol, leading to a suspension of colloidal mesoporous silica (CMS) with approximately 5 wt % solid content.

Film preparation

Thin film preparation was performed by spin-coating with an ethanolic suspension containing about 5 wt % of solid material. The substrate (silicon or glass) was coated 3 times at 3000 rpm (acceleration: 5000 rpm s^{-1}). In order to remove potential inhomogeneities, the transparent ethanolic suspension was filtered through a 0.2 μm syringe filter prior to spin-coating.

Characterization

Dynamic light scattering (DLS) data were collected with a Malvern Nano ZS in PMMA cuvettes at 25 °C. For thermogravimetric analysis (TGA) 10 mg of dry powder were heated in corundum crucibles from 30 to 900 °C (10 °C min^{-1}) in a flow of synthetic air (25 ml min^{-1}) using a Netzsch STA 449 C Jupiter thermobalance. Transmission electron

microscopy (TEM) was carried out on a FEI Titan 80-300 at an accelerating voltage of 300 kV. Samples were prepared on a Plano holey carbon coated copper grid by evaporating one droplet of diluted ethanolic suspension of the extracted material. The nitrogen sorption isotherms (77 K) were obtained using a Quantachrome NOVA 4000e Surface Area & Pore Size Analyzer. Surface area calculations were made using the Brunauer-Emmett-Teller (BET) equation in the range from $p\,p_0^{-1} = 0.05 - 0.25$. Pore-size distributions were determined using the DFT-method (NLDFT equilibrium model, cylindrical pores, N_2 on carbon). Ellipsometry measurements were performed with a Woollam M2000D at different angles (65°, 70°, and 75°) in the spectral range of 190 – 1000 nm. The data were fitted in the range between 250 – 1000 nm using the Cauchy material as model layer. Ellipsometric porosimetry measurements were carried out in a closed cell at different partial pressures at a measurement angle of 75°. The recording of isotherms was performed using a homemade Labview-controlled gas mixer. Digital mass flow controllers (W-101A-110-P, F-201C, Bronkhorst High-Tech) ensured the accurate dosing of the carrier gas nitrogen and the liquid analyte, which was vaporized in a controlled evaporation and mixing element (W-101A, Bronkhorst High-Tech). Partial pressures were calculated using the van der Waals equation. For a better comparison, with nitrogen sorption the relative pressure $p\,p_x^{-1}$ (p_x: saturation pressure) is used for the vapor sorption analysis.

Results and Discussion

The synthesis results are in good accordance with the expectations based on the work of Stöber[12] and LaMer.[13] A first variable of course is the amount of precursor added to the synthesis. In a certain range decreasing the amount of precursor can reduce the size of the final particles. According to Stöber, the particle size distribution passes a maximum when the concentration is varied, because the concentration of precursor influences not only the growth of the seeds but also the nucleation rate und thus the number of initial seeds. Since high yield is a priority, it is more interesting to choose other options for a successful downsizing. The experiments show that the final particle size in the resultant suspensions (CMS-P26 – CMS-P88) is dependent on the amount of added TEAH and the reaction temperature. In Fig. 42, the hydrodynamic diameter of all samples is shown (CMS-P**86** stand for synthesis with 0.0**8** g TEAH at **6**0 °C).
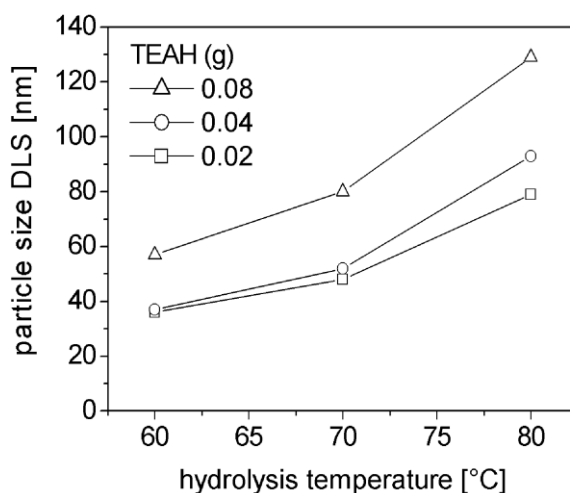
Fig. 42: Initial particle size (DLS) of samples CMS-P26 – CMS-P88

With increasing temperature and amount of catalyst (TEAH), the hydrolysis of the precursor and condensation of the nanoparticles is supported and the reaction is faster. In this specific range, these changes apparently promote the growth rate more than the nucleation rate, resulting in bigger particles. Fig. 43 shows micrographs (TEM) of samples synthesized at different temperatures with the same amount of TEAH (CMS-P8*y*). The difference in size can be clearly seen; the particles that formed at 60 °C (CMS-P86) show the smallest diameter of only 15 nm. At 70 and 80 °C the diameter reaches 25 and 30 nm, respectively.
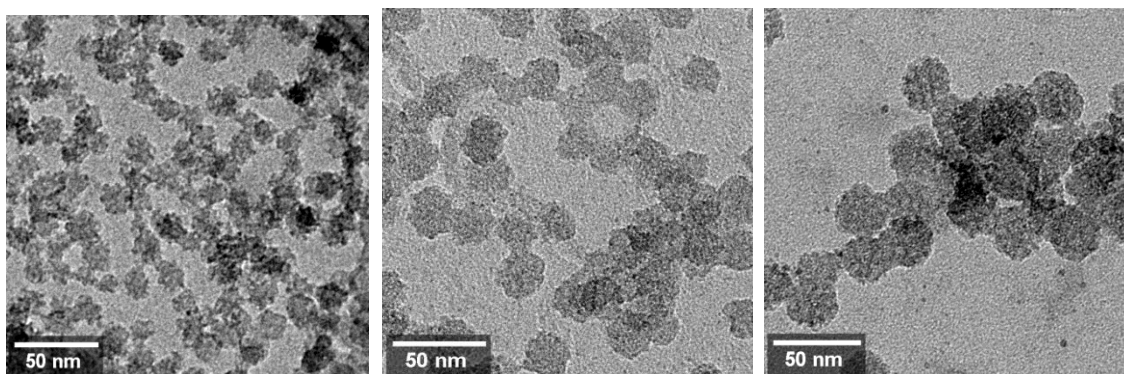
Fig. 43: Electron micrographs (TEM) of samples CMS-P86, CMS-P87 and CMS-P88

In agreement with DLS data, TEM also shows that the variation of the amount of catalyst TEAH at a constant reaction temperature (80 °C, CMS-*x*8) has an influence on the particle size. The difference is less pronounced, but the general tendency can be confirmed. The diameter varies between 22 nm (CMS-P28), 25 nm (CMS-P48) and 30 nm (CMS-P88) if the quantity of TEAH is increased.
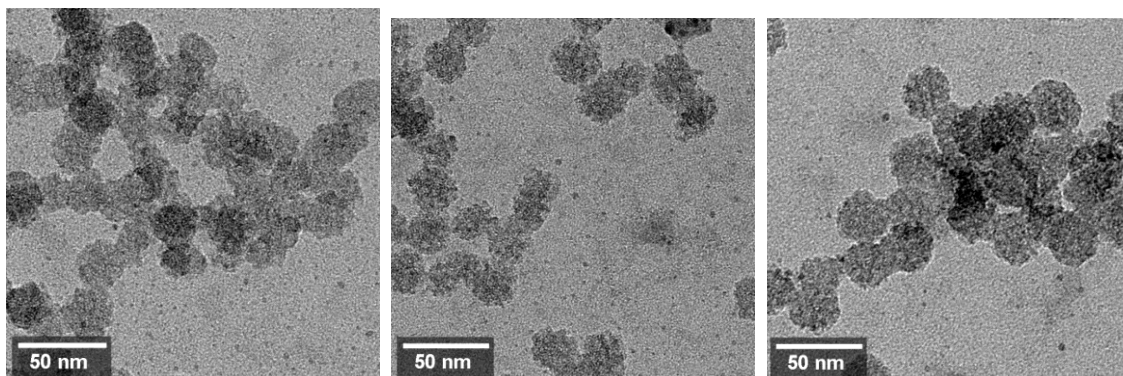
Fig. 44: Electron micrographs (TEM) of samples CMS-P28, CMS-P48 and CMS-P88

Table 5 shows a comparison of DLS and TEM data for selected particle sizes. The divergence in hydrodynamic diameter in DLS (36 - 130 nm) and discrete particle size in TEM (15 - 30 nm) could be explained with a higher degree of agglomeration at higher temperatures.

The findings made it possible to synthesize colloidal suspensions of functionalized, mesoporous silica nanoparticles with a very small particle size between 15 and 30 nm. As the scattering intensity (I) of light strongly decreases with smaller particles size ($I \sim$ radius^{6}), the suspensions with the smallest diameter (~ 15 nm) are completely clear (Fig. 45).
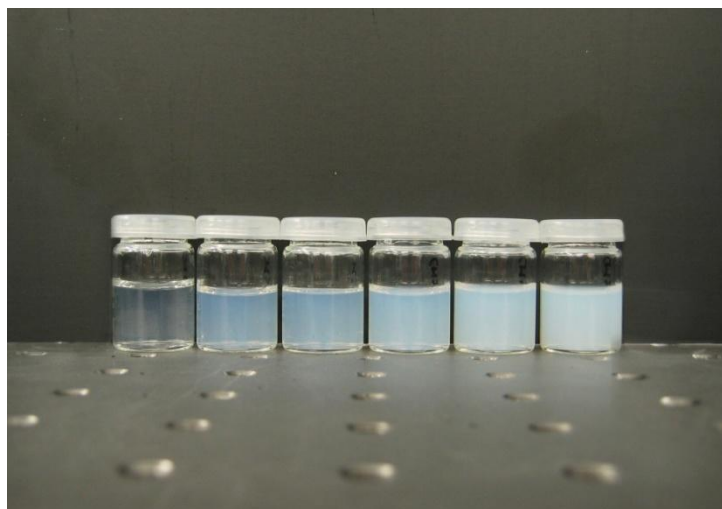
Fig. 45: Scattering of the initial colloidal suspensions containing particles with different diameters (DLS) in the range between about 40 to 130 nm (from left to right: CMS-P27, -P86, -P28, -P87, -P48, -P88)

When reaching a certain size, separating particles with centrifuges becomes difficult, as the effective gravitational force is dependent on the mass of the particles. An elegant method to overcome this problem is the flocculation of the particles. Therefore, acidified ethanol was added to the aqueous colloidal suspension leading to a cloudy suspension of agglomerated particles. The particles then could be separated from the solution by centrifugation and were purified in the following steps. The final gelatinous sediment can be completely redispersed in ethanol, leading to transparent colloidal suspensions with almost exactly the initial particle size distribution in DLS. Fig. 46 shows the mean hydrodynamic diameter of CMS-P86 before and after template extraction. The polydispersity index (PDI) of all suspensions was below 0.2. The suspensions with a diameter below 40 nm are completely transparent to the visible part of the light and show nearly no scattering.
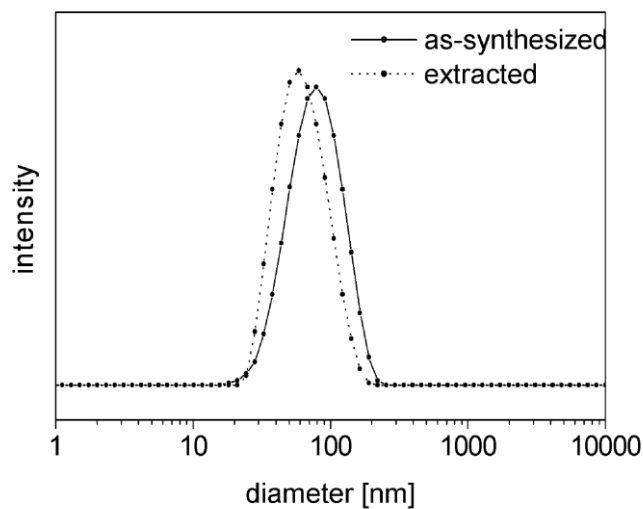
Fig. 46: Hydrodynamic diameter of CMS-P86 before and after template extraction

In transmission electron microscopy (TEM) the diameter of the particles can be specified as significantly smaller (by a factor of 3) than in dynamic light scattering. Fig. 47 shows micrographs of CMS-P86 with an average particle diameter around 20 nm. The size distribution of the discrete particles is very narrow. High resolution images clearly show the porous nature of the functionalized particles.
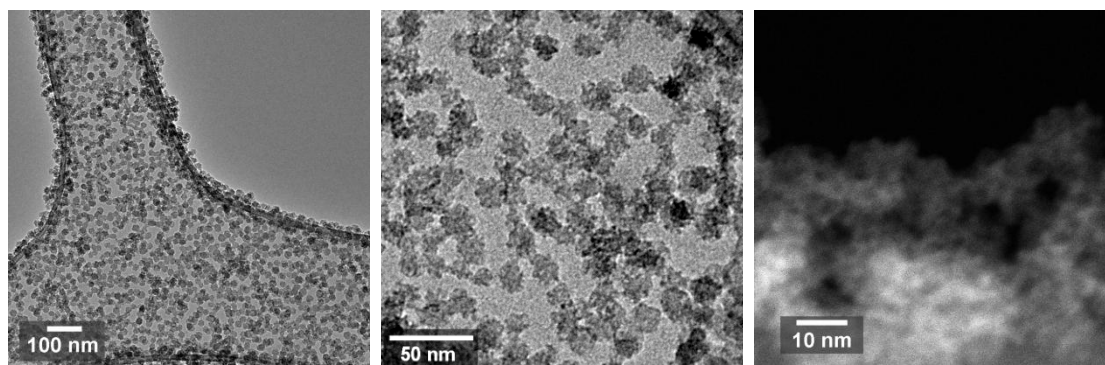
Fig. 47: TEM micrographs of CMS-P86 (right: HAADF-STEM)

In order to investigate the sorption properties of the porous nanoparticles, the ethanolic suspensions were dried at 60 °C. The resulting solids were colorless and transparent, consisting of small platelets with about 1 mm diameter. Despite of its dense appearance, the material has a high specific surface area of 640 $m^2 g^{-1}$ as well as a high pore volume (0.95 $cm^3 g^{-1}$) in the case of CMS-P86. DFT calculations resulted in a bimodal pore size distribution
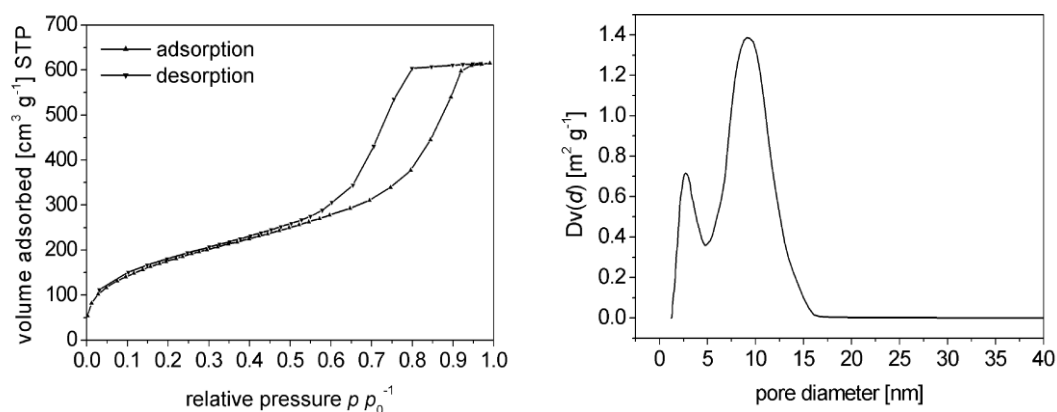
Fig. 48: N_2 sorption data of dried, extracted CMS-P86

The first peak at 2.7 nm due to templated mesopores is in the expected range for functionalized mesoporous silica templated by hexadecyltrimethylammonium ions. The second peak around 10 nm reflects the textural porosity of the material. It is a widely accepted concept that an inscribed sphere between adjacent spheres is an approximate shape for the access opening to the interstitial void space between randomly packed spheres.[117-119] Depending on the packing of the individual particles, the pore opening varies approximately between 0.2 and 0.6 times the radius of the equally sized particles. In the case of CMS-P86, this interparticle porosity is in the range between 5 and 15 nm (compare Fig. 48).

Thus, the expected particle size based on sorption is about 25 nm, which coincides well with the observed diameter in the TEM. With decreasing particle size this second peak is shifted to smaller pore sizes as shown in Fig. 49. The maximum of the interparticle porosity is in the expected range for all samples (see Table 5).
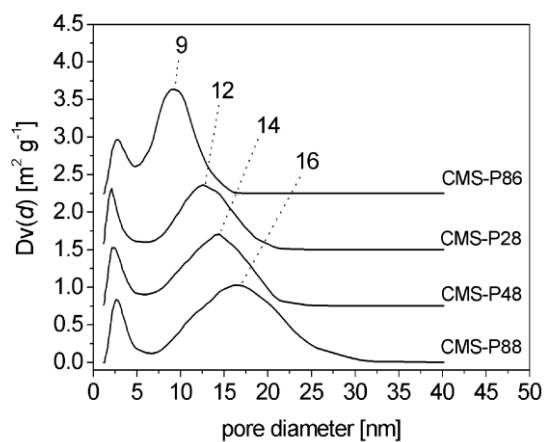
Fig. 49: Pore size distribution from N$_2$ sorption of differently sized mesoporous
particles with maximum for interparticle porosity

Table 5: Particle size (DLS, TEM) and maximum in interparticle porosity (N$_2$ sorption):

sample	hydrodynamic diameter (DLS)	diameter (TEM)	max. interparticle porosity
CMS-P88	130	30	16
CMS-P48	95	25	14
CMS-P28	80	22	12
CMS-P87	80	25	14
CMS-P86	60	15	9

Homogeneous Thin Films

The ethanolic suspensions of the template-free material are ideal candidates for the preparation of homogeneous spin-on thin films. The dry bulk material exhibits a high surface area even though it appears to be a dense solid. Thus, one can expect a high porosity for the corresponding thin film. Fig. 50 shows an image of a silicon wafer with a thin film of mesoporous functionalized silica with a thickness of 650 nm. The film was prepared by spin-coating three times with an ethanolic suspension containing 5 wt % of CMS-P86.
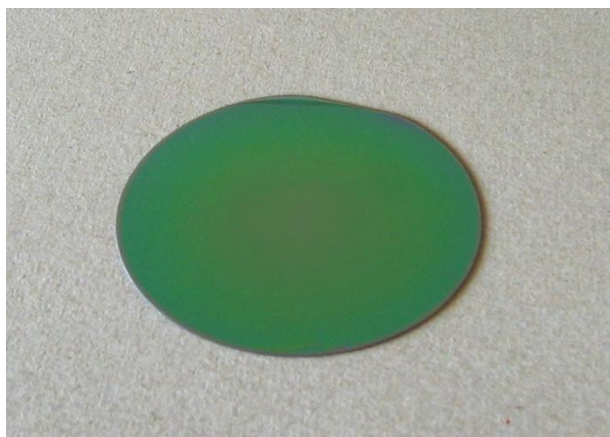
Fig. 50: Thin film of CMS-P86 on a silicon wafer

The film appears very homogeneous and transparent and thus has a definite interference color. Due to pronounced capillary forces occurring during the solvent evaporation, the nanoparticles are very closely packed – a phenomenon that also assists in the assembly of colloidal crystals.[120] Because of the smooth surface, no scattering is observed, which makes the films perfect candidates for ellipsometry investigations. Modeling and fitting

of the data was based on the assumption that the film consist of porous nanoparticles, the model layer is designed as follows:

0: the silicon substrate is infinitely thick (1 mm); 1: a typical layer of 2 nm thermal oxide (SiO_2) is presumed; 2: the material (organic functionalized silica) is described with a Cauchy layer. Starting with a guessed film thickness of 500 nm, the subsequent fitting of the thickness and the Cauchy parameters resulted in a 650 nm thick film. As show in Fig. 51, this model layer fits exactly the experimental data.
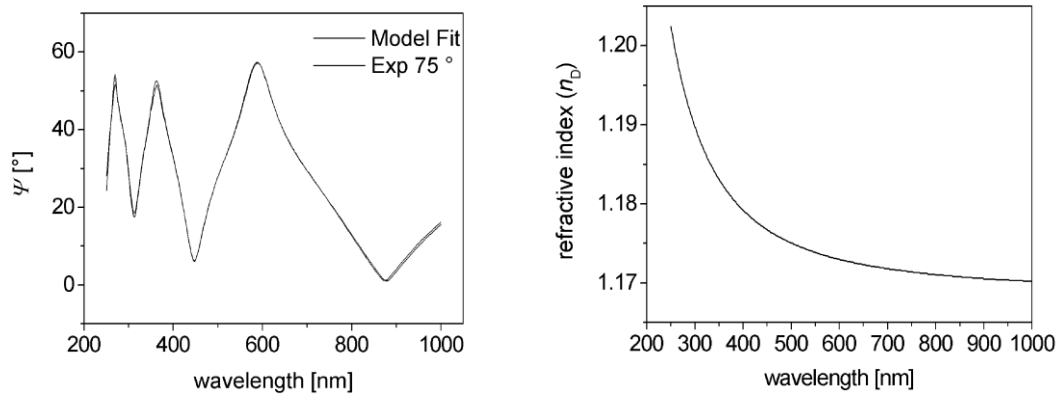
Fig. 51: Ellipsometry data of a thin film of CMS-P86 in nitrogen atmosphere

The measurement was performed in a flow cell in a flow of nitrogen. It was repeated at different relative pressures of gaseous toluene. The adsorption affinity of the thin film can be also observed when the interference color changes due to the pore filling. The relative pressure of toluene was controlled between 0 and 0.943 ($p\,p_0^{-1}$). Plotting the refractive index of the thin film versus the relative pressure of toluene resulted in the isotherm shown in Fig. 52.
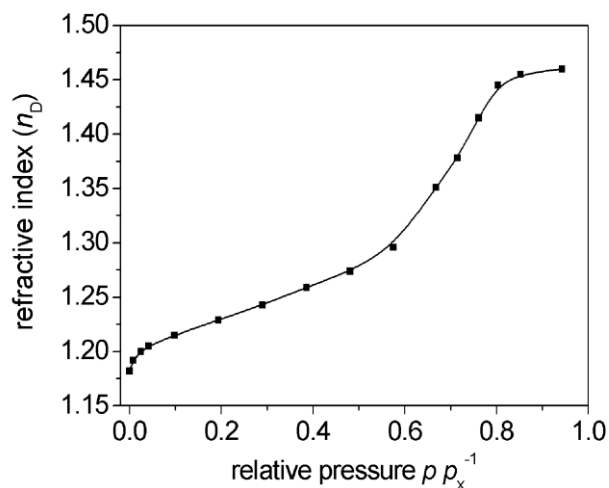
Fig. 52: Ellipsometry data of a thin film of CMS-P86 in toluene vapor in a nitrogen atmosphere

After the templated mesopores are filled, a second step due to the filling of the interparticle porosity can be identified at a relative pressure of 0.6 - 0.8. The ellipsometric data are in very good accordance with powder nitrogen sorption data (Fig. 53). The overlay shows the same sorption behavior for the two different adsorbates.
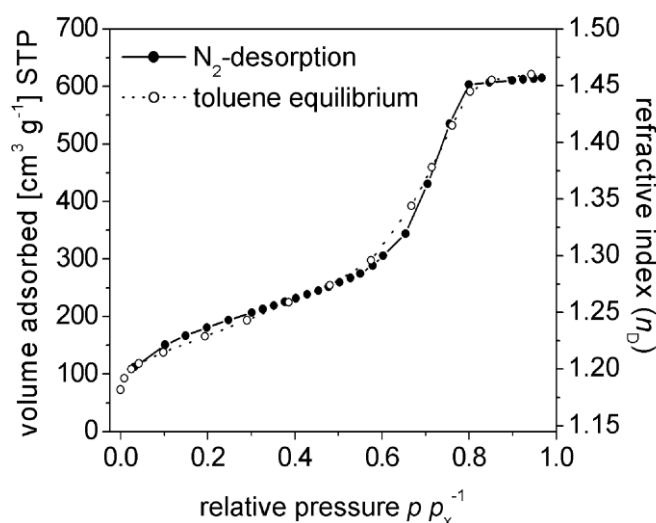
Fig. 53: Overlay of a powder N_2 sorption isotherm (desorption) and a toluene isotherm (equilibrium) of a thin film recorded with ellipsometry (CMS-P86)

With the Lorentz-Lorenz equation for ellipsometric porosimetry (EP), a porosity of 53 % can be specified. Knowing the area of the substrate - a 3 inch wafer - the volume of the deposited film can be easily calculated assuming a cylinder with a height of 650 nm. Based on the high precision of thickness measurements in ellipsometry, the calculated volume of 0.0030 cm^3 can be considered as accurate. If the total pore volume of 0.95 cm^3 g^{-1} in N_2 sorption is correlated to the 53 % porosity in ellipsometric data, a density of 0.56 g cm^{-3} can be calculated. Thus, the expected weight of the film is 1.7 mg. Weighing before and after the film deposition gave a difference of 2.1 mg. This can only act as a rough indication due to a relatively large measuring inaccuracy of the analytical balance and possible adsorbed water due to air humidity.

Conclusion

In this study we have demonstrated the synthesis of extremely small mesoporous silica nanoparticles via a specific co-condensation process with phenyl groups. The size of the suspended mesoporous silica spheres can be controlled in a wide range. The suspensions with a mean hydrodynamic particle diameter of 40 nm or less were optically transparent. After extraction of the surfactant, dispersion in ethanol led to transparent colloidal suspensions. The existence of very small individual porous particles was confirmed by transmission electron microscopy (TEM) and sorption measurements. The suspensions were used for the preparation of homogeneous porous thin films by spin-coating. The films showed excellent optical qualities and could thus be characterized with ellipsometry. It was possible to record sorption isotherms of the thin films with ellipsometry and to correlate the data with nitrogen sorption data of dried powders of the same material. In the future, exchange of the template is anticipated to allow control over the pore size, and the particles can be functionalized or labeled with a fluorescent dye. Examples for a successful functionalization are listed in the supporting information.

Supporting Information

The versatility of the modified synthesis procedure described in Chapter 4.3 can be illustrated by the production of several other functional nanoparticles. If the particle size in the resulting colloidal suspension is around 100 nm, extraction and redispersion can be performed as described in Chapter 4.2. The synthesis conditions were thus adjusted for the following samples.

Experimental Part

CMS-AP

0.22 g aminopropyltriethoxylsilane (APTES, 1 mmol), 0.24 g phenyltriethoxysilane (PTES, 1 mmol) and 2.08 g tetraethylorthosilicate (TEOS, 10 mmol) were combined. 9.0 g triethanolamine (TEAH) and 100 g of an aqueous solution containing 2.5 wt % hexadecyltrimethylammonium chloride (CTAC) were heated to 70 °C. The precursor solution was added and the mixture was stirred for 2 h at 70 °C.

CMS-FITC

3.90 mg fluorescein isothiocyanate (FITC, 0.01 mmol), 0.11 g aminopropyl-triethoxysilane (APTES, 0.5 mmol) and 2.0 g abs. ethanol were stirred 24 h under dry nitrogen atmosphere. The resulting fluorescent orange solution was combined with a mixture of 2.08 g tetraethylorthosilicate (TEOS, 10 mmol) and 0.24 g phenyltriethoxy-silane (PTES, 1 mmol). 9.0 g triethanolamine (TEAH) and 100 g of an aqueous solution

containing 2.5 wt % hexadecyltrimethylammonium chloride (CTAC) were heated to 70 °C. The precursor solution was added and the mixture was stirred for 2 h at 70 °C.

Extraction

Extraction of template was performed by adding an equal amount of ethanol to the translucent, colloidal aqueous suspension of the mesoporous material. The resulting precipitate was centrifuged for 10 min at 40000 g (RCF). After decanting, the sediment was redispersed through vigorous stirring in the initial volume (ca. 100 ml) of an ethanolic solution of ammonium nitrate (20 g l^{-1}) and then refluxed for 1 h. This procedure was repeated with the same amount of a solution of concentrated hydrochloric acid in ethanol (5 g l^{-1}). After washing with pure ethanol, the transparent gelatinous cake obtained after centrifugation was suspended in ethanol.

Results and Discussion

a) Introduction of Aminopropyl Groups through Co-condensation

The new method additionally allows the introduction of aminopropyl groups during the co-condensation. The presence of aminogroups in the silica precursor during the synthesis is usually accompanied with gelation problems. Hence, the synthesis of nanoparticle suspensions with aminopropyl moieties is mainly realized by grafting.[121] In combination with the steric demanding phenyl groups of the phenyltriethoxysilane (PTES), it is possible to obtain dispersed discrete nanoscaled particles. The particle size

distribution in DLS (Fig. 54) shows a slightly broadened signal, probably due to partly interconnected particles.
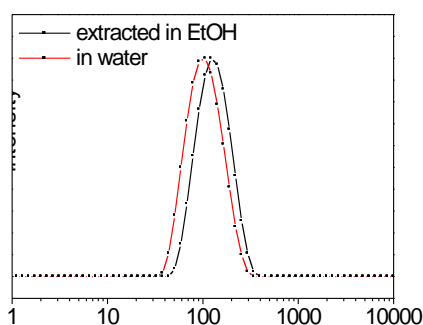

Fig. 54: Particle size distribution (DLS) of CMS-AP before and after extraction

The functional mesoporous organosilica particles show a similar mean diameter around 100 nm before and after template extraction. The coexistence of the two different functionalities can be demonstrated with various methods. In this case, TGA data is difficult to interpret, because the weight loss caused by the decomposition of the aminopropyl groups and the template are overlapping. Fig. 55 shows two distinct steps, with the one at higher temperatures unequivocally deriving from the decay of the aromatic phenyl groups, whereas the first step can presumably be assigned to the aminopropyl groups. Decomposing of the template starts already at lower temperatures around 150 °C (compare Fig. 35, Chapter 4.2).
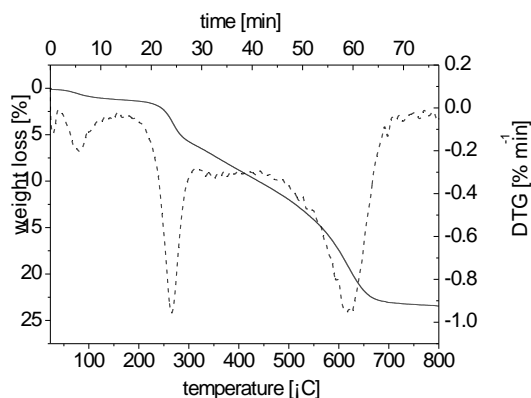
Fig. 55: Thermogravimetric data of extracted CMS-AP

Spectroscopic methods such as NMR or Raman measurements are usually more reliable methods for the characterization of functionalized silica materials. However, solid state ^{29}Si-NMR can also just give an indication for the incorporation of the aliphatic group. Compared to the spectra of the single phenyl modified product, a shoulder at lower field occurs in sample CMS-AP.[122]
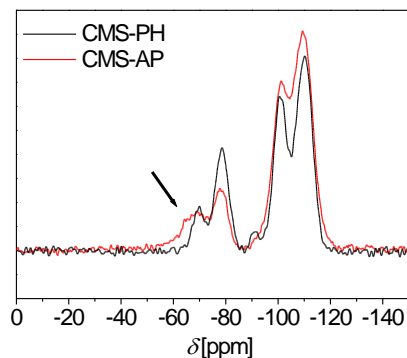
Fig. 56: ^{29}Si-NMR spectra of CMS-AP and CMS-PH

Even though it is difficult to detect the aliphatic aminogroups in Raman measurements, Fig. 57 shows the appearance of an additional signal at 1050 cm^{-1} as a result of C-N stretching in primary amines.
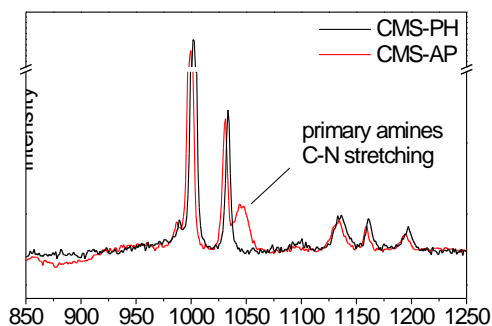

Fig. 57: Raman spectra of CMS-PH and CMS-AP

The isotherm obtained by nitrogen sorption analysis (Fig. 58a) shows the typical pronounced hysteresis at high pressures due to interparticle condensation in nanopowders. The step for the condensation in the templated mesopores is smeared out,

inferring a relatively broad pore size distribution due to the existence of functional groups inside the pore system. Fig. 58b shows the bimodal pore size distribution which is characteristic for mesoporous particles in the scale of about 100 nm.
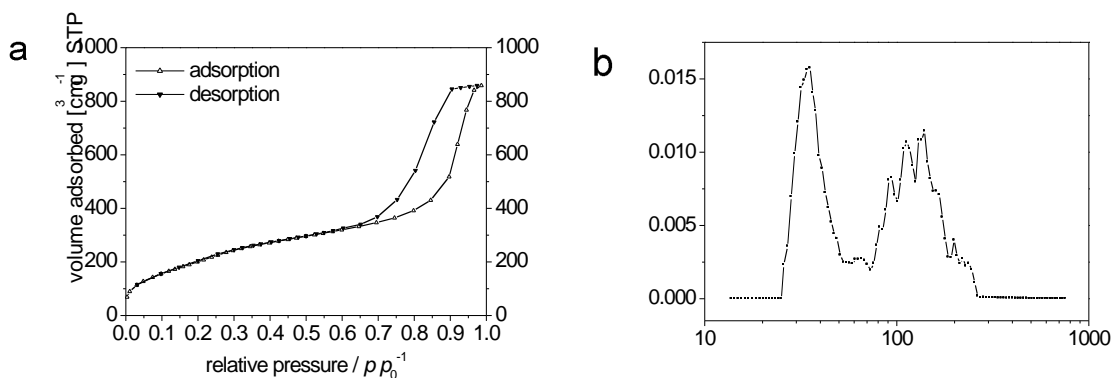

Fig. 58: N_2 sorption isotherm and pore size distribution (DFT) of CMS-AP

c) Labeling with Fluorescein Marker

A porous silica nanoparticle is a suitable host for fluorescent markers due to its chemical and mechanical stability.[108] The encapsulated dye molecule is shielded from external influences and can be further functionalized with biocompatible elements. The labeling with a fluorescein isothiocyanate (FITC) is a common method in biochemistry. The method was also adopted to silica particles[123] and recently to mesoporous silica structures[43] and even mesoporous silica nanoparticles.[47]

The availability of a synthesis recipe for colloidal suspensions with incorporated aminogroups establishes a basis for the successful linking of a marker during a one-step synthesis.[124] After the synthesis of a suitable precursor that already carries the

fluorescence marker, it can be incorporated into the above mentioned synthesis procedure to form labeled colloidal silica particles. The successful incorporation of the dye can be easily verified by adding only fluorescein to a reference sample. Both suspensions are transparent and the exhibit the characteristic color (Fig. 59).
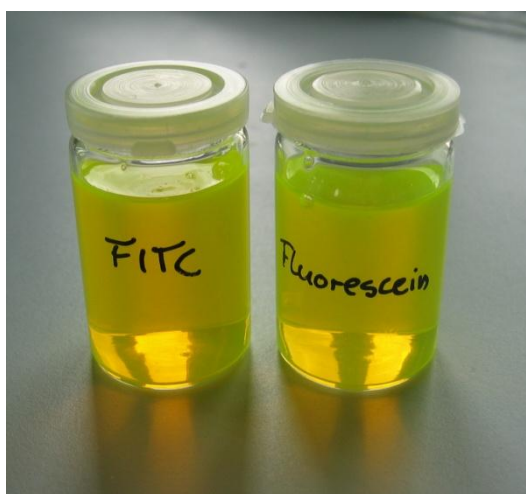

Fig. 59: CMS-FITC and reference sample with fluorescein

After flocculation and separation of the particles by centrifugation, the successful incorporation of the FITC modified precursor can be verified when the solution above the sediment is analyzed. Only in the case of a successful functionalization, it appears colorless or only pale colored from some FITC residues, respectively (Fig. 60).
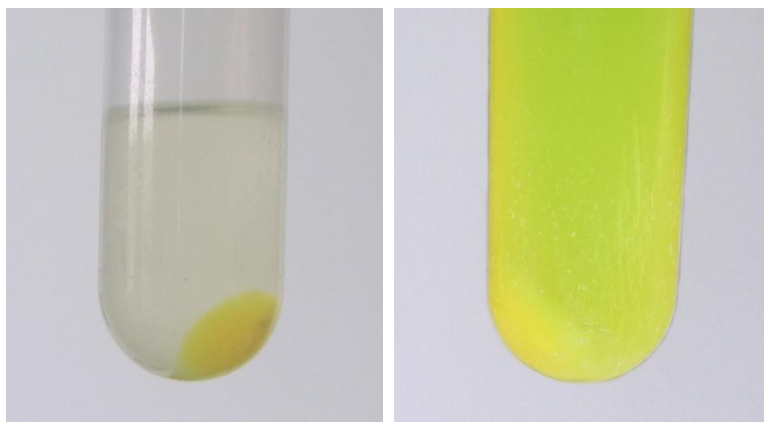
Fig. 60: CMS-FITC and reference sample after centrifugation

The precipitation can be extracted and redispersed in ethanol, resulting in translucent and fluorescent colloidal suspensions of mesoporous silica nanoparticles (Fig. 61)
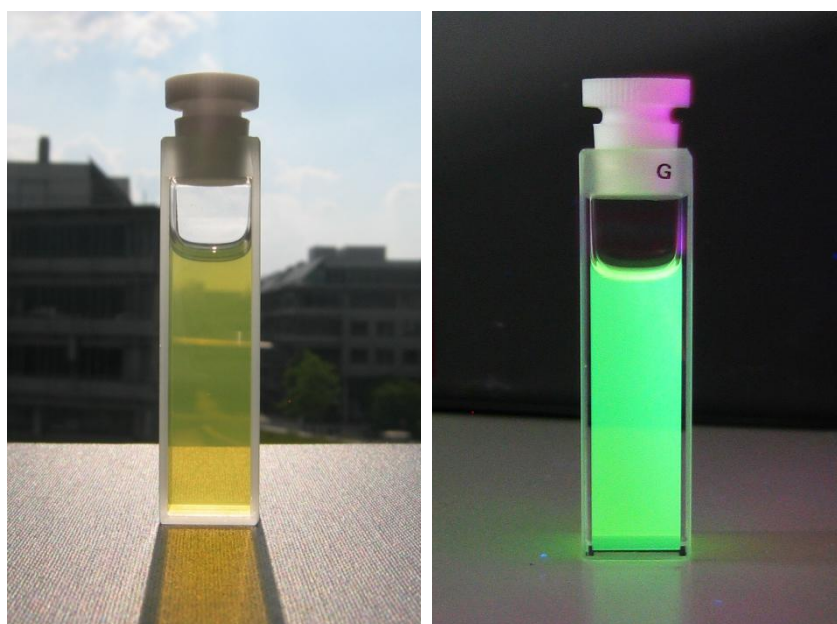

Fig. 61: CMS-FITC after extraction and under UV-irradiation

DLS data confirmed the existence of discrete particles with a comparable particle size distribution. The mean diameter of the particles in the stable colloidal suspension before and after extraction is around 100 nm
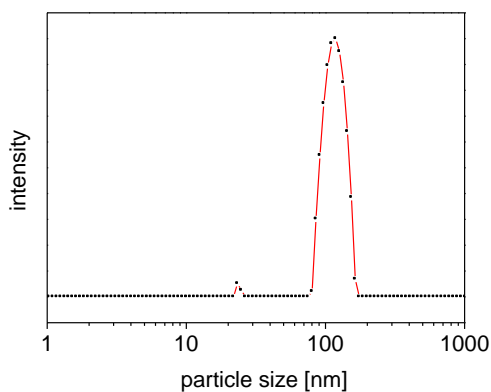

Fig. 62: Particle size distribution (DLS) of extracted CMS-FITC

Due to the very small amount of FITC in the synthesis, further characterization methods give no distinct discrepancy to the sample CMS-AP. TGA as well as nitrogen sorption or Raman investigations are very similar.
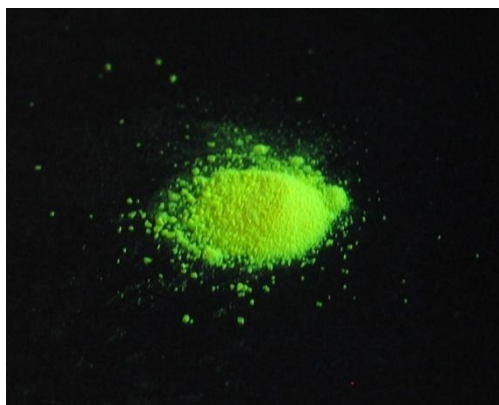
Fig. 63: Dry sample CMS-FITC under UV-irradiation

The dried sample also exhibits the characteristic fluorescence (Fig. 63). In order to investigate the porosity of the sample and the accessibility of the functional group, a simple gas phase reaction can be applied. The yellow powder is brominates with elemental gaseous bromine at normal atmospheric moisture resulting in a red-colored product carrying now eosin moieties (Fig. 64).
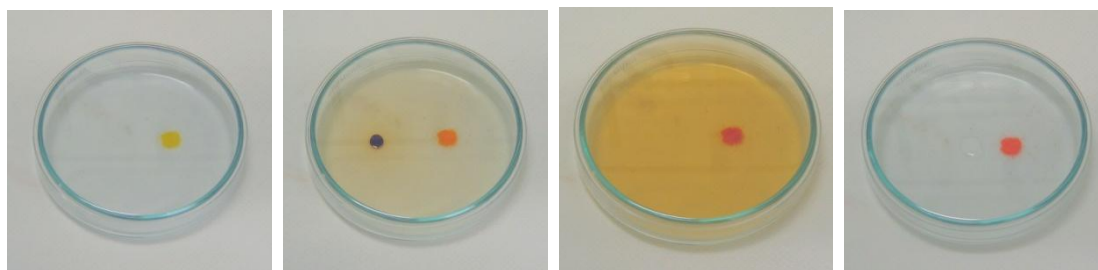

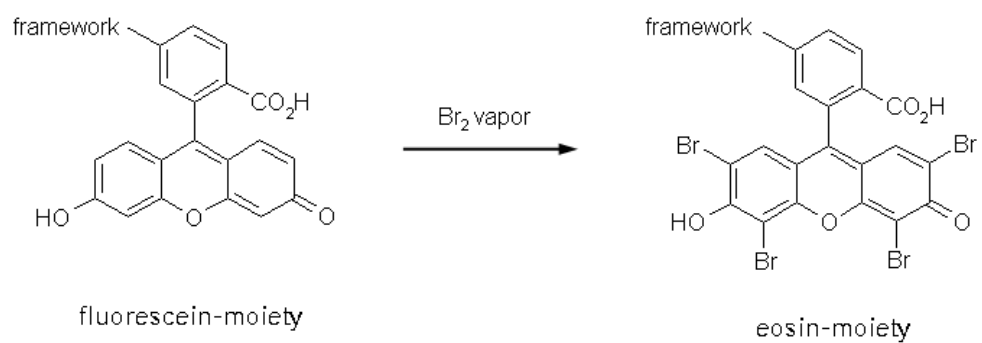Fig. 64: Gas phase reaction of CMS-FITC with bromine vapor

Fig. 65: Bromination of fluorescein moieties with gaseous bromine

4.4 Vapor-Sensitive Bragg Mirrors and Optical Isotherms from Mesoporous Nanoparticle Suspensions

Introduction

Bragg reflectors are multilayer structures composed of alternating layers of two dielectric materials with different refractive indices (n). The optical properties of a Bragg mirror are dependent on the thickness and refractive index of the individual layers. For ideal reflectors, all layers exhibit an optical thickness of $\lambda/4$. The efficiency increases with the number of layer pairs and the contrast of the refractive indices of the low and high refracting materials. For the preparation of good Bragg mirrors, the individual films have to be homogeneous with smooth surfaces and reproducible thickness. Thus, they were often produced by vapor deposition techniques. But it is also possible to assemble Bragg stacks using spin- or dip-coating.

Bragg reflectors are also widespread in nature, e.g., in butterfly wings or iridescent elytra of beetles, where chitin layers are alternated with different refractive index layers in order to control the apparent color in a wide variety of animals.[38] In the laboratory, these special thin films can be prepared, for example, by alternation of low refractive SiO_2 with high refractive TiO_2 films. Regarding porous thin films, the expected change of the interference color upon adsorption or desorption of a volatile species suggests a novel concept for chemical sensing. Indeed, this sensing effect of porous films has already been studied in several publications,[39-43] also in combination with the Bragg stacks.[44]

The preparation of sensing Bragg mirrors faces several challenges. In order to realize high quality Bragg mirrors, the individual layers have to be very homogeneous. Defects or a high surface roughness in the films would propagate and amplify with each

additional layer. For a high brilliance of the Bragg stack, the thickness of the layer has to be constant across the substrate surface. If the stack is to be built from nanoparticle layers, there will be boundary conditions on the optimal size distribution of the individual particles, i.e., the smaller the nanoparticles are, the smoother the film. Porous thin films by their nature have a relatively low refractive index, but for intensive colors, the contrast needs to be high. For sensing applications, one needs two porous layers to guarantee good pore accessibility normal to the surface of the film. Porous SiO_2 is a material with a very low refractive index. In Chapter 4.2, synthesis procedures for the preparation of colloidal suspensions of functionalized mesoporous silica nanoparticles with a very small particle size were discussed. These colloidal suspensions are ideal candidates for the production of highly porous homogeneous thin films with a low refractive index. For the high refractive index layer, nanoparticulate colloidal titania is a suitable material. The preparation of thin films with porous nanoparticles can have some advantages over the common EISA approach for mesoporous films and the growth of zeolite films on substrates, respectively: a) It is anticipated that the porous thin films made of randomly oriented (porous) nanoparticles exhibit improved diffusion properties and a highly accessible pore system.[50] b) It is possible to prepare stable suspensions of already extracted and characterized nanoparticles, thus assuring good reproducibility and well-characterized sorption properties. c) The film thickness can be controlled over a wide range by varying the particle concentration or the number of coating steps. d) The coating of sensitive substrates is facilitated due to the mild processing conditions. For example, intricate or high-temperature template removal procedures between the

coating steps are not required. e) The last-coated layers are located only on top of the layer structure – no soluble precursor constituents may percolate into the already deposited underlying layer structure. Such Bragg mirrors have numerous potential applications, in sensing devices, wavelength-selective tunable optical filters in a broad spectral range, and reflective coatings.

Experimental

The colloidal suspensions of low refractive index material (CMS-P86, porous SiO_2 nanoparticles – see Chapter 4.3) and high refractive index material (CMT-6, TiO_2 nanoparticles – see Chapter 6.2) were used for the preparation of thin films. The homogeneous colloidal suspensions contained between 2 and 5 wt % solid nanoparticulate material. In order to remove potential inhomogeneities, the coating suspensions were filtered through 0.2 μm syringe filters prior to deposition. The thin films were deposited on polished silicon wafers or glass plates by spin-coating using a Laurell WS-400B-6NPP-Lite-AS. All substrates were pre-cleaned with ethanol for 5 s under spinning at 3000 rpm. The film thickness was adjusted by diluting the colloidal suspensions with absolute ethanol, by variation of the spinning rate between 3000 and 5000 rpm, or by multi step coatings, respectively. After each deposition, the film was annealed for 10 s. in a flow of hot air (heat gun, ~ 300 °C) and cooled to room temperature before measurements were performed and the next layer was added. SEM micrographs were recorded with a JEOL JSM-6500F scanning electron microscope (SEM) equipped with an Oxford EDX analysis system. Ellipsometry measurements

were performed with a Woollam M2000D at an angle of 75 ° in the spectral range of 190 – 1000 nm. The data was fitted in the range between 350 – 1000 nm using the Cauchy material as model layer. Transmittance and reflectance measurements were recorded with the same ellipsometer using *p*-polarized light at 45 °, 75 ° or 90 °, depending on the sample and the experimental setup. In order to record the shift of the transmitted (angle: 90 °) wavelength due to vapor sorption, the films were placed into quartz cuvettes with gas in- and outlet. The recording of isotherms (at 22 °C) was performed using a homemade Labview-controlled gas mixer. Digital mass flow controllers (W-101A-110-P, F-201C, Bronkhorst High-Tech) ensured the accurate dosing of the carrier gas nitrogen and the liquid analyte, which was vaporized in a controlled evaporation and mixing element (W-101A, Bronkhorst High-Tech). Partial pressures (*p*) were calculated using the van der Waals equation. The relative pressure $p\,p_0^{-1}$ relates to the saturation pressure p_0.

Results and Discussion

The colloidal suspensions of CMS-P86 and CMT-6 were used for the stepwise deposition of multilayer thin films on silicon wafers in order to examine the thickness, optical properties and homogeneity of the resulting stacks (sample BS-1). After each coating step, the sample was analyzed with ellipsometry. Once the data was fitted, these layers were not changed in the following data acquisition. After the last layer was deposited, the unrestricted fitting of all previous layers did only slightly improve the quality of the fit. This indicates, that the previous films are not changing significantly

upon heating and further deposition. The final homogeneous film (BS-1) appeared golden. Fig. 66 shows the ellipsometric data for a multilayer stack of 4 thin films consisting of functionalized mesoporous silica nanoparticles. The layers are intercalated with mesoporous thin films of titania nanoparticles.
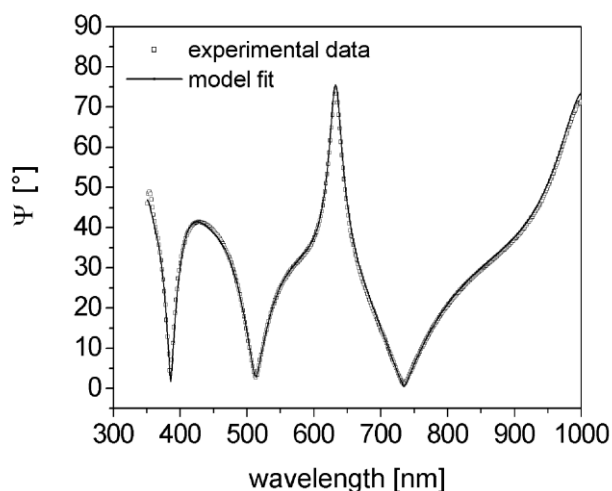

Fig. 66: Experimental ellipsometry data and model fit for a multilayer thin film (BS-1) at 75 ° in nitrogen atmosphere

The data for the theoretical model stack exactly fits the experimental data. The thickness of the individual layers is reproducible and varies only in a narrow range (e.g. 135 nm +/- 8 nm in the case of CMS-P86). This ensures a narrow bandwidth in reflection and transmission, respectively. Table 6 shows the composition of the multilayer stack:

Table 6: Layer thicknesses of the sample BS-1 determined with ellipsometry

number of layer	layer describtion	thickness
8	Cauchy 1	127 nm
7	Cauchy 2	74 nm
6	Cauchy 1	129 nm
5	Cauchy 2	76 nm
4	Cauchy 1	135 nm
3	Cauchy 2	73 nm
2	Cauchy 1	143 nm
1	silicon dioxide	2 nm
0	silicon	1 mm

In the model stack shown above, the functionalized porous silica as well as the porous titania layers are fitted using a Cauchy dispersion model for dielectric materials. Cauchy 1 represents the silica material, and Cauchy 2 stands for the titania layer. Due to inherent porosity of both materials, the fitted refractive indices are significantly lower than for the bulk materials ($n_D = 1.27$ and 1.72 compared to 1.46 for glass and 2.49 for anatase). The Bragg stack structure derived from the ellipsometric data was confirmed with scanning electron microscopy. Fig. 67 shows side-view micrographs of the Bragg stack BS-1. The dark layer represents the SiO_2 layers, which are intercalated by light TiO_2 layers. Thus, the depth profile obtained with ellipsometry is in good accordance with the SEM investigations.
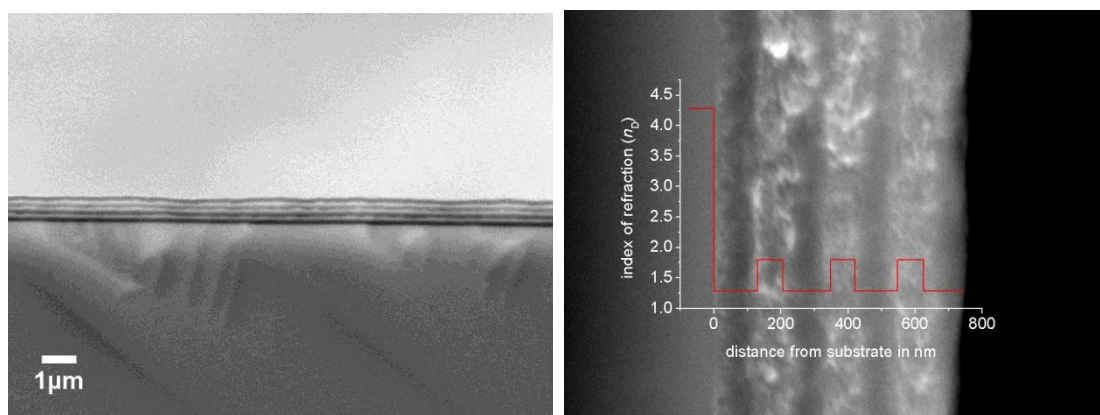
Fig. 67: SEM pictures (side view) and a depth profile (ellipsometry) of the multilayer stack BS-1

When exposed to an atmosphere of toluene close to saturation ($p\,p_0^{-1} = 0.86$), the color of the Bragg mirror immediately changes from yellow to red, because the optical thickness of the individual layers increases due to adsorption of toluene into the pores. This change of the optical properties can be also observed in the reflectance spectra of BS-1 at an angle of 75° in a flow of dry nitrogen (solid line) and of toluene-enriched nitrogen (dotted line) in Fig. 68.
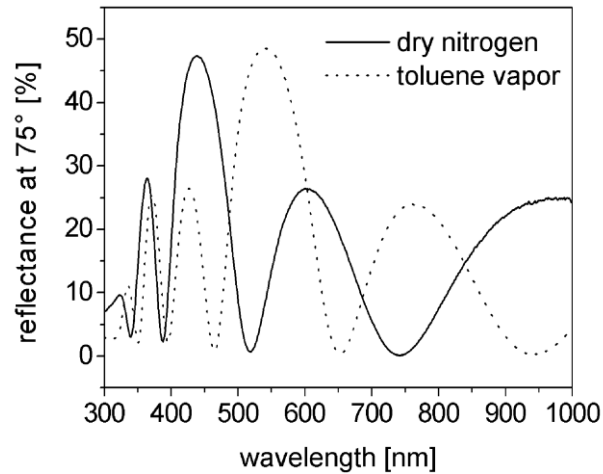
Fig. 68: Reflectance spectra (75 °) of BS-1 in dry nitrogen (solid line) and in toluene-containing nitrogen ($p\,p_0^{-1} = 0.86$, dashed line)

Spectroscopic ellipsometry allows correlating the pore filling to the increase of the refractive index of the individual layers. Fig. 69 shows the pronounced change due to sorption of toluene. The exchange of the gaseous nitrogen by liquid toluene inside the porous multilayer stack significantly influences the refractive index of the individual films.
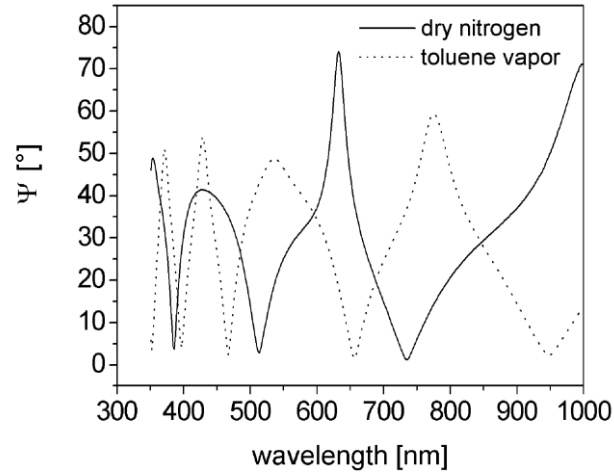
Fig. 69: Experimental ellipsometry data of BS-1 in nitrogen (solid line) and toluene atmosphere ($p\, p_0^{-1} = 0.86$, dashed line)

Fitting of the new experimental data is achieved by simply increasing the refractive index of the layers at constant film thickness. Thus, the n_D values for the silica layer increases from 1.27 to 1.48, and the one of the titania layer from 1.72 to 1.93. Fig. 70 shows the experimental data and the model fit of BS-1 in gaseous toluene with modified optical properties. The good correlation confirms the theory of filled pores:
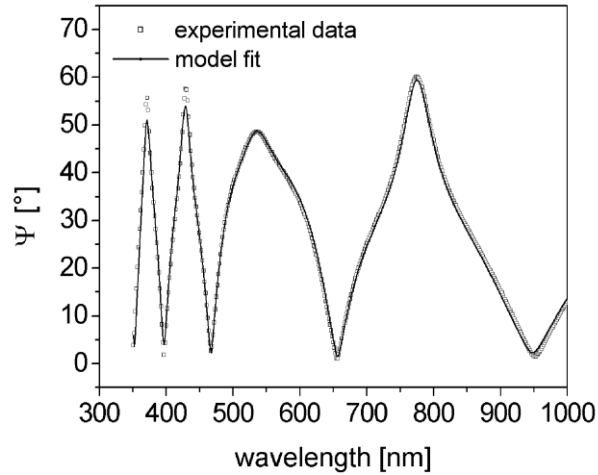
Fig. 70: Experimental ellipsometry data and model fit for sample BS-1 in toluene atmosphere ($p\,p_0^{-1} = 0.86$, dashed line)

The total porosity is calculated with ellipsometric porosimetry using the Lorentz-Lorenz equation. It is based on the Clausius-Mossotti equation, which describes the relation between the macroscopic measurable relative dielectric constant and the electric polarizability α. The adsorption of a volatile species in the film changes its refractive index. When the refractive index of the filled and empty porous substrate is known, one can determine the porosity of the material without knowing the refractive index of the dense material. The values are listed in Table 7:

Table 7: Porosity of the layers in BS-1 determined with ellipsometric porosimetry

layer describtion	n_D in dry nitrogen	n_D in toluene vapor	n_D toluene	porosity (%)
Cauchy 2 (titania)	1.718	1.925	1.496	27.7
Cauchy 1 (silica)	1.266	1.476	1.496	39.3

Knowing the optical properties of the materials, one can predict the optical properties of Bragg reflectors with different thicknesses for wavelength-selective coatings. The optical thickness (OT) of the layers is adjusted to one fourth of the desired wavelength (OT = λ/4). Depending on the refractive index of the material, the physical thickness of the film is calculated (OT/n). If the Bragg mirror is supposed to reflect the green part of the light (500 - 550 nm), the optical thickness of the layers should be about 130 nm. In order to observe a color change depending mainly on the low refractive and modifiable SiO_2-layer, the titania-layer was chosen thin enough to realize an optical thickness (OT) outside the visible part of the light (OT < 100 nm), even in the filled state (refractive index of the toluene filled layer at 350 nm: 1.93). Table 8 shows the desired and realized optical properties of the prepared individual layers of a green reflecting Bragg Stack (BS-2):

Table 8: Desired and actual layer thicknesses and optical properties of the sample BS-2:

	modified silica	titania
reflected color	green	UV
selected wavelength range	500-550 nm	< 350 nm
optical thickness	~ 130 nm	< 90 nm
refractive index of filled layer (325 nm)	-	1.93
refractive index (525 nm)	1.28	-
theoretical film thickness	~ 100 nm	< 47 nm
realized film thickness	102 nm	40 nm

Therefore, the concentration of the colloidal suspensions and the spinning rate of the spin-coater were adjusted in order to realize the preparation of thin films with the above shown thickness for reflecting green light. Single layers of the films were deposited on silicon wafers in order to examine the thickness, before the preparation of the stack was performed on a glass plate. Fig. 71 shows the color of the transmitted and reflected light of the Bragg stack BS-2. The coated transparent glass plate (perpendicular) is illuminated from the right side with sunlight at an angle about 25 °. The transmitted and reflected light falling onto the table is complementary. Due to the illumination angle, the light is shifted to shorter wavelengths (Bragg's law).
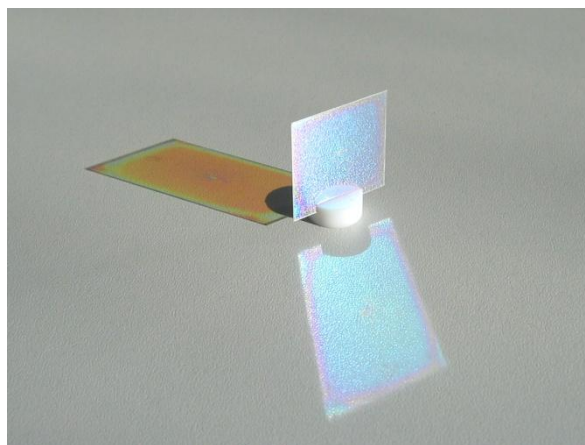
Fig. 71: Sample BS-2 reflecting and transmitting sunlight

The desired theoretical reflected wavelength of the Bragg mirror (maximum ~ 525 nm) was confirmed with transmission measurements. Fig. 72 shows the transmittance spectrum at an angle of 90 ° of sample BS-2. The transmittance minimum is at 520 nm.
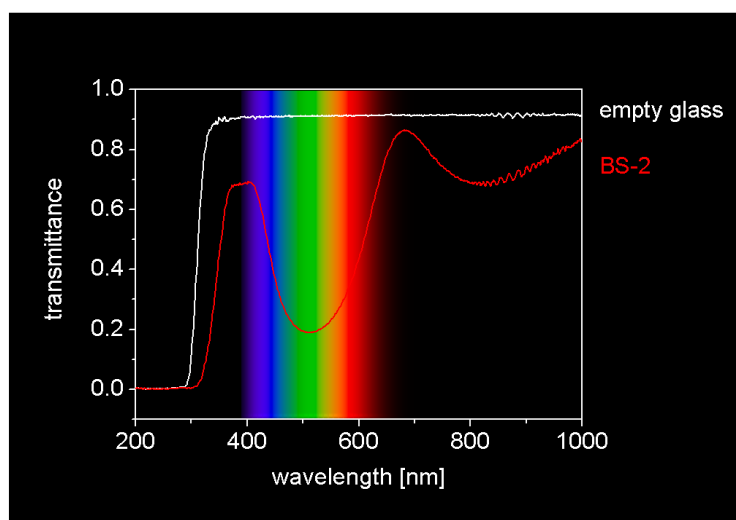

Fig. 72: Transmittance spectrum of BS-2 at an incident angle 90 °

The coated glass cover plate was placed in a quartz cuvette with gas in- and outlet in order to follow the change in the reflectance and transmittance colors of the Bragg reflector after adsorption of gaseous toluene. Fig. 73 shows the sample in dry nitrogen atmosphere (above) and in an atmosphere of toluene ($p\,p_0^{-1} = 0.86$) illuminated with sunlight at an angle of about 45 °.
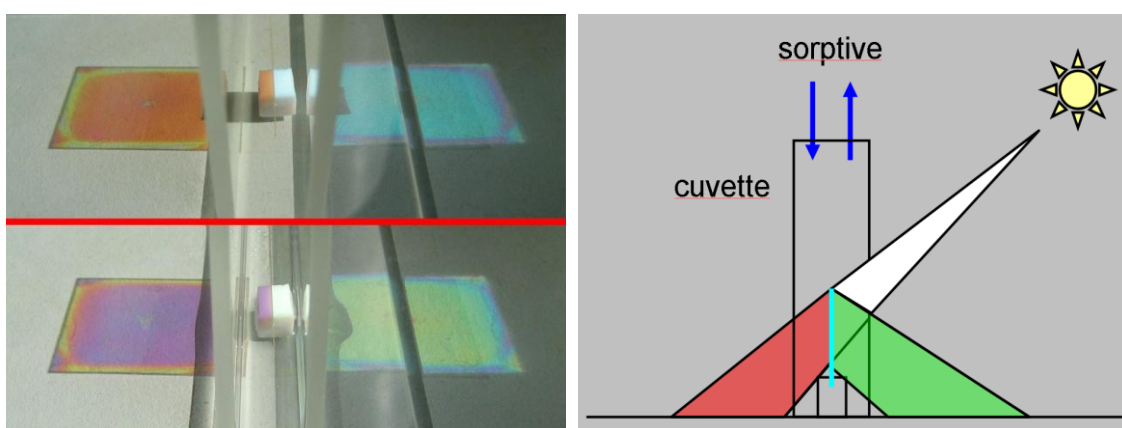

Fig. 73: Wavelength shift due to adsorption of toluene in sample BS-2 (samples in a quartz cuvette illuminated with sunlight at 45 °)

The adsorption of toluene increases the optical thickness of the adsorbing layer and thus drastically changes the reflected as well as the transmitted wavelength. This change can be clearly seen in the transmission spectrum at 45 ° (Fig. 74). The transmission minimum (reflection maximum) changes from about 510 nm (blue) to 590 nm (yellow). This change happens within seconds when the film is exposed to the gaseous adsorbate.
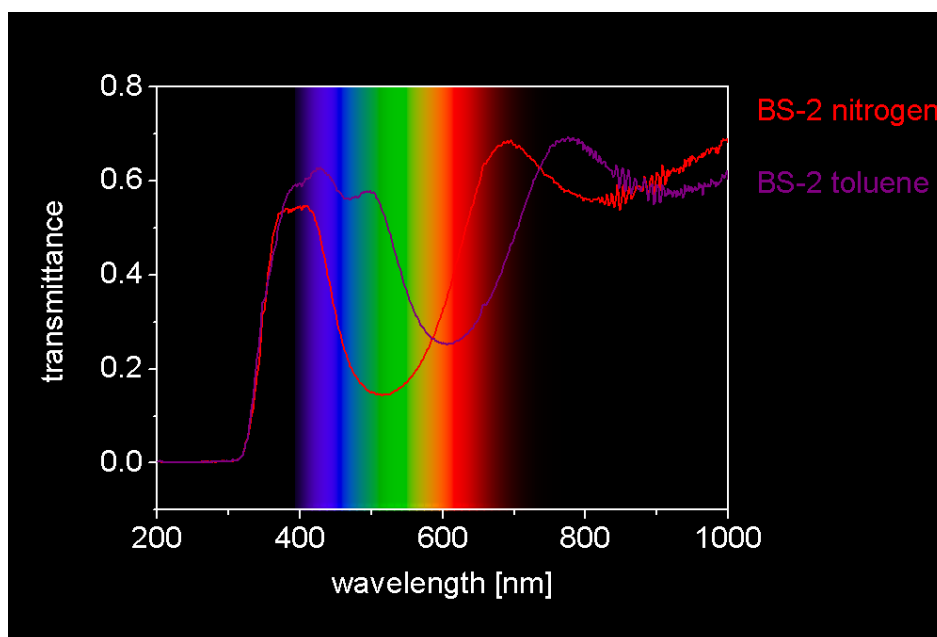
Fig. 74: Wavelength shift of transmitted light at an incident angle of 45 ° due to adsorption of toluene in sample BS-2

Recording the transmission spectrum (90 °) at different partial pressures of toluene resulted in the isotherm shown in Fig. 75. The curve resembles a type IV isotherm, typical for mesoporous materials. After a relatively steep increase, it passes nearly a plateau at a relative pressure of about 0.53 before the slope increases again at about 0.70. The capillary condensation of the mesoporous film occurs at a higher relative pressure.

Fig. 75: Wavelength shift of transmitted light in BS-2 at different relative pressures of toluene (90 ° incident angle)
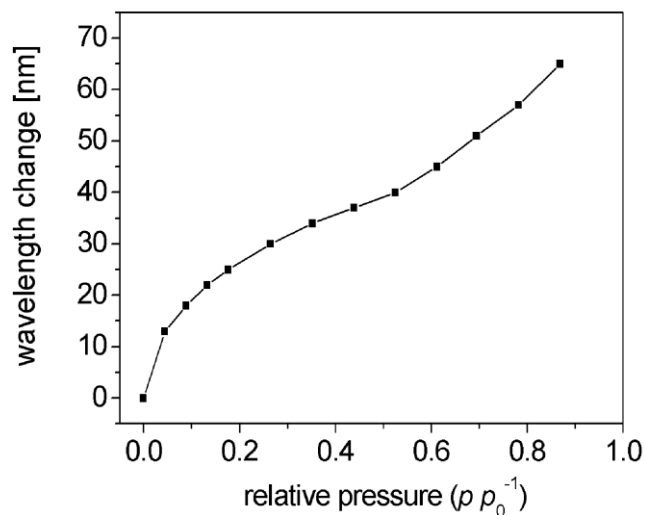
Conclusion

Wavelength specific Bragg mirrors could be produced by a simple and reproducible spin-coating approach. These Bragg reflectors show a sensitivity towards specific relative pressures of organic vapors such as toluene. The existence of various colloidal suspensions of porous nanoparticles opens a wide field of possible functional Bragg mirrors. The functionalization and thus the sorption properties may be varied by introduction of different organic groups offering different interactions with the adsorptives (or analytes) of interest. The sensitive layer can also be replaced by other low-refractive index materials such as zeolites. The thickness of the individual layers can be tuned in order to obtain reflectance or transmittance minima or maxima at a desired wavelength, even in the UV or IR region, or a combination of different wavelengths.

5. CONCLUSION AND OUTLOOK

Colloidal suspensions of various kinds of discrete porous nanoparticles could be synthesized and additionally functionalized with a multitude of organic groups.

Due to the versatile functionalization of porous silica nanoparticles, the materials have a high potential in many applications, e.g., as artificial viruses. The pathway of a fluorescently labeled particle into a cell could be observed with confocal microscopy.

Due to the very small particle size, the colloidal suspensions are completely transparent to the visible part of the light. Thus, the material can be used, e.g., as host material in spectroscopic investigations. Additionally, liquid NMR-studies are possible due to the fast rotation of such small objects in typical solvents. The transparency is also advantageous for the encapsulation of dyes or other materials which may allow one to disperse otherwise insoluble substances in all kinds of matrices. In combination with sensitive caps, the controlled release of drugs or other substances, e.g., of initiators in polymers, constitute interesting topics for further research.

Homogeneous colloidal suspensions of very small nanoparticles are of special interest for the production of thin films by spin-coating on electronic semiconductor devices and for optical coatings. The thin films show very low refractive indices around 1.2 in the case of zeolites and functionalized mesoporous silica nanoparticles, respectively.

The usage of porous nanoparticles has numerous advantages (see introduction in Chapter 4.3). Porous titanium dioxide (thin) films may be interesting for the development of dye-sensitized solar cells. Thorough characterization and optimization of the porosity can help to improve the loading with a dye or the permeation with the electrolyte.

The ability, e.g., of thiol-functionalized mesoporous silica to adsorb high amounts of heavy metal ions could be further investigated in thin films. Their presence should influence the optical properties of the thin films.

Finally, the preparation of chemically sensitive Bragg mirrors using zeolites or other porous metal oxides is also very promising. Due to the usage of nanoparticles, the refractive index of the thin films can be easily adjusted by simply combining colloidal suspensions of different materials. Thus, the color change due to adsorption can be controlled in many respects.

6. APPENDIX

6.1 Functionalized Mesoporous Silica Nanoparticles as Host System for the Synthesis of CdS Quantum Dots

Introduction

Mesoporous materials like MCM-41 can act as molds for the synthesis of structures by inclusion chemistry in otherwise hardly accessible dimensions. Depending on the pore system, the size and shape of the embedded structures can be controlled in a certain range. In the past, many different nanoclusters such as Ge,[125] Fe_2O_3[126] or semiconducting GaAs[127] have been synthesized within the channels. The main interesting features of semiconductor nanocrystals or quantum dots (QD) derive from their atom-like electronic structure. This atom-like electronic structure is a result of the confinement of the electrons in all three spatial directions when very small sizes - typically between 2 and 10 nm - are realized. In contrast to atoms, the energy spectrum of a quantum dot can be engineered by controlling the geometrical size, shape, and the strength of the confinement potential. Quantum dots show unique properties concerning their interaction with light. Their high quantum yield and the possibility to tune the size and thus the spectrum of quantum dots is advantageous for many applications. However, it is sometimes difficult to benefit from these features, because QDs are

difficult to handle. Depending on the desired application, the QDs have to be functionalized with specific shell molecules, for example, for in vivo optical imaging,[128] or they have to be embedded in specific matrix materials when used with high optical efficiency.[129]

A striking example for a possible application of QDs is the utilization in a so called Grätzel or electrochemical solar cell (ECS).[130] Until now, commercially available systems of that new kind of solar cell use TiO_2 crystals in combination with dyes in order to convert photons into excitons (electron-hole pairs) and realize charge separation. Quantum-dot sensitized mesoporous TiO_2, features several advantages compared to the standard electrochemical solar cell, like a better optical tenability and stability.[131] Common II-VI semiconductor nanoclusters include cadmium chalcogenides, e.g., cadmium sulfide or telluride. The emission wavelength depends on the diameter of the dots.[132] The desired size range coincides with the typical pore size of the MCM-41-like mesoporous silica materials. The typical synthesis of semiconductor nanoclusters in the channels of mesoporous materials has been shown following surface modification of the materials.[133] After functionalization, e.g., with thiol groups, a dissolved cadmium salt is absorbed. The resulting sample can be reacted with a chalcogenide source, e.g., H_2S gas, forming nanometer sized quantum dots or wires inside the pores. As discussed before, the functionalized silica materials can also be synthesized as nanoparticles. These colloidal silica particles are of great interest for several optical and biological applications. The combination with a water-based synthesis of cadmium chalcogenide nanocrystals promises large cost advantages

compared to commonly synthesized quantum dots with organic stabilizing agents.[134] Here we describe the attempt to prepare CdS quantum-dots inside the pores of mesoporous silica nanoparticles retaining the colloidal nature of the suspensions.

Experimental

All chemicals were reagent grade (98 % or higher) purchased from Sigma-Aldrich and used without further purification. The water was deionized. The synthesis was carried out in open polypropylene (PP) bottles.

MS-1 host

The synthesis of MS-1 followed a method published by Grün et al:[135] 2.4 g cetyltrimethylammonium bromide (CTAB, 6.6 mmol) were dissolved in 120 ml deionized water in a 250 ml PP-bottle. 9.5 g of ammonia solution (25 %, 140 mmol NH_3), and 10 ml EtOH were added and the solution was stirred for 10 min. After the addition of 10 g tetraethoxysilane (TEOS, 48 mmol) a white precipitate was formed and the suspension was stirred for 1 h. The product was recovered by filtration and washed with water and EtOH.

MS-SH host

Thiol-functionalized mesoporous silica was synthesized similarly in a co-condensation process: 2.4 g cetyltrimethylammonium bromide (CTAB, 6.6 mmol) were dissolved in 120 ml deionized water in a 250 ml PP-bottle. 9.5 g of ammonia solution (25%,

140 mmol NH_3) and 10 ml EtOH were added and the solution was stirred for 10 min. After the addition of a mixture of 8.5 g tetraethylorthosilicate (TEOS, 41 mmol) and 1.63 g mercaptopropyltrimethoxysilane (MPTMS, 8.3 mmol) a white precipitate was formed and the suspension was stirred for 1 h. The product was recovered by filtration and washed with water and EtOH.

Extraction of template from the bulk mesoporous hosts

For extraction of the template, the product was suspended in 250 ml of an ethanolic solution of ammonium nitrate (20 g l^{-1}). The mixture was refluxed under vigorous stirring for 1 h and then filtrated. The procedure was repeated with 250 ml of an ethanolic solution of concentrated hydrochloric acid (5 g l^{-1}). The white filter cake was washed with ethanol and dried at 60 °C.

CMS-SH host

Colloidal mesoporous silica with thiol groups was synthesized following a published procedure.[99] 143 g (960 mmol) triethanolamine (TEAH) and a mixture of 22.3 ml (100 mmol) TEOS plus 3.8 ml MPTMS (20 mmol) were combined in a 500 ml PP-bottle with lid. The two-phase mixture was heated in an oil bath at 90 °C for 20 min without stirring. Immediately after taking the mixture out of the oil bath, 267 g of an aqueous solution (2.5 wt %) of CTAC which had been heated to 60 °C was added and the final mixture was stirred for at least 3 h at 23 °C.

Extraction of template from the colloidal mesoporous host

Extraction of template was performed by adding 250 ml of ethanol to the translucent, colloidal aqueous suspension of the mesoporous material. The resulting precipitate was centrifuged for 10 min at 40.000 g (RCF). After decanting, the sediment was redispersed through vigorous stirring in 250 ml of an ethanolic solution of ammonium nitrate (20 g l^{-1}) and then refluxed for 1 h. This procedure was repeated with a 250 ml of a solution of concentrated hydrochloric acid in ethanol (5 g l^{-1}). After washing with pure ethanol, the transparent gelatinous cake obtained after centrifugation could be redispersed in ethanol, leading to a colloidal suspension of the extracted product.

CMS-SO3H host

The oxidation of the thiol groups in CMS-SH to sulfonic acid was performed with concentrated hydrogen peroxide (33 %) before template extraction. Hydrogen peroxide (120 ml) was added to 2.5 g (calculated dry weight) of the wet sample CMS-SH and stirred for 24 h at room temperature. After oxidation, the sample was washed first in HCl-ethanol and subsequently in pure ethanol (CMS-SO3H-EtOH) or water (CMS-SO3H-water), respectively.

Incubation with Cd (II)

The amount of 10 ml of a 0.1 M solution of $Cd(NO_3)_2$ in ethanol or water, respectively, were added to 2 g of mesoporous silica host (dry weight or calculated dry weight in the case of colloidal suspensions) and stirred for 2 h. The product was recovered by

filtration or centrifugation and washed with ethanol or water ($\rightarrow$ *sample*-Cd-EtOH, s*ample*-Cd-water).

Reaction with hydrogen sulfide

The ethanolic or aqueous suspensions of the corresponding products obtained after the incubation with Cd(II) were treated with gaseous hydrogen sulfide as follows:

FeS was slowly dissolved with 2 M hydrogen chloride and the developing H_2S was bubbled through the suspensions in a flow of nitrogen using the apparatus shown in Fig. 76. Excessive H_2S was eliminated in two washing bottles containing concentrated aqueous NaOH or 2 M aqueous $Cu(NO_3)_2$ ($\rightarrow$ *sample*-CdS).
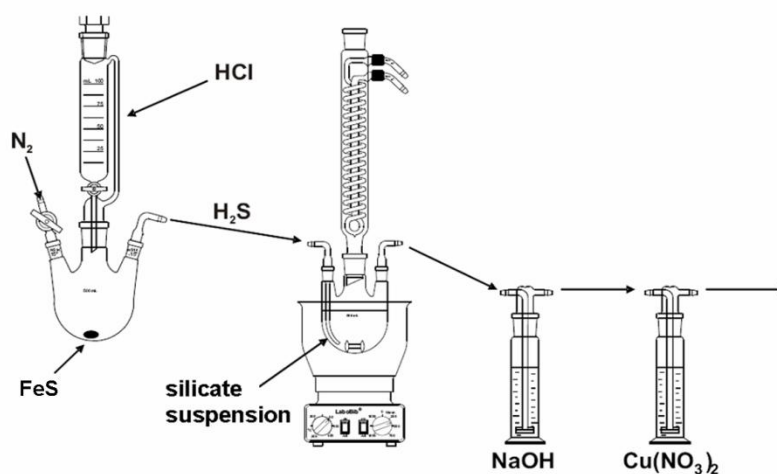

Fig. 76: Setup for the reaction with hydrogen sulfide

Alternatively, dry powder of the Cd(II)-containing mesoporous silica was exposed to dry H_2S atmosphere by connecting a $CaCl_2$-column before the reaction vessel.

Characterization

Dynamic light scattering (DLS) data were collected with an ALV-NIBS/HPPS High Performance Particle Sizer in PMMA cuvettes at 25 °C. Raman spectroscopy was performed with a He-Ne laser (633 nm) on a LabRAM HR UV-Vis (HORIBA Jobin Yvon) Raman Microscope (Olympus BX41) equipped with a Symphony CCD detection system. The spectra were baseline-corrected. For thermogravimetric analysis (TGA) 10 mg of dry powder were heated in corundum crucibles from 30 to 900 °C (10 °C min^{-1}) in a flow of synthetic air (25 ml min^{-1}) using a Netzsch STA 449 C Jupiter thermobalance. X-ray diffraction pattern were recorded on a Scintag Inc. XDS 2000 in theta-theta geometry (Cu-K$_{\alpha 1}$, λ=1.5406 Å; Cu-K$_{\alpha 2}$, λ=1.5444 Å).

Transmission electron microscopy (TEM) was carried out on JEOL JEM 2011 instrument with LaB6 cathode at 200 kV. Samples were prepared on a Plano holey carbon coated copper grid by evaporating one droplet of diluted ethanolic suspension of the extracted material. The nitrogen sorption isotherms (77 K) were obtained using a Quantachrome NOVA 4000e Surface Area & Pore Size Analyzer. Surface area calculations were made using the Brunauer-Emmett-Teller (BET) equation in the range from $p\,p_0^{-1}$ = 0.05 - 0.25. Pore-size distributions were determined using the DFT-method (NLDFT equilibrium model, cylindrical pores, N_2 on oxygen). The pore volume was determined for meso- and micropores at $p\,p_0^{-1}$ < 0.8.

Results and Discussion

Fig. 77 shows the XRD patterns for the prepared bulk samples with (a) and without (b) mercaptopropyl groups. After template extraction the peaks become more pronounced. The typical reflection peak for such mesoporous materials can be observed at about 2 ° (2θ) for the pure siliceous material (MS-1) and 2.3 ° for the functionalized one (MS-SH). In the sample with thiol groups, the reflections are less intense and shifted to higher values. This can be explained with the smaller pore size in combination with a higher degree of disorder in the functionalized materials synthesized via co-condensation.
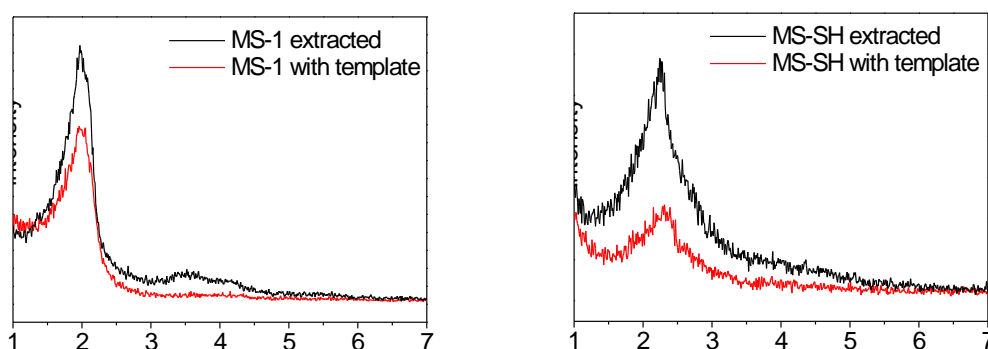

Fig. 77: XRD powder pattern of pure siliceous and functionalized mesoporous bulk material after drying and extracting

These two observations are naturally more pronounced when looking at dry powder of functionalized mesoporous nanoparticles (Fig. 78). Characterization of the colloidal suspensions of mercaptopropyl functionalized nanoparticles is described in Chapter 4.2.
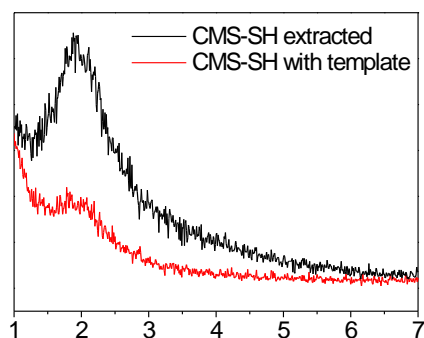
Fig. 78: XRD powder pattern of colloidal functionalized mesoporous silica (CMS-SH) after drying and extraction

Sorption measurements (Fig. 79) confirmed the successful extraction of the template and the availability of highly porous materials.
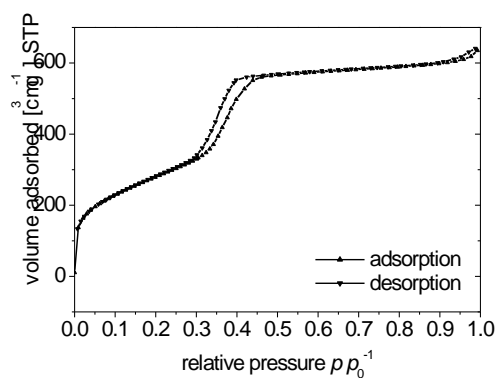

Fig. 79: N_2 sorption isotherm of extracted MS-1

Incubation with Cd(II)

Evaluation of the thermogravimetric analysis data resulted in an estimated weight loss of 190 mg mercaptopropyl residues per gram for MS-SH as well as for CMS-SH. Using the molar weight of 75 g mol^{-1} for these mercaptopropyl-residues, resulted in a calculated concentration of 2.5 mmol thiol per g material (ignoring residual template). The more conclusive elemental analysis showed a sulfur content of 6 % in weight. Using the molar weight of sulfur (32 g mol^{-1}) results in a concentration of 1.87 mmol thiol per g silica. Based on an average value of 2 mmol g^{-1} and the assumption that one Cd^{2+} ion coordinates to two thiolates, the maximum of adsorbed cadmium ions should not exceed 1 mmol per g functionalized silica. The usage of a great excess (5 mmol g^{-1}) in the treatment with Cd(II) should ensure the coordination of every accessible thiol group.

TGA measurements after incubation and washing showed a successful loading with the heavy metal ions. The relative weight loss in percent caused by the decomposition of the organic residues is lower in the material loaded with Cd^{2+} (Fig. 80)
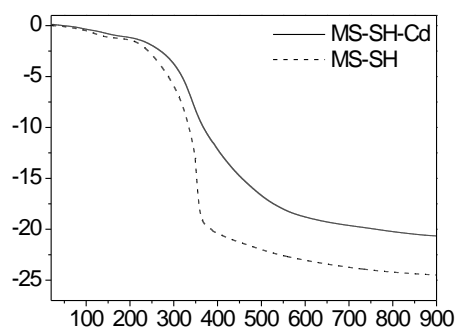
Fig. 80: TGA data of extracted MS-SH before and after loading with Cd(II)

A further indication for a successful coordination to the thiol groups is the decrease of the pH-value, when the cadmium salt is added to the suspensions of extracted MS-SH. The Cd^{2+}-ions replace the protons when coordinating to the SH-groups, resulting in a higher acidity. Fig. 81 shows that the pH-value of the suspension (3.5) decreases significantly to 2.4 after addition of the aqueous cadmium salt solution (pH = 5.6).
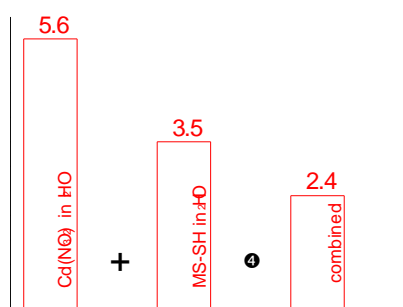

Fig. 81: Increase of the acidity caused by the coordination of Cd^{2+} in MS-SH

Deprotonation of the SH-groups can also be observed in Raman measurements. Fig. 82 shows the spectra before and after insertion of cadmium ions in MCM-SH. The characteristic S-H-stretching at 2580 cm^{-1} lost most of its intensity after the adsorption of cadmium ions.
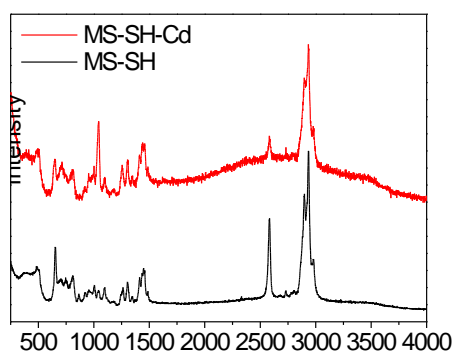
Fig. 82: Raman spectra of MS-SH before and after incubation with Cd^{2+} ions

Oxidation of CMS-SH

After the first adsorption experiments with cadmium salts in colloidal suspensions of thiol-functionalized mesoporous silica, it emerged that the particles tend to agglomerate irreversibly.

The selective oxidation of the external SH-groups into sulfonic acid groups (-SO$_3$H) was believed to solve the aggregation problem. This modification should have been achieved with hydrogen peroxide in combination with template-filled material. The

conversion of thiol groups in mesoporous silica nanoparticles into sulfonic acid with hydrogen peroxide is proven.[99]

Apparently, the strength of the H_2O_2 and the reaction time were sufficient to oxidize all thiol groups − also those inside the pore system. Probably, the organic template is decomposed,[136] while the functional head of the organic residue is only converted into sulfonic acid. The completeness of the thiol oxidation can be observed in Raman spectra. Before the reaction with hydrogen peroxide, the typical signals of the thiol groups appear at 2580 cm^{-1} and 650 cm^{-1}. These peaks completely disappear after the treatment with H_2O_2 and instead a new one occurs at 1050 cm^{-1} (sulfonate stretching). The signals for the aliphatic propyl groups around 2900 cm^{-1} are retained (Fig. 83).
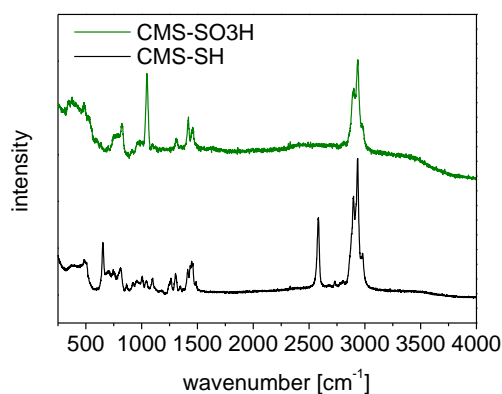

Fig. 83: Raman-spectra before and after oxidation of CMS-SH with hydrogen peroxide.

The coagulation of the particles after Cd(II)-salt addition could be avoided by oxidation of the thiol groups. The suspensions showed the same particle size distribution after incubation with cadmium salts.

In order to further verify the effective coordination of heavy metal ions to the functional groups, equivalent amounts of the cadmium salt are introduced to the aqueous or ethanolic suspensions of:

pure siliceous bulk material (MS-1-Cd)

functionalized bulk material (MS-SH-Cd)

colloidal suspensions of functionalized material (CMS-SH-Cd)

colloidal suspensions of oxidized functionalized material (CMS-SO3H-Cd)

After washing the material, the cadmium content was investigated with elemental analysis. As seen in Fig. 84, the amount of incorporated cadmium found in the thiol functionalized materials is significantly higher compared to the pure silica. The amount additionally depends on the solvent. The remaining amount is higher when the loading and washing is performed with ethanol. Colloidal suspensions and suspension containing bulk material adsorb comparable amounts. Interestingly, the suspension containing the nanoparticles with sulfonic acid groups also adsorbs a considerable amount of heavy metal ions - and the colloidal particles do not coagulate.
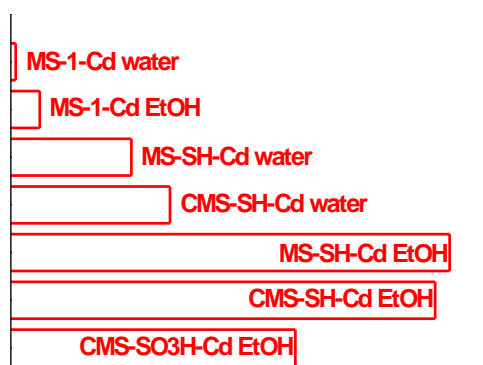
Fig. 84: Amount of Cd^{2+} in the different suspensions found with elemental analysis

Reaction with hydrogen sulfide

After the successful loading of the cadmium ions into the mesoporous hosts, the materials were exposed to gaseous hydrogen sulfide. The aqueous as well as the ethanolic suspensions immediately turned yellow upon bubbling with H_2S. Only if the CdS is present as bulk material - or at least not as quantum dots - it shows its characteristic bright yellow color. The expected nanoparticles inside the pore system should be colorless and fluorescent under UV-irradiation. Fig. 85 shows an image of CMS-SO3H-CdS with the typical yellow color of bulk cadmium sulfide. The colloidal nature of the suspension with an average particle diameter of 170 nm is preserved.
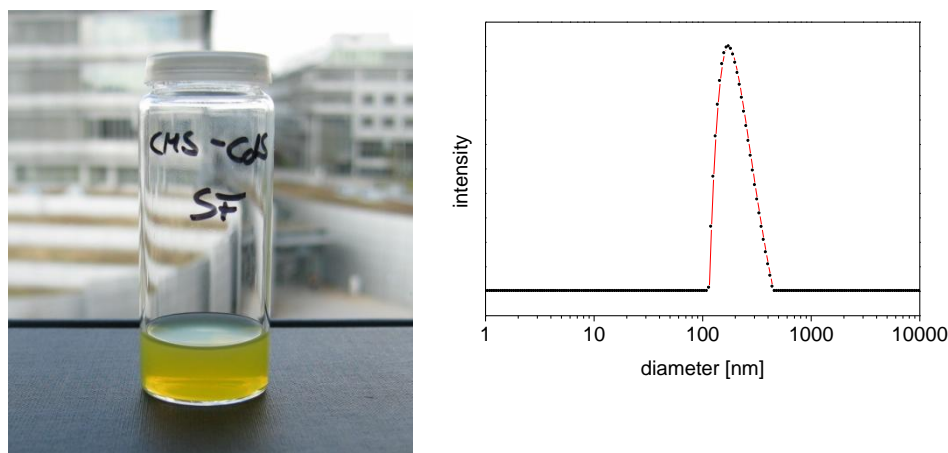
Fig. 85: Image and DLS data of CMS-SO3H-CdS in ethanol after loading with Cd^{2+} and reaction with H_2S

Probably, the initially formed CdS-clusters are very mobile in water or ethanol and tend to leave the pore system in order to create larger particles on the surface of the mesoporous hosts or in solution. Even the supposedly dry powder (MS-SH-Cd) in H_2S atmosphere showed this yellow color after a few seconds. Presumably, the moisture present with the development of hydrogen sulfide is problematic because it enhances the mobility of the sulfide species involved.. Therefore, the H_2S was dried in a $CaCl_2$-column before it was reacted with the completely dry material (MS-SH-Cd). No change in color could be observed under these conditions. However, after addition of water the white powder instantly turned yellow (Fig. 86). This observation supports the proposed high mobility of initially formed CdS species.
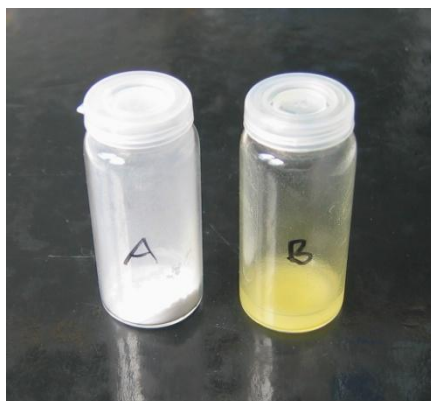
Fig. 86: MS-SH-Cd after exposure to dry H$_2$S (A) and after addition of water (B)

Powder X-ray diffraction

Fig. 87 shows the XRD pattern of CMS-SO3H-CdS in combination with the expected diffraction pattern of bulk CdS material. The peaks are significantly broadened, indicating the existence of small crystallites.
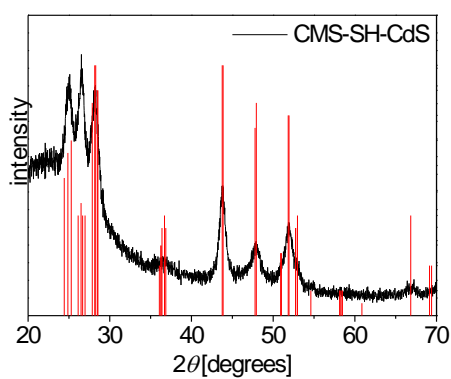

Fig. 87: Powder diffraction pattern of CMS-SO3H-CdS

Applying the Scherrer equation allows approximating the average particle size. For this purpose, the full width at half maximum (FWHM) of a peak at a certain angle (2θ) is determined. Here, the instrumental broadening is neglected and the value of 0.94 was chosen for the Scherrer constant K.

$$D = \frac{K \cdot \lambda}{FWHM \cdot \cos\theta}$$

In combination with the wavelength of the Cu-K$_\alpha$ radiation ($\lambda = 0.154$ nm) and a FWHM of 0.014 (radian measure) at $2\theta = 44°$ or $\theta = 22°$, respectively, an average particle diameter D of approximately 11 nm can be calculated. Thus, the particles are much too big to fit into the 3 nm pores.

TEM-micrographs of the same sample show the monodisperse spherical particles with a star-shaped pore system. As expected from XRD measurements, there is no evidence for the existence of CdS particles inside the pores. Instead, a few dense particles in the dimensions of about 10 nm can be found beside the porous silica particles (Fig. 88).
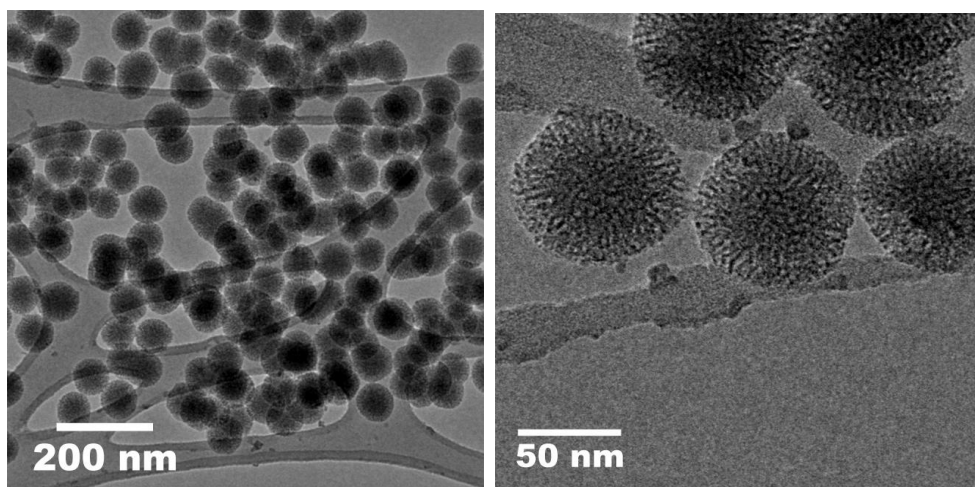
Fig. 88: TEM-micrographs of CMS-SO3H-CdS

As mentioned above, the colloidal suspension had a bright yellow color. Interestingly, this coloration became less intense with time and nearly disappeared after 10 days. The suspension showed a pink fluorescence under UV-irradiation (Fig. 89).

Fig. 89: CMS-SO3H-CdS after 10 days (left) shows fluorescence under UV-light (right)

Presumably, the initially 11 nm-sized CdS particles slowly dissolved and temporarily had the appropriate size to show fluorescence. The undefined pink fluorescence may derive from a rather diversified size distribution of the CdS clusters. Two days later the fluorescence disappeared.

Conclusion

The aim of the project was to use the existent colloidal suspensions of functionalized mesoporous silica nanoparticles as host system for the synthesis of CdS quantum dots. It was possible to load these porous particles with a high amount of heavy metal ions preserving the colloidal state. However, when introducing the hydrogen sulfide, it appears that the initially formed CdS species inside the pores are very mobile, and that they can easily leave the pore system to form larger clusters at the outer surface of the mesoporous particles or in the solvent. They are not stabilized in the confined space as desired. It is imaginable that the synthesis could be successful with other solvents or reagents.

6.2 Colloidal Suspensions of TiO$_2$ Nanoparticles for the Preparation of Porous Thin Films

Introduction

Titania exists in a number of crystalline forms, of which the most important are anatase and rutile. It is inert, does hardly react with other materials, and is thermally stable, non-flammable, and non-toxic. TiO$_2$ is the most widely used white pigment because of its brightness and very high refractive index ($n = 2.4$). As effective opacifier in powder form, it is employed as a pigment to provide whiteness and opacity to products, such as glass and porcelain enamels, cosmetics, sunscreens, paper, paints, and foods.

Titanium dioxide, particularly in the anatase form, is a photocatalyst under ultraviolet light. The strong oxidative potential of the positive holes oxidizes water to create hydroxyl radicals, and the holes can also oxidize organic materials directly. Titanium dioxide is thus added to paints, cements or directly coated as protective thin film onto the desired surface. When deposited as a thin film, its high refractive index makes titania an excellent reflective optical coating for dielectric mirrors. A further important application is the utilization as semiconducting layer in dye-sensitized solar cells (DSSC).[130] In these so-called Grätzel cells, nanoparticulate layers or homogeneous

mesoporous films can potentially offer great improvements. Their high surface areas allow a high loading with dye. For an efficient operation, the titania layer should have a highly accessible pore system. Thus, it is important to obtain the material as discrete nanoparticles in colloidal suspensions. The synthesis of titanium dioxide particles at the nanometer scale can be achieved by several methods, such as pyrolysis or sol-gel chemistry.[137]

In the last years, several studies on the synthesis of mesoporous titania, which should exhibit a higher specific surface area than the nanoparticles, were published. Most of the experiments are based on the synthesis of mesoporous silica, for example, the synthesis procedure described by Amoros[138] which uses a complexing agent in order to retard the hydrolysis of the titaniumalkoxide. Due to fundamental differences in hydrolysis and condensation behavior as well as template interaction, it turned out that the principles used for the synthesis and extraction of mesoporous silica cannot be adopted easily. The main difficulty is the removal of the template either by extraction or calcination. In the latter case, collapsing of the pore system due to the formation of large crystalline domains is one reason.

The preparation of mesoporous titanium dioxide in nanoparticulate form is also frequently claimed.[139, 140] For the preparation of thin films via spin-coating, the existence of discrete mesoporous particles in a homogeneous colloidal suspension is necessary, but the focus of the research is often on other objectives, like a high crystallinity or stability.[140, 141]

The preparation of mesoporous titania in the form of thin films with the EISA approach is well-investigated.[20] This recipe was also adopted for the synthesis of bulk material, by slowly evaporating the solvent.[142, 143] Although the synthesis of homogeneous mesoporous TiO_2 thin films following the EISA-approach is practical, the formation from nanoparticles might be advantageous in some respects. As already mentioned in Chapter 4.3, it is believed that such films might exhibit improved diffusionial access. Additionally one can work with a stable suspension of already extracted and characterized nanoparticles, thus ensuring good reproducibility. The coating of sensitive substrates is facilitated due to the mild conditions and the thickness can be easily controlled by varying the concentration or by multiple step coating. As a further treatment such as extraction or calcination is no longer necessary, sensitive substances, e.g., dyes, can already be added to the coating suspensions. Finding an appropriate titania precursor is the first challenge in titania sol-gel chemistry, as the hydrolysis of the titanium precursors is typically much faster than that of the silica analogues. Common precursors are titanium alkoxides and complexes, e.g., titanium(IV)bis(acetylacetonate)diisopropoxide or titanium(IV)(triethanolaminato) isopropoxide. The aim of this work was the preparation of homogeneous porous thin films from TiO_2 nanoparticles by a facile and reproducible spin-coating approach.

Experimental

CMT-1 / CMT-1A

The amount of 2.44 g hexadecyltrimethylammonium bromide (CTAB, 6.7 mmol) and 6.33 g titanium(IV) (triethanolaminato) isopropoxide (TiTEAiOPr, 80 % in isopropanol, 20 mmol) were combined at room temperature and mixed with 60 ml water under stirring. Precursor and template were completely dissolved and stirred for 24 hours at room temperature. The initially clear solution started to become opalescent after about 2 hours. One half of the final colloidal suspension was centrifuged and the sediment was washed 3 times and then redispersed in water (CMT-1). The other half was autoclaved at 100 °C for 24 hours and then washed and redispersed (CMT-1A). Parts of the material were calcined (CMT-1-c, CMT-1A-c) at 350 °C for 3 h (1 K min^{-1}) or extracted (CMT-1-e, CMT-1A-e) as described in Chapter 4.2.

CMT-2

The experiment above was repeated at 50 °C without autoclaving.

CMT-3

The amount of 2.0 g TiTEAOiPr (80 % in isopropanol, 6.3 mmol) was added to a preheated (60 °C) solution of 0.5 g hexadecyltrimethylammonium chloride and 62.0 g water under stirring. The mixture was kept at 60 °C and stirred for 2 h. The final colloidal suspension was centrifuged and the sediment was washed 3 times and then redispersed in water.

CMT-4

The amount of 2.76 g concentrated hydrochloric acid (37 %) was added to a solution of 5.68 g tetraisopropylorthotitanate and 10 g EtOH. A mixture of 1.16 g hexadecyltrimethyl-ammonium bromide (CTAB) in 8.4 g EtOH and 4.38 g dest. H_2O were added and the clear solution was refluxed under stirring for 6 h, while slowly forming a white suspension. The suspension was diluted with 20 ml EtOH, centrifuged for 30 min at 40000 g (RCF) and redispersed in a mixture of 20 ml EtOH and 2 g dest. H_2O. Centrifugation and redispersion in pure ethanol was repeated twice leading to a colloidal suspension of TiO_2 nanoparticles. For characterization of the material, a part of the suspension was dried at 60 °C.

CMT-5

The amount of 2.76 g concentrated hydrochloric acid (37 %) was added to a solution of 5.68 g tetraisopropylorthotitanate and 18.4 g EtOH. The amount of 4.38 g dest. H_2O was added and the clear solution was refluxed under stirring for 6 h, while slowly forming a white suspension. The suspension was diluted with 20 ml EtOH, centrifuged for 30 min at 40000 g (RCF) and redispersed in a mixture of 20 ml EtOH and 2 g dest. H_2O. Centrifugation and redispersion in pure ethanol was repeated twice leading to a colloidal suspension of TiO_2 nanoparticles. For characterization of the material, a part of the suspension was dried at 60 °C.

CMT-6

The amount of 5.52 g concentrated hydrochloric acid (37 %) was added to a solution of 11.36 g tetraisopropylorthotitanate and 36.8 g EtOH. The amount of 8.76 g dest. H_2O was added and the clear solution was refluxed under stirring for 6 h, while slowly forming a white suspension.

The suspension was diluted with 20 ml EtOH and peptized with 1 ml water before it was centrifuged for 5 min at 40000 g (RCF) in order to remove big agglomerates. The supernatant suspension was flocculated with 20 g hydrochloric acid and after centrifugation the sediment was redispersed in a mixture of 20 ml EtOH and 2 g dest. H_2O. This washing procedure was repeated once.

Thin film preparation

The colloidal suspensions of CMT-6 contained about 3 wt %. titaniumdioxide. The ethanolic suspension can be used directly for the preparation of thin films by spin-coating. The thin films were deposited on polished silicon wafers or QCM chips (XA 1600 AT-cut, KVG Quartz Crystal Technology) by spin-coating using a Laurell WS-400B-6NPP-Lite-AS. All substrates were pre-cleaned with ethanol for 5 s under spinning at 3000 rpm. The film thickness was adjusted by diluting the colloidal suspensions with absolute ethanol, by variation of the spinning rate between 3000 and 5000 rpm, and by multi step coatings.

Characterization

Dynamic light scattering (DLS) data were collected with a Malvern Nano ZS in PMMA cuvettes at 25 °C. Raman spectroscopy was performed with a He-Ne laser (633 nm) on a LabRAM HR UV-Vis (HORIBA Jobin Yvon) Raman Microscope (Olympus BX41) equipped with a Symphony CCD detection system. The spectra were baseline-corrected. For thermogravimetric analysis (TGA) 10 mg of dry powder were heated in corundum crucibles from 30 to 900 °C (10 °C min^{-1}) in a flow of synthetic air (25 ml min^{-1}) using a Netzsch STA 449 C Jupiter thermobalance. X-ray diffraction pattern were recorded on a Scintag Inc. XDS 2000 in theta-theta geometry (Cu-K$_{\alpha 1}$, $\lambda = 1.5406$ Å; Cu-K$_{\alpha 2}$, $\lambda = 1.5444$ Å). Transmission electron microscopy (TEM) was carried out on a JEOL JEM 2011 instrument with LaB$_6$ cathode at 200 kV. Samples were prepared on a Plano holey carbon coated copper grid by evaporating one droplet of diluted ethanolic

suspension of the extracted material. The nitrogen sorption isotherms (77 K) were obtained using a Quantachrome NOVA 4000e Surface Area & Pore Size Analyzer. Surface area calculations were made using the Brunauer-Emmett-Teller (BET) equation in the range from $p\,p_0^{-1}$ = 0.05 - 0.25. Pore-size distributions were determined using the DFT-method (NLDFT equilibrium model, cylindrical pores, N_2 on oxygen). The pore volume was determined for meso- and micropores at $p\,p_0^{-1}$ < 0.8. Ellipsometry measurements were performed with a Woollam M2000D at an angle of 75° in the spectral range of 190 - 1000 nm. The data was fitted in the range between 350 – 1000 nm using the Cauchy material as model layer. Ellipsometric porosimetry measurements were carried out in a liquid cell at different partial pressures at a measurement angle of 75 °. The recording of isotherms was performed using a homemade Labview-controlled gas mixer. Digital mass flow controllers (W-101A-110-P, F-201C, Bronkhorst High-Tech) ensured the accurate dosing of the carrier gas nitrogen and the liquid analyte, which was vaporized in a controlled evaporation and mixing element (W-101A, Bronkhorst High-Tech). Partial pressures were calculated using the van der Waals equation with real gas-state assumptions.

(QCM) A 10 MHz Quartz Crystal Microbalance (QCM) device (XA 1600 AT-cut, KVG Quartz Crystal Technology) was used to measure frequency changes due to additional adsorbed mass. Some parameters of the Sauerbrey equation, such as the density ρ_q = 2.648 g·cm^{-3} and the shear modulus υ_q = 2.947·10^{11} g·cm^{-1}·s^{-2}, are characteristics of the piezoelectric material quartz. The Sauerbrey equation is normalized to 1 cm^2 sensing area on the QCM chip; thus, a frequency change of 1 Hz

corresponds to a mass-loading of $4.42 \cdot 10^{-9}$ g. The overall frequency fluctuation of the system is ± 1-2 Hz at room temperature.

Results and Discussion

The first experiments (not shown) were inspired by the synthesis of mesoporous silica nanoparticles described in Chapter 4.2. The pretreatment of the titaniumalkoxide with triethanolamine at elevated temperature resulted in yellowish clear solutions, which slowly hydrolyzed in water compared to the titaniumalkoxides. In the reactions shown here, the commercially available complexed precursor titanium(IV) (triethanolaminato) isopropoxide was used.

After hydrolysis, the resulting colloidal suspension CMT-1 contained discrete particles with an average hydrodynamic diameter (DLS) of almost 1 µm after washing (Fig. 90).
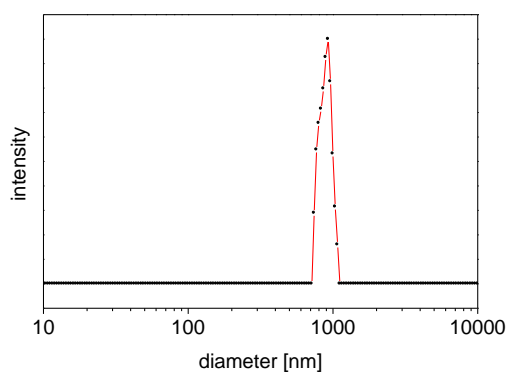
Fig. 90: DLS particle size distribution of washed CMT-1

The powder diffraction pattern (Fig. 91) of the dry product shows a weak reflection at 2.3 ° (2 θ), which is typical for CTMA$^+$ templated mesopores (Fig. 77 Chapter 6.1).
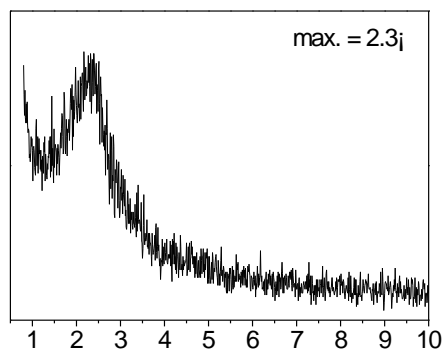

Fig. 91: Powder diffraction pattern of the washed sample CMT-1

Although the material seems to possess a certain mesostructure, TEM investigations (Fig. 92) could not confirm the existence of mesopores: The material possibly exhibits a fibrous structure, but it was not further analysed.
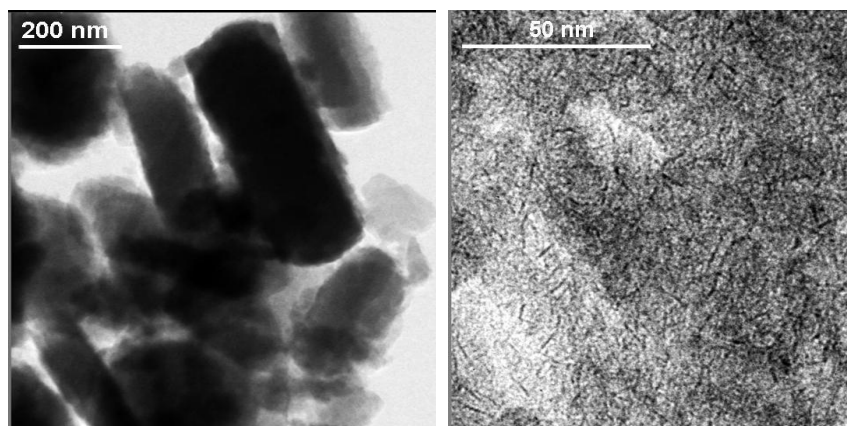
Fig. 92: TEM-micrographs of the washed sample CMT-1

The particles appear anisotropic with an irregular particle size distribution. At higher magnification, an undefined mesostructure in the material can be observed. However, it is not clear if this structure formed as a result of adding the template. Therefore, the washed product was subjected to an extraction procedure and the weight loss before and after this treatment was determined with TGA (Fig. 93).
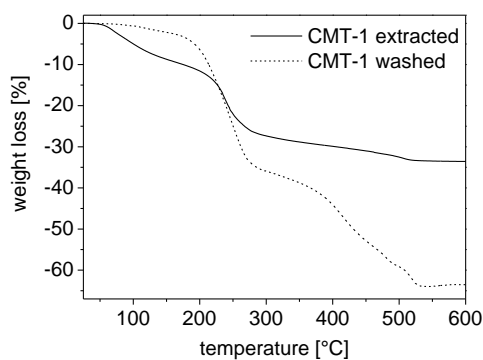

Fig. 93: Thermogravimetric analysis of washed and extracted sample CMT-1

Heating of the washed product caused two distinct steps in the weight loss. The first one at about 250 °C could be assigned either to the template decomposition or further condensation under elimination of alkoxygroups. The second step at higher temperatures between 400 and 500 °C might be due to complexing triethanolamine residues. After extraction, the weight loss is much lower – but it cannot be assured that the material is completely extracted mesoporous titania.

Elimination of the template should also be achieved after heating to 300 °C. Calcination at temperatures up to 350 °C is also claimed in several publications. [144] Both materials – extracted (CMT-1-e) and calcined (CMT-1-c) - were investigated by XRD (Fig. 94).The initial reflection at 2.3 °, and thus the mesostructure, completely disappeared after the treatment.
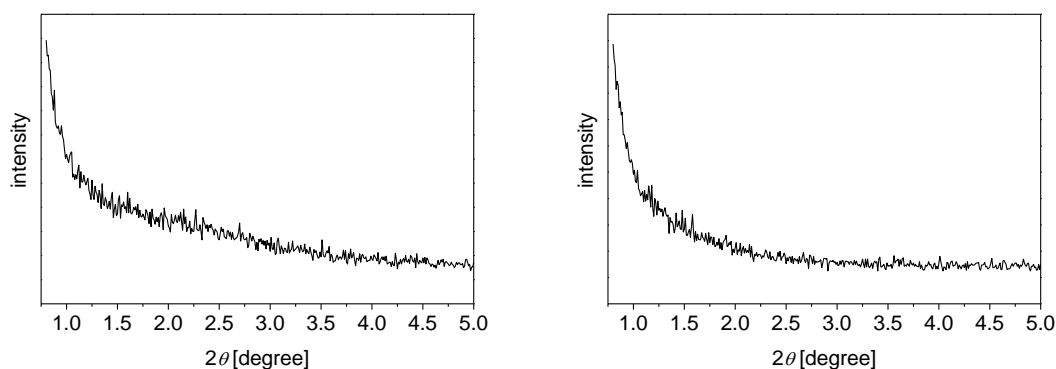

Fig. 94: XRD pattern of (a): calcined (CMT-1-c) and (b): extracted (CMT-1-e) material

Nitrogen sorption analysis also suggests the absence of ordered mesopores in both materials (Fig. 95). The isotherms are typical for an ink-bottle type pore system, but the difference in the adsorption and the desorption step argue against pore channels with a

defined diameter. The BET-surface areas of the calcined and extracted material are $80 \ m^2 \ g^{-1}$ and $200 \ m^2 \ g^{-1}$, respectively. One would expect a significantly higher specific surface area in ordered mesoporous titania, even though it can not reach the value of a comparable mesoporous silica, due to the higher density of TiO_2.

The DFT-pore size distribution was not calculated because no appropriate model is available at this time. As expected from the isotherm, a BJH pore size calculation regarding the adsorption branch gives a rather undefined and meaningless distribution.

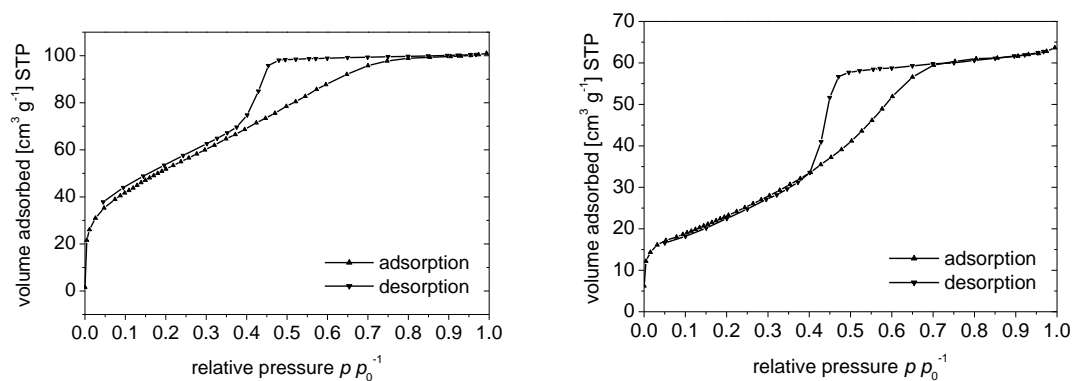Fig. 95: N_2-isotherms of extracted (CMT-1-e) and calcined (CMT-1-c) samples

In order to improve the condensation of the inorganic material and possibly an enhanced debonding of the complexing triethanolamine, the synthesis was repeated at an elevated temperature. The reaction at 50 °C resulted only in minor improvements, for example, a more pronounced reflection at about 2.3 ° in x-ray diffraction (Fig. 96).
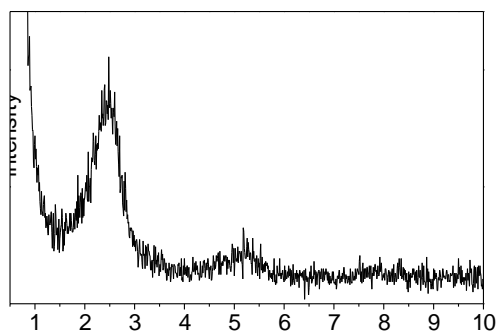
Fig. 96: Powder diffraction pattern of CMT-2

The particle size distribution in DLS as well as TGA data and sorption analysis showed no significant difference or improvement. In a further attempt to improve the condensation and debonding of triethanolamine, the suspension of CMT-1 was autoclaved at 100 °C after synthesis. Again, the peaks in the XRD powder pattern were more intensive and even showed higher-order reflections at 4.6 ° and 6.9 ° (Fig. 97).
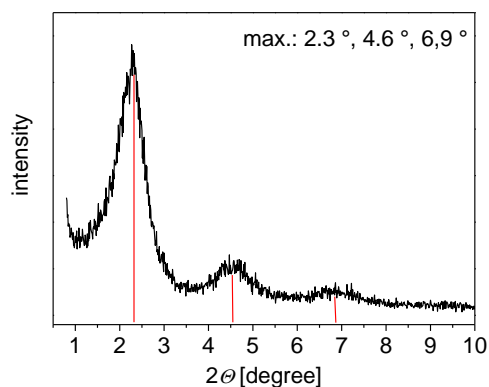
Fig. 97: Powder diffraction pattern of CMT-1A autoclaved at 100 °C

The positions of the reflections indicate the existence of a lamellar structure. This structure is believed to be the thermodynamically more stable one. The results in transmission electron microscopy (Fig. 98) could only confirm the expected lamellar structure.
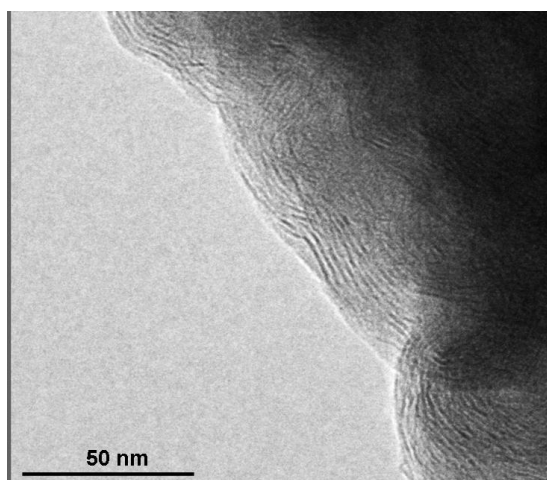
Fig. 98: TEM-micrograph of CMT-1A autoclaved at 100 °C

As expected for lamellar systems, template removal resulted in a loss of the mesostructure as shown in XRD patterns in Fig. 99.
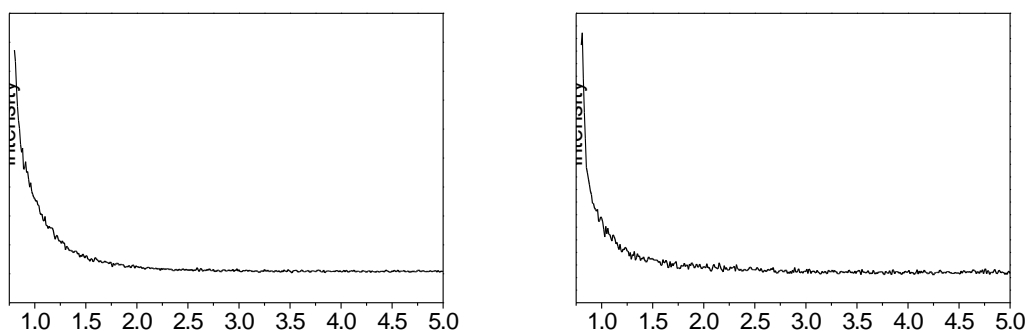
Fig. 99: Powder diffraction pattern of the (a) calcined (CMT-1A-c) and (b) extracted
(CMT-1A-e) material

The combination of solid template (CTAB) and titania precursor might be
disadvantageous for the formation of nanoparticles. Thus, in further experiments, an
aqueous solution of the template was prepared and heated, before the slowly
hydrolyzing precursor was added (CMT-3). After hydrolysis at elevated temperature
(60 °C), a homogeneous colloidal suspension with a narrow particle size distribution
was obtained (Fig. 100).
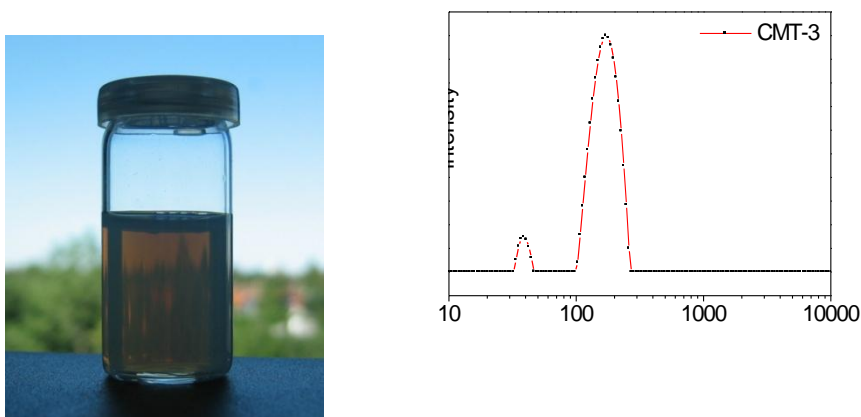
Fig. 100: Colloidal suspension and particle size distribution (DLS) of CMT-3

The product was subjected to the same extraction process as the mesoporous silica particles in Chapter 4.2. The particles in the resulting ethanolic suspension were agglomerated to a high degree. After drying, the product was slightly yellow and adhesive. TGA (Fig. 101) showed that the template was removed for the most part, but the material still seems to contain a noteworthy amount of triethanolamine, as already observed in the sample CMT-1.
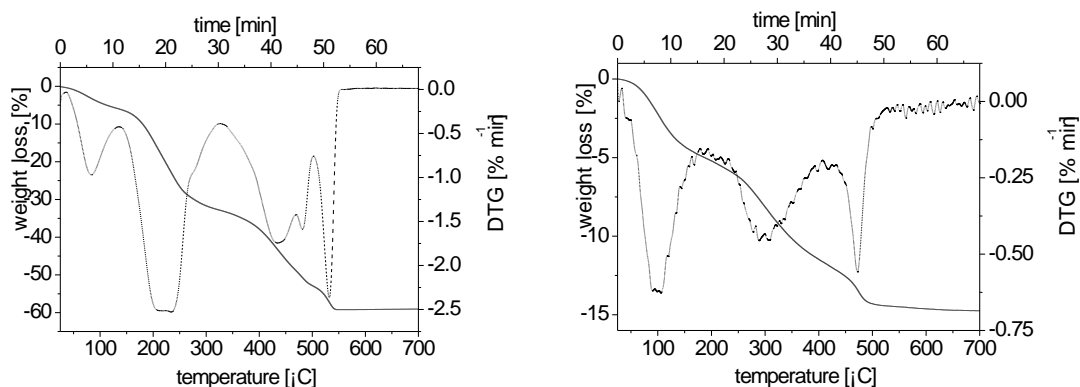
Fig. 101: TGA data of washed CMT-3 before and after extraction procedure

However, the nitrogen sorption isotherm of this sample differs from the one of CMT-2. The isotherm does not show such a pronounced hysteresis loop and the specific surface area is significantly higher ($330\ m^2\ g^{-1}$). The pore size distribution (DFT) shows a broadening on both sides of the typical peak for $CTMA^+$ at around 3 nm (Fig. 102).
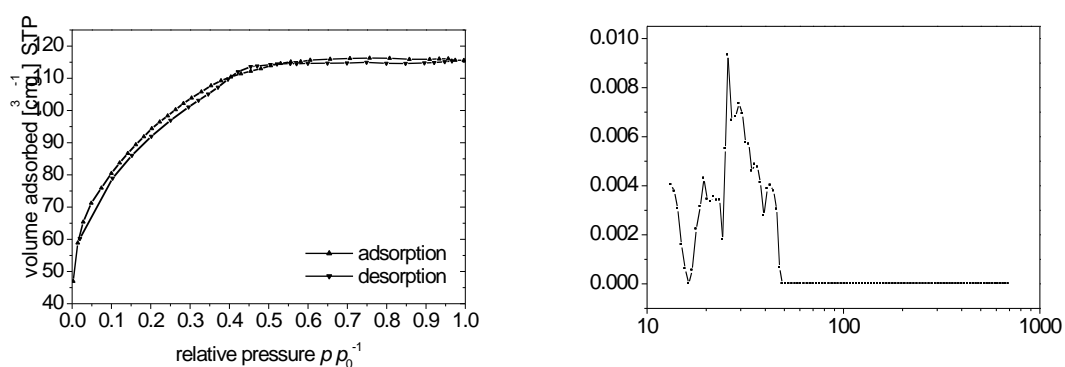
Fig. 102: N_2 sorption isotherm and DFT pore size distribution of extracted CMT-3

Variation of the synthesis conditions such as temperature or batch composition as well as the exchange of the template by shorter (dodecyltrimethylammonium chloride) or neutral substitutes (dodecyl amine) in further experiments did not lead to improved materials and were therefor not shown here. The replacement of the precursor with related complexes, e.g., titanium diisopropoxide bis(acetylacetonate) was unsuccessful because of a poor solubility in the aqueous medium. The results of the first experiments described above point out that, in contrast to the silica material, the basic synthesis procedure for mesoporous titania is connected to several problems. Especially in the presence of triethanolamine, extraction and redispersion is challenging.

Thus, the synthesis conditions were completely changed from basic to acidic conditions. Several synthesis procedures for mesoporous titania in acidic medium can be found in the literature.[143, 145, 146] One promising method described by Soler-Illia et al.[142] is based on the EISA approach for mesoporous TiO_2 thin films. This recipe was chosen as basis for the synthesis of colloidal suspensions of mesoporous titanium dioxide nanoparticles. The newly developed synthesis also started from a clear solution that was heated under reflux. The formation of TiO_2 particles in the initial solution caused a slowly increasing turbidity resulting in a white viscous suspension. Subsequent washing and redispersion led to an ethanolic suspension of titanium dioxide nanoparticles. Peptization of the particles was realized by addition of very small amounts of water. The resulting colloidal, translucent suspensions showed a narrow particle size

distribution in dynamic light scattering (DLS) with a mean particle size of 130 nm (Fig. 103).
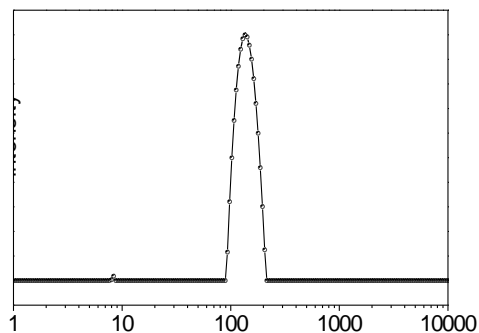
Fig. 103: Particle size distribution (DLS) of an ethanolic colloidal suspension of CMT-4

Electron microscopy confirmed the existence of discrete particles in the nanometer range. The TiO_2 nanoparticles can be described as prolate spheroids of approximately the same average size as indicated by DLS. (Fig. 104).
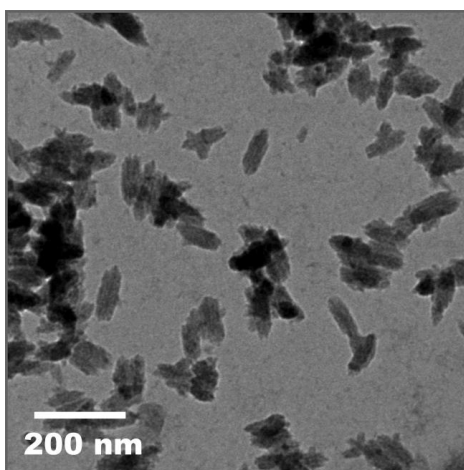
Fig. 104: TEM-micrograph of CMT-4

Because of this anisotropic shape one can expect a certain order either due to template interaction or crystallinity. Therefore, a dried sample of CMT-4 and CMT-5 was investigated in thermogravimetric analysis.
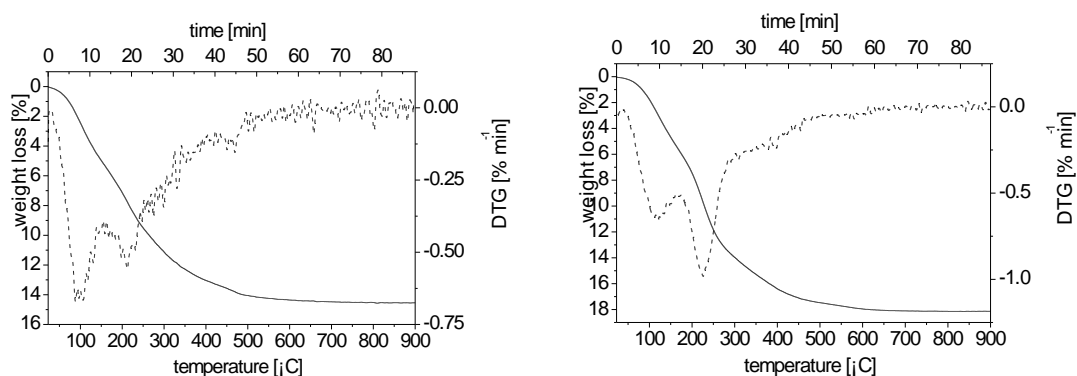
Fig. 105: TGA data of washed CMT-4 (a) and washed CMT-5 (b)

Sample CMT-4 and the product synthesized with the same procedure but without any template (CMT-5) do hardly show any difference. The synthesis was also carried out with different other templates − anionic and cationic (palmitic acid, CTAC) or neutral (pluronic, dodecylamine) template. In no case, an ordered or disordered mesoporous structure caused by organic templates could be confirmed. Thus, the weight loss at around 250 °C, which is typically assigned to template elimination in mesoporous silica materials, cannot be attributed to the template in the case of CMT-4. As this step can also be observed in CMT-5, it is probably caused by further condensation of the inorganic network and decomposition of alkoxy groups. This relatively high weight loss may be due to incomplete crystallinity of the samples. Nevertheless, the materials show

a certain crystallinity in Raman spectroscopy. The apparent signals can be attributed to rutile.
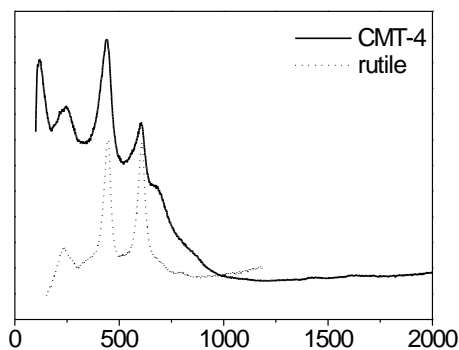
Fig. 106: Raman spectra of CMT-4 and spectra of rutile

X-ray powder diffraction patterns confirmed the existence of a crystalline phase in the dry powder. The relatively broad signals indicate the existence of small particles.
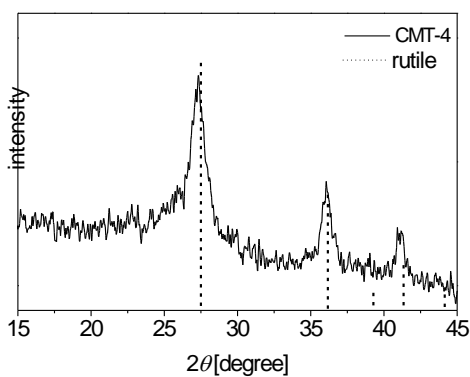
Fig. 107: X-ray powder diffraction pattern of CMT-4

Nitrogen sorption analyses (Fig. 108) showed that both materials exhibit a certain mesoporosity. Due to the shape of the isotherms and hysteresis loops, the existence of a channel-like pore structure can be excluded.
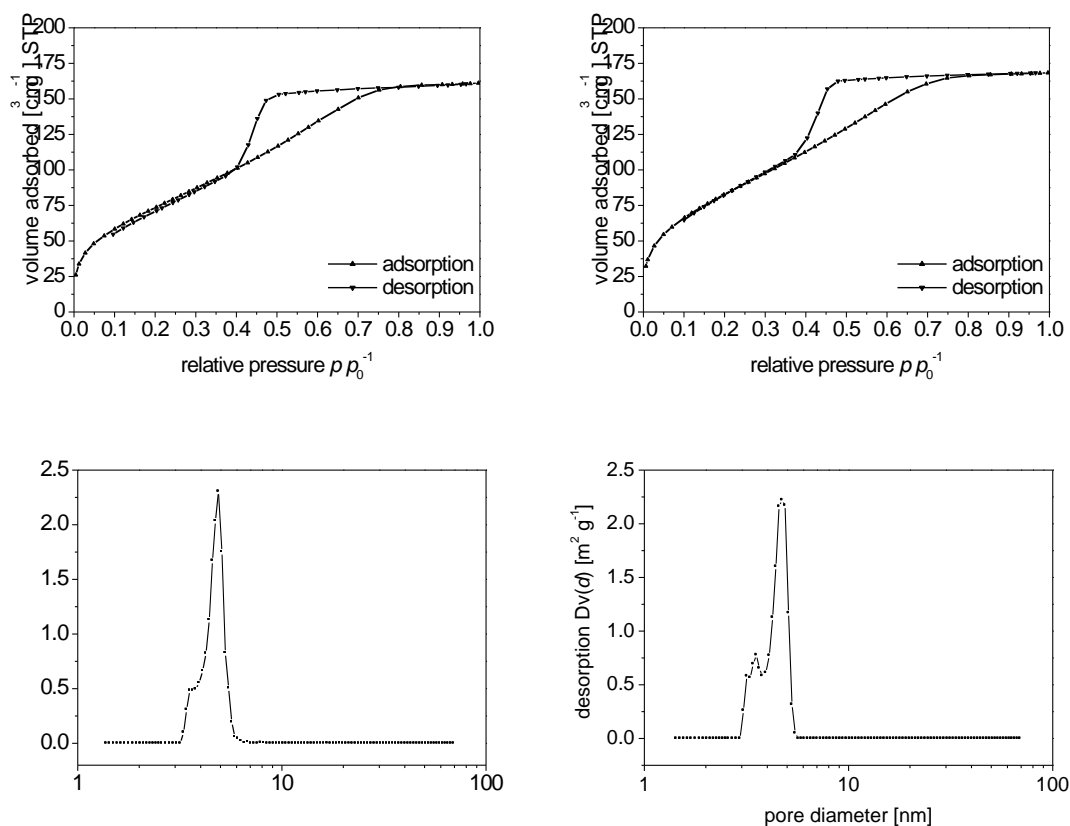
Fig. 108: N_2 sorption data of CMT-4 (l.) and CMT-5 (r.)

These findings led to the conclusion that the interaction of template and titanium precursor in the described procedures seems to be too weak to build up a mesostructure. This interpretation is corroborated by the fact that the best results concerning the surface area of the resulting particles were achieved without any template. The measured pore size is not influenced by the addition of template. CMT-5 showed a BET-surface area of

more than 300 m^2 g^{-1} and a relatively narrow pore size distribution with a diameter around 5 nm (Table 9).

Table 9: Nitrogen sorption data of CMT-4 and CMT-5

	CMT-4	CMT-5
Surface area (BET)	276 m^2 g^{-1}	311 m^2 g^{-1}
Total pore volume	0.24 cm^3 g^{-1}	0.25 cm^3 g^{-1}
Mean pore width	4.8 nm	4.7 nm

The synthesis of similar hydrosols is already known.[147] The existence of a mesoporous structure caused by agglomeration of the TiO$_2$ nanoparticles and the resulting high surface area is described in literature.[148, 149] Due to the easy redispersability of the washed particles and the high quality of the final ethanolic suspensions, the material can be used for the preparation of homogeneous thin films by spin-coating.[150]

Homogeneous Thin Films

For the preparation of homogeneous thin films, the synthesis without template (CMT-5) was repeated. After purification of the nanoparticles received from hydrothermal treatment (CMT-6), the colloidal suspension was used for the preparation of thin film. Fig. 109 shows the mean particle size (80 nm) of the suspended titania nanoparticles in the coating suspension.
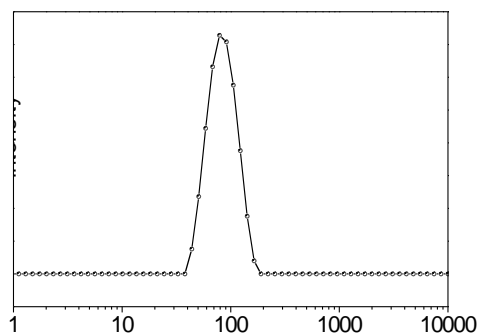
Fig. 109: Particle size distribution (DLS) of CMT-6

Fig. 110 shows an image of a silicon wafer with a thin film of titania nanoparticles. The film was prepared by spin-coating two times with a suspension containing about 3 wt % of CMT-6.
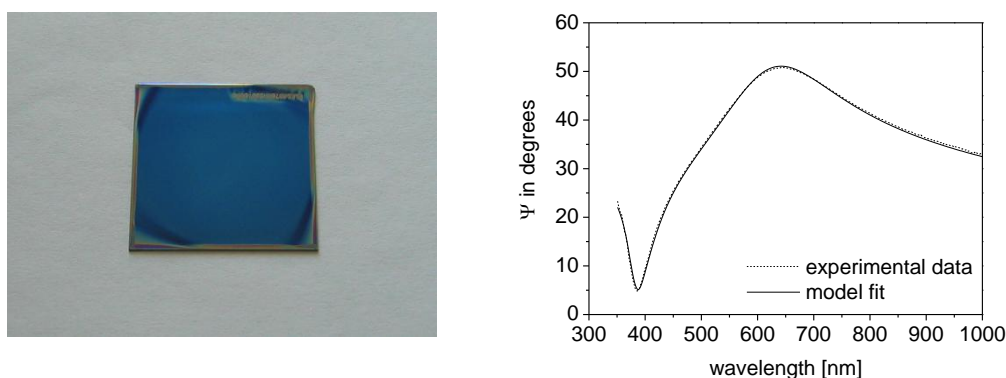
Fig. 110: Thin film of CMT-6 (107 nm) on a silicon wafer and ellipsometric data

The film appears very homogeneous and transparent and thus has a definite interference color. Ellipsometric measurements resulted in a film thickness of 107 nm. The same film was deposited on a quartz crystal microbalance chip. In order to achieve a higher thickness, the chip was coated four times. The optical characterization was performed with ellipsometry assuming the following theoretic model: 0: the gold electrode was chosen to be infinitely thick (1 mm); 1: the material (titania nanoparticles) is described with a Cauchy layer. Starting with a guessed film thickness of 200 nm, the subsequent fitting of the thickness and the Cauchy parameters resulted in a film thickness of 187 nm.

The measurement was performed in a liquid cell in a flow of nitrogen. It was repeated in an atmosphere of gaseous toluene with a partial pressure of 0.943 ($p\,p_0^{-1}$). Fig. 111 shows the change in the ellipsometric data due to physisorption of toluene.
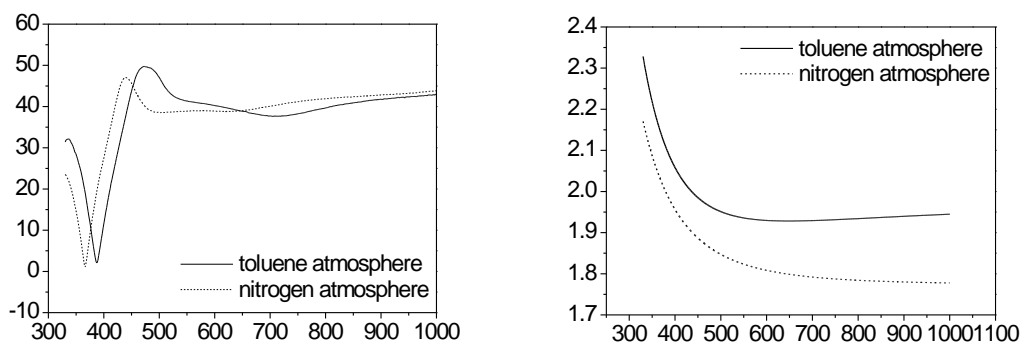
Fig. 111: Ellipsometry data of a thin film of CMT-6 on a QCM chip in nitrogen (dashed line) and toluene (solid line) atmosphere

The refractive index n_D of the film changes from 1.80 to 1.93 when filled with toluene ($n_D = 1.5$). With the Lorentz-Lorenz equation for ellipsometric porosimetry (EP)[55] a porosity of 16 % can be specified. The sorption measurement was repeated in a quartz crystal microbalance at different partial pressures of toluene to record a full sorption isotherm (Fig. 112).
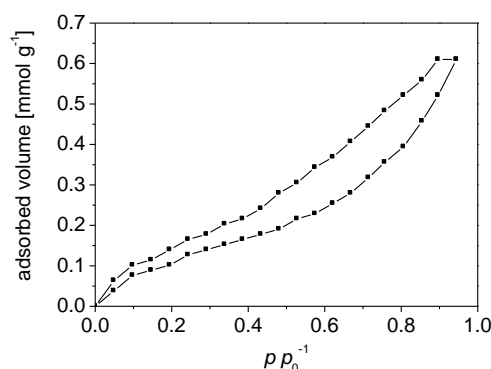
Fig. 112: Toluene sorption isotherm of a thin film of CMT-6 recorded in a QCM

The weight increase due to film deposition was 37.6 µg per cm^2. With a film thickness of 187 nm, a density of 2.01 g cm^{-3} can be calculated. The maximum weight increase due to toluene adsorption was 2.1 µg per cm^2 or 0.11 g per cm^3, respectively. With a density of 0.87 g cm^{-3} for liquid toluene, a porosity of 13 % can be calculated, which coincides well with the value determined with ellipsometric porosimetry.

Conclusion

The synthesis of templated mesoporous titanium dioxide nanoparticles similar to the silica analogues introduced in Chapter 4.2 could not be realized. The TiO$_2$ particles forming in the acidic medium by a simple sol-gel process often show a higher surface area and are much easier to redisperse than particles obtained in the basic synthesis. Although the general synthesis procedure is already known for a long time, the resulting colloidal suspensions are ideal candidates for the preparation of porous thin films. Especially, if the synthesis by evaporation induced self-assembly is connected to

problems, the usage of these suspensions can be an interesting alternative. Despite of their porosity, the prepared films have a high refractive index.

7. REFERENCES

[1]   Taniguchi, N., *On the Basic Concept of 'Nano-Technology'*, Japan Society of Precision Engineering, **1974**.

[2]   Drexler, E., *Engines of Creation: The Coming Era of Nanotechnology*, New York: Anchor Press/Doubleday, **1986**.

[3]   Drexler, E., *Nanosystems: Molecular Machinery, Manufacturing, and Computation:*, John Wiley & Sons Inc, **1992**.

[4]   Boncheva, M.; Whitesides, G. M.; Making things by self-assembly. *MRS Bull.* **2005**, *30*, 736-742.

[5]   Ter Minassian-Saraga, L.; Thin films including layers: terminology in relation to their preparation and characterization. *Pure Appl. Chem.* **1994**, *66*, 1667-1738.

[6]   Koga, K.; Ikeshoji, T.; Sugawara, K.-i.; Size- and Temperature-Dependent Structural Transitions in Gold Nanoparticles. *Phys. Rev. Lett.* **2004**, *92*, 115507.

[7]   Trewyn, B. G.; Giri, S.; Slowing, I. I.; Lin, V. S.-Y.; Mesoporous silica nanoparticle based controlled release, drug delivery, and biosensor systems. *Chem. Commun. (Cambridge, U. K.)* **2007**, 3236-3245.

[8]   Barbe, C.; Bartlett, J.; Kong, L.; Finnie, K.; Lin, H. Q.; Larkin, M.; Calleja, S.; Bush, A.; Calleja, G.; Silica particles: A novel drug-delivery system. *Adv. Mater. (Weinheim, Ger.)* **2004**, *16*, 1959-1966.

[9]   Joutsensaari, J.; Loivamaki, M.; Vuorinen, T.; Miettinen, P.; Nerg, A. M.; Holopainen, J. K.; Laaksonen, A.; Nanoparticle formation by ozonolysis of inducible plant volatiles. *Atmospheric Chemistry and Physics* **2005**, *5*, 1489-1495.

[10]   Mackenzie, J. D.; Bescher, E. P.; Chemical Routes in the Synthesis of Nanomaterials Using the Sol-Gel Process. *Acc. Chem. Res.* **2007**, *40*, 810-818.

[11]   Cushing, B. L.; Kolesnichenko, V. L.; O'Connor, C. J.; Recent Advances in the Liquid-Phase Syntheses of Inorganic Nanoparticles. *Chem. Rev. (Washington, DC, U. S.)* **2004**, *104*, 3893-3946.

[12]   Stober, W.; Fink, A.; Bohn, E.; Controlled growth of monodisperse silica spheres in the micron size range. *J. Colloid Interface Sci.* **1968**, *26*, 62-69.

REFERENCES

[13]   LaMer, V. K.; Dinegar, R. H.; Theory, Production and Mechanism of Formation of Monodispersed Hydrosols. *J. Am. Chem. Soc.* **1950**, *72*, 4847-4854.

[14]   Sing, K. S. W.; Everett, D. H.; Haul, R. A. W.; Moscou, L.; Pierotti, R. A.; Rouquerol, J.; Siemieniewska, T.; Reporting Physisorption Data For Gas/Solid Systems with Special Reference to the Determination of Surface Area and Porosity. *Pure Appl. Chem.* **1985**, *57*, 603-619.

[15]   Cundy, C. S.; Cox, P. A.; The hydrothermal synthesis of zeolites: Precursors, intermediates and reaction mechanism. *Microporous Mesoporous Mater.* **2005**, *82*, 1-78.

[16]   Baerlocher, C.; McCusker, L. B.; Database of Zeolite Structure: www.iza-structure.org/databases

[17]   Yan, Y.; Silica zeolite ultra low-k dielectric thin films. *PMSE Prepr.* **2004**, *90*, 89-94.

[18]   Fowler, C. E.; Khushalani, D.; Lebeau, B.; Mann, S.; Nanoscale materials with mesostructured interiors. *Adv. Mater. (Weinheim, Ger.)* **2001**, *13*, 649-652.

[19]   Yang, P.; Zhao, D.; Margolese, D. I.; Chmelka, B. F.; Stucky, G. D.; Block Copolymer Templating Syntheses of Mesoporous Metal Oxides with Large Ordering Lengths and Semicrystalline Framework. *Chem. Mater.* **1999**, *11*, 2813-2826.

[20]   Brinker, C. J.; Lu, Y. F.; Sellinger, A.; Fan, H. Y.; Evaporation-induced self-assembly: Nanostructures made easy. *Adv. Mater. (Weinheim, Ger.)* **1999**, *11*, 579-585.

[21]   Liu, J.; Shin, Y.; Nie, Z. M.; Chang, J. H.; Wang, L. Q.; Fryxell, G. E.; Samuels, W. D.; Exarhos, G. J.; Molecular assembly in ordered mesoporosity: A new class of highly functional nanoscale materials. *J. Phys. Chem. A* **2000**, *104*, 8328-8339.

[22]   Burkett, S. L.; Sims, S. D.; Mann, S.; Synthesis of hybrid inorganic-organic mesoporous silica by co-condensation of siloxane and organosiloxane precursors. *Chem. Commun. (Cambridge, U. K.)* **1996**, 1367-1368.

[23]   Burleigh, M. C.; Markowitz, M. A.; Spector, M. S.; Gaber, B. P.; Direct synthesis of periodic mesoporous organosilicas: Functional incorporation by co-condensation with organosilanes. *J. Phys. Chem. B* **2001**, *105*, 9935-9942.

[24]   Huh, S.; Wiench, J. W.; Yoo, J.-C.; Pruski, M.; Lin, V. S.-Y.; Organic Functionalization and Morphology Control of Mesoporous Silicas via a Co-Condensation Synthesis Method. *Chem. Mater.* **2003**, *15*, 4247-4256.

[25]   Igarashi, N.; Hashimoto, K.; Tatsumi, T.; Studies on the structural stability of mesoporous molecular sieves organically functionalized by a direct method. *J. Mater. Chem.* **2002**, *12*, 3631-3636.

[26]   Trewyn, B. G.; Slowing, I. I.; Giri, S.; Chen, H.-T.; Lin, V. S. Y.; Synthesis and Functionalization of a Mesoporous Silica Nanoparticle Based on the Sol-Gel Process and Applications in Controlled Release. *Acc. Chem. Res.* **2007**, *40*, 846-853.

[27]   Diaz, I.; Mohino, F.; Perez-Pariente, J.; Sastre, E.; Study by TG-MS of the oxidation of SH-MCM-41 to SO3H-MCM-41. *Thermochim. Acta* **2004**, *413*, 201-207.

[28]   Radu, D. R.; Lai, C.-Y.; Huang, J.; Shu, X.; Lin, V. S. Y.; Fine-tuning the degree of organic functionalization of mesoporous silica nanosphere materials via an interfacially designed co-condensation method. *Chem. Commun. (Cambridge, U. K.)* **2005**, 1264-1266.

[29]   Kumar, R.; Chen, H. T.; Escoto, J. L. V.; Lin, V. S. Y.; Pruski, M.; Template Removal and Thermal Stability of Organically Functionalized Mesoporous Silica Nanoparticles. *Chem. Mater.* **2006**, *18*, 4319-4327.

[30]   Kawi, S.; Lai, M. W.; Supercritical fluid extraction of surfactant template from MCM-41. *Chem. Commun. (Cambridge, U. K.)* **1998**, 1407-1408.

[31]   Tian, B.; Liu, X.; Yu, C.; Gao, F.; Luo, Q.; Xie, S.; Tu, B.; Zhao, D.; Microwave assisted template removal of siliceous porous materials. *Chem. Commun. (Cambridge, U. K.)* **2002**, 1186-1187.

[32]   Lang, N.; Tuel, A.; A Fast and Efficient Ion-Exchange Procedure To Remove Surfactant Molecules from MCM-41 Materials. *Chem. Mater.* **2004**, *16*, 1961-1966.

[33]   Schubert, U.; Chemical modification of titanium alkoxides for sol-gel processing. *J. Mater. Chem.* **2005**, *15*, 3701-3715.

[34]   Nagamine, S.; Sasaoka, E.; Synthesis of Nanostructured Titania Templated by Anionic Surfactant in Acidic Conditions. *Journal of Porous Materials* **2002**, *9*, 167-173.

[35]   O'Regan, B.; Graetzel, M.; A low-cost, high-efficiency solar cell based on dye-sensitized colloidal titanium dioxide films. *Nature (London, U.K.)* **1991**, *353*, 737-740.

[36]   Evans, U.; Die Interferenzfarben dünner Filme von Oxyden, Sulfiden oder Jodiden auf Metallen. *Colloid Polym. Sci.* **1934**, *69*, 129-137.

[37]   Raacke, J.; Interferenzfarben dünner Schichten (V2.7): http://www.raacke.de/index.html?airy.html

[38]   Parker, A. R.; McKenzie, D. R.; Large, M. C. J.; Multilayer reflectors in animals using green and gold beetles as contrasting examples. *J. Exp. Biol.* **1998**, *201*, 1307-1313.

[39]   Palaniappan, A.; Su, X.; Tay, F.; Functionalized mesoporous silica films for gas sensing applications. *J. Electroceram.* **2006**, *16*, 503-505.

[40]   Nicole, L.; Boissiere, C.; Grosso, D.; Hesemann, P.; Moreau, J.; Sanchez, C.; Advanced selective optical sensors based on periodically organized mesoporous hybrid silica thin films. *Chem. Commun. (Cambridge, U. K.)* **2004**, 2312-2313.

[41]   Yuliarto, B.; Zhou, H.; Yamada, T.; Honma, I.; Katsumura, Y.; Ichihara, M.; Effect of Tin Addition on Mesoporous Silica Thin Film and Its Application for Surface Photovoltage NO2 Gas Sensor. *Anal. Chem.* **2004**, *76*, 6719-6726.

[42]   Bearzotti, A.; Mio Bertolo, J.; Innocenzi, P.; Falcaro, P.; Traversa, E.; Relative humidity and alcohol sensors based on mesoporous silica thin films synthesised from block copolymers. *Sens. Actuators, B* **2003**, *B95*, 107-110.

[43]   Wirnsberger, G.; Scott, B. J.; Stucky, G. D.; pH sensing with mesoporous thin films. *Chem. Commun. (Cambridge, U. K.)* **2001**, 119-120.

[44]   Choi, S. Y.; Mamak, M.; vonFreymann, G.; Chopra, N.; Ozin, G. A.; Mesoporous Bragg Stack Color Tunable Sensors. *Nano Lett.* **2006**, *6*, 2456-2461.

[45]   Tosheva, L.; Valtchev, V. P.; Nanozeolites: Synthesis, Crystallization Mechanism, and Applications. *Chem. Mater.* **2005**, *17*, 2494-2513.

[46]   Bein, T.; Zeolitic host-guest interactions and building blocks for the self-assembly of complex materials. *MRS Bull.* **2005**, *30*, 713-720.

[47]   Slowing, I.; Trewyn, B. G.; Lin, V. S. Y.; Effect of Surface Functionalization of MCM-41-Type Mesoporous Silica Nanoparticles on the Endocytosis by Human Cancer Cells. *J. Am. Chem. Soc.* **2006**, *128*, 14792-14793.

[48]   Schulz-Ekloff, G.; Wohrle, D.; van Duffel, B.; Schoonheydt, R. A.; Chromophores in porous silicas and minerals: preparation and optical properties. *Microporous Mesoporous Mater.* **2002**, *51*, 91-138.

[49]   Scott, B. J.; Wirnsberger, G.; Stucky, G. D.; Mesoporous and mesostructured materials for optical applications. *Chem. Mater.* **2001**, *13*, 3140-3150.

[50]   Lee, U. H.; Kim, M.-H.; Kwon, Y.-U.; Mesoporous thin films with accessible pores from surfaces. *Bull. Korean Chem. Soc.* **2006**, *27*, 808-816.

[51]   Sing, K. S. W.; Everett, D. H.; Haul, R. A. W.; Moscou, L.; Pierotti, R. A.; Rouquerol, J.; Siemieniewska, T.; Reporting physisorption data for gas/solid systems with special reference to the determination of surface area and porosity (Recommendations 1984). *Pure Appl. Chem.* **1985**, *57*, 603-619.

[52]   Brunauer, S.; Emmett, P. H.; Teller, E.; Adsorption of Gases in Multimolecular Layers. *J. Am. Chem. Soc.* **1938**, *60*, 309-319.

[53]   Thommes, M.; Kohn, R.; Froba, M.; Sorption and Pore Condensation Behavior of Nitrogen, Argon, and Krypton in Mesoporous MCM-48 Silica Materials. *J. Phys. Chem. B* **2000**, *104*, 7932-7943.

[54]   Moeller, A.; Yang, X.; Caro, J.; Staudt, R.; Measurements of the adsorption of n-alkanes on 5A zeolites. *Chem. Ing. Tech.* **2006**, *78*, 1831-1836.

[55] Baklanov, M. R.; Mogilnikov, K. P.; Non-destructive characterisation of porous low-k dielectric films. *Microelectron. Eng.* **2002**, *64*, 335-349.

[56] Eslava, S.; Baklanov, M. R.; Kirschhock, C. E. A.; Iacopi, F.; Aldea, S.; Maex, K.; Martens, J. A.; Characterization of a Molecular Sieve Coating Using Ellipsometric Porosimetry. *Langmuir* **2007**, *23*, 12811-12816.

[57] Mintova, S.; Nanosized molecular sieves. *Collect. Czech. Chem. Commun.* **2003**, *68*, 2032-2054.

[58] Holmberg, B. A.; Wang, H.; Yan, Y.; High silica zeolite Y nanocrystals by dealumination and direct synthesis. *Microporous Mesoporous Mater.* **2004**, *74*, 189-198.

[59] Zhu, G.; Qiu, S.; Yu, J.; Sakamoto, Y.; Xiao, F.; Xu, R.; Terasaki, O.; Synthesis and Characterization of High-Quality Zeolite LTA and FAU Single Nanocrystals. *Chem. Mater.* **1998**, *10*, 1483-1486.

[60] Kecht, J.; Mintova, S.; Bein, T.; Nanosized Zeolites Templated by Metal-Ammine Complexes. *Chem. Mater.* **2007**, *19*, 1203-1205.

[61] Larsen, S. C.; Nanocrystalline Zeolites and Zeolite Structures: Synthesis, Characterization, and Applications. *Journal of Physical Chemistry C* **2007**, *111*, 18464-18474.

[62] Larlus, O.; Mintova, S.; Bein, T.; Environmental syntheses of nanosized zeolites with high yield and monomodal particle size distribution. *Microporous Mesoporous Mater.* **2006**, *96*, 405-412.

[63] Hsu, C.-Y.; Chiang, A. S. T.; Selvin, R.; Thompson, R. W.; Rapid Synthesis of MFI Zeolite Nanocrystals. *J. Phys. Chem. B* **2005**, *109*, 18804-18814.

[64] Lew, C. M.; Li, Z.; Zones, S. I.; Sun, M.; Yan, Y.; Control of size and yield of pure-silica-zeolite MFI nanocrystals by addition of methylene blue to the synthesis solution. *Microporous Mesoporous Mater.* **2007**, *105*, 10-14.

[65] Li, Z. J.; Li, S.; Luo, H. M.; Yan, Y. S.; Effects of Crystallinity in Spin-On Pure-Silica-Zeolite MFI Low-Dielectric-Constant Films. *Adv. Funct. Mater.* **2004**, *14*, 1019-1024.

[66] Li, Z.; Lew, C. M.; Li, S.; Medina, D. I.; Yan, Y.; Pure-Silica-Zeolite MEL Low-k Films from Nanoparticle Suspensions. *J. Phys. Chem. B* **2005**, *109*, 8652-8658.

[67] Mintova, S.; Reinelt, M.; Metzger, T. H.; Senker, J.; Bein, T.; Pure silica beta colloidal zeolite assembled in thin films. *Chem. Commun. (Cambridge, U. K.)* **2003**, 326-327.

[68] Camblor, M. A.; Corma, A.; Valencia, S.; Spontaneous nucleation and growth of pure silica zeolite-b free of connectivity defects. *Chem. Commun. (Cambridge, U. K.)* **1996**, 2365-2366.

[69] Serrano, D. P.; Van Grieken, R.; Sanchez, P.; Sanz, R.; Rodriguez, L.; Crystallization mechanism of all-silica zeolite beta in fluoride medium. *Microporous Mesoporous Mater.* **2001**, *46*, 35-46.

[70] Wang, Z.; Mitra, A.; Wang, H.; Huang, L.; Yan, Y.; Pure silica zeolite films as low-k dielectrics by spin-on of nanoparticle suspensions. *Adv. Mater. (Weinheim, Ger.)* **2001**, *13*, 1463-1466.

[71] Mintova, S.; Bein, T.; Microporous Films Prepared by Spin-Coating Stable Colloidal Suspensions of Zeolites. *Adv. Mater. (Weinheim, Ger.)* **2001**, *13*, 1880-1883.

[72] Johnson, M.; Li, Z.; Wang, J.; Yan, Y.; Mechanical characterization of zeolite low dielectric constant thin films by nanoindentation. *Thin Solid Films* **2007**, *515*, 3164-3170.

[73] Tatlier, M.; Demir, M.; Tokay, B.; Erdem-Senatalar, A.; Kiwi-Minsker, L.; Substrate heating method for coating metal surfaces with high-silica zeolites: ZSM-5 coatings on stainless steel plates. *Microporous Mesoporous Mater.* **2007**, *101*, 374-380.

[74] Barrett, P. A.; Camblor, M. A.; Corma, A.; Jones, R. H.; Villaescusa, L. A.; Structure of ITQ-4, a New Pure Silica Polymorph Containing Large Pores and a Large Void Volume. *Chem. Mater.* **1997**, *9*, 1713-1715.

[75]   Selvam, T.; Aresipathi, C.; Mabande, G. T. P.; Toufar, H.; Schwieger, W.; Solid state transformation of TEAOH-intercalated kanemite into zeolite beta (BEA). *J. Mater. Chem.* **2005**, *15*, 2013-2019.

[76]   Schoeman, B. J.; Babouchkina, E.; Mintova, S.; Valtchev, V. P.; Sterte, J.; The Synthesis of Discrete Colloidal Crystals of Zeolite Beta and their Application in the Preparation of Thin Microporous Films. *Journal of Porous Materials* **2001**, *8*, 13-22.

[77]   Nery, J. G.; Hwang, S.-J.; Davis, M. E.; On the synthesis of SSZ-48, SSZ-43 and their variations. *Microporous Mesoporous Mater.* **2002**, *52*, 19-28.

[78]   Krijnen, S.; Sanchez, P.; Jakobs, B. T. F.; van Hooff, J. H. C.; A controlled post-synthesis route to well-defined and active titanium Beta epoxidation catalysts. *Microporous Mesoporous Mater.* **1999**, *31*, 163-173.

[79]   Bruggeman, D. A. G.; The calculation of various physical constants of heterogeneous substances. I. The dielectric constants and conductivities of mixtures composed of isotropic substances. *Annalen der Physik (Berlin, Germany)* **1935**, *24*, 665-679.

[80]   Kresge, C. T.; Leonowicz, M. E.; Roth, W. J.; Vartuli, J. C.; Beck, J. S.; Ordered Mesoporous Molecular-Sieves Synthesized by a Liquid-Crystal Template Mechanism. *Nature* **1992**, *359*, 710-712.

[81]   Qi, L. M.; Ma, J. M.; Cheng, H. M.; Zhao, Z. G.; Micrometer-sized mesoporous silica spheres grown under static conditions. *Chem. Mater.* **1998**, *10*, 1623-1626.

[82]   Huo, Q. S.; Zhao, D. Y.; Feng, J. L.; Weston, K.; Buratto, S. K.; Stucky, G. D.; Schacht, S.; Schuth, F.; Room temperature growth of mesoporous silica fibers: A new high-surface-area optical waveguide. *Adv. Mater. (Weinheim, Ger.)* **1997**, *9*, 974-978.

[83]   Li, Y. S.; Shi, J. L.; Hua, Z. L.; Chen, H. R.; Ruan, M. L.; Yan, D. S.; Hollow Spheres of Mesoporous Aluminosilicate with a Three-Dimensional Pore Network and Extraordinarily High Hydrothermal Stability. *Nano Lett.* **2003**, *3*, 609-612.

[84]   Cauvel, A.; Renard, G.; Brunel, D.; Monoglyceride synthesis by heterogeneous catalysis using MCM-41 type silicas functionalized with amino groups. *J. Org. Chem.* **1997**, *62*, 749-751.

[85]   Zhao, X. S.; Lu, G. Q.; Modification of MCM-41 by surface silylation with trimethylchlorosilane and adsorption study. *J. Phys. Chem. B* **1998**, *102*, 1556-1561.

[86]   Anwander, R.; SOMC@PMS. Surface organometallic chemistry at periodic mesoporous silica. *Chem. Mater.* **2001**, *13*, 4419-4438.

[87]   Qi, Z.-m.; Honma, I.; Zhou, H.; Ordered-mesoporous-silica-thin-film-based chemical gas sensors with integrated optical polarimetric interferometry. *Appl. Phys. Lett.* **2006**, *88*, 053503/053501-053503/053503.

[88]   Boissiere, C.; Kummel, M.; Persin, M.; Larbot, A.; Prouzet, E.; Spherical MSU-1 mesoporous silica particles tuned for HPLC. *Adv. Funct. Mater.* **2001**, *11*, 129-135.

[89]   Ren, J.; Ding, J.; Chan, K.-Y.; Wang, H.; Dual-Porosity Carbon Templated from Monosize Mesoporous Silica Nanoparticles. *Chem. Mater.* **2007**, *19*, 2786-2795.

[90]   Lu, J.; Liong, M.; Zink, J. I.; Tammanoi, F.; Mesoporous silica nanoparticles as a delivery system for hydrophobic anticancer drugs. *Small* **2007**, *3*, 1341-1346.

[91]   Asai, S.; Tominaga, Y.; Sumita, M.; Mesoporous silica as inorganic filler in polymer composites. *Zeoraito* **2006**, *23*, 117-124.

[92]   Lu, Y. F.; Fan, H. Y.; Stump, A.; Ward, T. L.; Rieker, T.; Brinker, C. J.; Aerosol-assisted self-assembly of mesostructured spherical nanoparticles. *Nature* **1999**, *398*, 223-226.

[93]   Suzuki, K.; Ikari, K.; Imai, H.; Synthesis of Silica Nanoparticles Having a Well-Ordered Mesostructure Using a Double Surfactant System. *J. Am. Chem. Soc.* **2004**, *126*, 462-463.

[94]   El Haskouri, J.; Ortiz de Zarate, D.; Guillem, C.; Beltran-Porter, A.; Caldes, M.; Marcos, M. D.; Beltran-Porter, D.; Latorre, J.; Amoros, P.; Hierarchical Porous Nanosized Organosilicas. *Chem. Mater.* **2002**, *14*, 4502-4504.

[95] Nooney, R. I.; Thirunavukkarasu, D.; Chen, Y.; Josephs, R.; Ostafin, A. E.; Synthesis of Nanoscale Mesoporous Silica Spheres with Controlled Particle Size. *Chem. Mater.* **2002**, *14*, 4721-4728.

[96] Rathousky, J.; Zukalova, M.; Kooyman, P. J.; Zukal, A.; Synthesis and characterization of colloidal MCM-41. *Colloids Surf., A* **2004**, *241*, 81-86.

[97] Cai, Q.; Luo, Z. S.; Pang, W. Q.; Fan, Y. W.; Chen, X. H.; Cui, F. Z.; Dilute solution routes to various controllable morphologies of MCM-41 silica with a basic medium. *Chem. Mater.* **2001**, *13*, 258-263.

[98] Moeller, K.; Kobler, J.; Bein, T.; Colloidal suspensions of nanometer-sized mesoporous silica. *Adv. Funct. Mater.* **2007**, *17*, 605-612.

[99] Moeller, K.; Kobler, J.; Bein, T.; Colloidal suspensions of mercapto-functionalized nanosized mesoporous silica. *J. Mater. Chem.* **2007**, *17*, 624-631.

[100] Sadasivan, S.; Khushalani, D.; Mann, S.; Synthesis and shape modification of organo-functionalized silica nanoparticles with ordered mesostructured interiors. *J. Mater. Chem.* **2003**, *13*, 1023-1029.

[101] Frye, C. L.; Vincent, G. A.; Finzel, W. A.; Pentacoordinate silicon compounds. V. Novel silatrane chemistry. *J. Am. Chem. Soc.* **1971**, *93*, 6805-6811.

[102] Verkade, J. G.; Atranes: new examples with unexpected properties. *Acc. Chem. Res.* **1993**, *26*, 483-489.

[103] Cabrera, S.; ElHaskouri, J.; Guillem, C.; Latorre, J.; BeltranPorter, A.; BeltranPorter, D.; Marcos, M. D.; Amoros, P.; Generalised syntheses of ordered mesoporous oxides: the atrane route. *Solid State Sci.* **2000**, *2*, 405-420.

[104] Zhao, X. S.; Lu, G. Q.; Whittaker, A. K.; Millar, G. J.; Zhu, H. Y.; Comprehensive study of surface chemistry of MCM-41 using ^{29}Si CP/MAS NMR, FTIR, pyridine-TPD, and TGA. *J. Phys. Chem. B* **1997**, *101*, 6525-6531.

[105] Socrates, G., *Infrared and Raman Characteristic Group Frequencies*, 3. ed., Wiley, **2005**.

[106] Okabayashi, H.; Izawa, K.; Yamamoto, T.; Masuda, H.; Nishio, E.; O'Connor, C. J.; Surface structure of silica gel reacted with 3-mercaptopropyltriethoxysilane and 3-aminopropyltriethoxysilane: formation of the S-S bridge structure and its characterization by Raman scattering and diffuse reflectance Fourier transform spectroscopic studies. *Colloid Polym. Sci.* **2002**, *280*, 135-145.

[107] Kobler, J.; Möller, K.; Bein, T.; Colloidal Suspensions of Functionalized Mesoporous Silica Nanoparticles. *ACS Nano* **2008**, *2*, 791-799.

[108] Sokolov, I.; Kievsky, Y. Y.; Kaszpurenko, J. M.; Self-assembly of ultrabright fluorescent silica particles. *Small* **2007**, *3*, 419-423.

[109] Ren, T.-Z.; Yuan, Z.-Y.; Su, B.-L.; Encapsulation of direct blue dye into mesoporous silica-based materials. *Colloids Surf., A* **2007**, *300*, 79-87.

[110] Laerte de Castro, F.; Santos, J. G.; Fernandes, G. J. T.; Souza de Araujo, A.; Fernandes, V. J.; Politi, M. J.; Brochsztain, S.; Solid state fluorescence of a 3,4,9,10-perylenetetracarboxylic diimide derivative encapsulated in the pores of mesoporous silica MCM-41. *Microporous Mesoporous Mater.* **2007**, *102*, 258-264.

[111] Wark, M.; Ganschow, M.; Rohlfing, Y.; Schulz-Ekloff, G.; Woehrle, D.; Methods of synthesis for the encapsulation of dye molecules in molecular sieves. *Stud. Surf. Sci. Catal.* **2001**, *135*, 3292-3300.

[112] Huang, D.-M.; Hung, Y.; Ko, B.-S.; Hsu, S.-C.; Chen, W.-H.; Chien, C.-L.; Tsai, C.-P.; Kuo, C.-T.; Kang, J.-C.; Yang, C.-S.; Mou, C.-Y.; Chen, Y.-C.; Highly efficient cellular labeling of mesoporous nanoparticles in human mesenchymal stem cells: implication for stem cell tracking. *FASEB J.* **2005**, *19*, 2014-2016.

[113] Torney, F.; Trewyn, B. G.; Lin, V. S. Y.; Wang, K.; Mesoporous silica nanoparticles deliver DNA and chemicals into plants. *Nat. Nanotechnol.* **2007**, *2*, 295-300.

[114]   Chen, J. Y.; Pan, F. M.; Chang, L.; Cho, A. T.; Chao, K. J.; Thermal stability of trimethylsilylated mesoporous silica thin films as the ultralow-k dielectric for copper interconnects. *Journal of Vacuum Science & Technology, B: Microelectronics and Nanometer Structures--Processing, Measurement, and Phenomena* **2005**, *23*, 2034-2040.

[115]   Innocenzi, P.; Martucci, A.; Guglielmi, M.; Bearzotti, A.; Traversa, E.; Pivin, J. C.; Mesoporous silica thin films for alcohol sensors. *J. Eur. Ceram. Soc.* **2001**, *21*, 1985-1988.

[116]   Brinker, C. J.; Evaporation-induced self-assembly. Functional nanostructures made easy. *MRS Bull.* **2004**, *29*, 631-640.

[117]   Mason, G.; A model of the pore space in a random packing of equal spheres. *J. Colloid Interface Sci.* **1971**, *35*, 279-287.

[118]   Slobozhanin, L. A.; Alexander, J. I. D.; Collicott, S. H.; Gonzalez, S. R.; Capillary pressure of a liquid in a layer of close-packed uniform spheres. *Physics of Fluids* **2006**, *18*, 082104-082115.

[119]   Mayer, R. P.; Stowe, R. A.; Packed uniform sphere model for solids: Interstitial access opening sizes and pressure deficiencies for wetting liquids with comparison to reported experimental results. *J. Colloid Interface Sci.* **2006**, *294*, 139-150.

[120]   Juillerat, F.; Bowen, P.; Hofmann, H.; Formation and Drying of Colloidal Crystals Using Nanosized Silica Particles. *Langmuir* **2006**, *22*, 2249-2257.

[121]   Suzuki, T. M.; Yamamoto, M.; Fukumoto, K.; Akimoto, Y.; Yano, K.; Investigation of pore-size effects on base catalysis using amino-functionalized monodispersed mesoporous silica spheres as a model catalyst. *J. Catal.* **2007**, *251*, 249-257.

[122]   Pasqua, L.; Testa, F.; Aiello, R.; Cundari, S.; Nagy, J. B.; Preparation of bifunctional hybrid mesoporous silica potentially useful for drug targeting. *Microporous Mesoporous Mater.* **2007**, *103*, 166-173.

[123] Van Blaaderen, A.; Vrij, A.; Synthesis and characterization of colloidal dispersions of fluorescent, monodisperse silica spheres. *Langmuir* **1992**, *8*, 2921-2931.

[124] Ren, T.-Z.; Yuan, Z.-Y.; Su, B.-L.; Encapsulation of direct blue dye into mesoporous silica-based materials. *Colloids and Surfaces, A: Physicochemical and Engineering Aspects* **2007**, *300*, 79-87.

[125] Leon, R.; Margolese, D.; Stucky, G.; Petroff, P. M.; Nanocrystalline Ge filaments in the pores of a meso-silicate. *Physical Review B: Condensed Matter* **1995**, *52*, r2285-r2288.

[126] Abe, T.; Tachibana, Y.; Uematsu, T.; Iwamoto, M.; Preparation and characterization of Fe2O3 nanoparticles in mesoporous silicate. *J. Chem. Soc., Chem. Commun.* **1995**, 1617-1618.

[127] Srdanov, V. I.; Alxneit, I.; Stucky, G. D.; Reaves, C. M.; DenBaars, S. P.; Optical Properties of GaAs Confined in the Pores of MCM-41. *J. Phys. Chem. B* **1998**, *102*, 3341-3344.

[128] Pathak, S.; Cao, E.; Davidson, M. C.; Jin, S.; Silva, G. A.; Quantum Dot Applications to Neuroscience: New Tools for Probing Neurons and Glia. *J. Neurosci.* **2006**, *26*, 1893-1895.

[129] Li, C. L.; Murase, N.; Synthesis of Highly Luminescent Glasses Incorporating CdTe Nanocrystals through Sol-Gel Processing. *Langmuir* **2004**, *20*, 1-4.

[130] O'Regan, B.; Gratzel, M.; A low-cost, high-efficiency solar cell based on dye-sensitized colloidal TiO2 films. *Nature* **1991**, *353*, 737-740.

[131] Kongkanand, A.; Tvrdy, K.; Takechi, K.; Kuno, M.; Kamat, P. V.; Quantum Dot Solar Cells. Tuning Photoresponse through Size and Shape Control of CdSe-TiO2 Architecture. *J. Am. Chem. Soc.* **2008**, *130*, 4007-4015.

[132] Franzl, T.; Klar, T. A.; Schietinger, S.; Rogach, A. L.; Feldmann, J.; Exciton Recycling in Graded Gap Nanocrystal Structures. *Nano Lett.* **2004**, *4*, 1599-1603.

[133] Wellmann, H.; Rathousky, J.; Wark, M.; Zukal, A.; Schulz-Ekloff, G.; Formation of CdS nanoparticles within functionalized siliceous MCM-41. *Microporous Mesoporous Mater.* **2001**, *44-45*, 419-425.

[134] Murray, C. B.; Norris, D. J.; Bawendi, M. G.; Synthesis and characterization of nearly monodisperse CdE (E = sulfur, selenium, tellurium) semiconductor nanocrystallites. *J. Am. Chem. Soc.* **1993**, *115*, 8706-8715.

[135] Grün, M.; Lauer, I.; Unger, K. K.; The synthesis of micrometer- and submicrometer-size spheres of ordered mesoporous oxide MCM-41. *Adv. Mater. (Weinheim, Ger.)* **1997**, *9*, 254-257.

[136] Melian-Cabrera, I.; Kapteijn, F.; Moulijn, J. A.; Room temperature detemplation of zeolites through H2O2-mediated oxidation. *Chem. Commun. (Cambridge, U. K.)* **2005**, 2744-2746.

[137] Chen, X.; Mao, S. S.; Synthesis of titanium dioxide (TiO2) nanomaterials. *J. Nanosci. Nanotechnol.* **2006**, *6*, 906-925.

[138] Cabrera, S.; ElHaskouri, J.; BeltranPorter, A.; BeltranPorter, D.; Marcos, M. D.; Amoros, P.; Enhanced surface area in thermally stable pure mesoporous TiO2. *Solid State Sci.* **2000**, *2*, 513-518.

[139] Abramson, S.; Lasperas, M.; Brunel, D.; Design of mesoporous aluminosilicates supported (1R ;2S)-(-)-ephedrine: evidence for the main factors influencing catalytic activity in the enantioselective alkylation of benzaldehyde with diethylzinc. *Tetrahedron: Asymmetry* **2002**, *13*, 357-367.

[140] Peng, T.; Zhao, D.; Dai, K.; Shi, W.; Hirao, K.; Synthesis of Titanium Dioxide Nanoparticles with Mesoporous Anatase Wall and High Photocatalytic Activity. *J. Phys. Chem. B* **2005**, *109*, 4947-4952.

[141] Chen, H.; Dai, K.; Peng, T.; Yang, H.; Zhao, D.; Synthesis of thermally stable mesoporous titania nanoparticles via amine surfactant-mediated templating method. *Mater. Chem. Phys.* **2006**, *96*, 176-181.

[142] Soler-Illia, G.; Louis, A.; Sanchez, C.; Synthesis and characterization of mesostructured titania-based materials through evaporation-induced self-assembly. *Chem. Mater.* **2002**, *14*, 750-759.

[143]   Cassiers, K.; Linssen, T.; Meynen, V.; Voort, P. V. D.; Cool, P.; Vansant, E. F.; A new strategy towards ultra stable mesoporous titania with nanosized anatase walls. *Chem. Commun. (Cambridge, U. K.)* **2003**, 1178-1179.

[144]   Grosso, D.; Soler-Illia, G.; Babonneau, F.; Sanchez, C.; Albouy, P. A.; Brunet-Bruneau, A.; Balkenende, A. R.; Highly organized mesoporous titania thin films showing mono-oriented 2D hexagonal channels. *Adv. Mater. (Weinheim, Ger.)* **2001**, *13*, 1085.

[145]   Yusuf, M. M.; Imai, H.; Hirashima, H.; Preparation of mesoporous titania by templating with polymer and surfactant and its characterization. *J. Sol-Gel Sci. Technol.* **2003**, *28*, 97-104.

[146]   Shibata, H.; Ogura, T.; Mukai, T.; Ohkubo, T.; Sakai, H.; Abe, M.; Direct Synthesis of Mesoporous Titania Particles Having a Crystalline Wall. *J. Am. Chem. Soc.* **2005**, *127*, 16396-16397.

[147]   Matijevic, E.; Budnik, M.; Meites, L.; Preparation and mechanism of formation of titanium dioxide hydrosols of narrow size distribution. *J. Colloid Interface Sci.* **1977**, *61*, 302-311.

[148]   Jinsoo Kim, K.-C. S., Oliver Wilhelm, Sotiris E. Pratsinis,; Sol-Gel Synthesis and Spray Granulation of Porous Titania Powder. *Chem. Ing. Tech.* **2001**, *73*, 461-468.

[149]   Deshpande, S. B.; Potdar, H. S.; Khollam, Y. B.; Patil, K. R.; Pasricha, R.; Jacob, N. E.; Room temperature synthesis of mesoporous aggregates of anatase TiO2 nanoparticles. *Mater. Chem. Phys.* **2006**, *97*, 207-212.

[150]   Benkstein, K. D.; Semancik, S.; Mesoporous nanoparticle TiO2 thin films for conductometric gas sensing on microhotplate platforms. *Sens. Actuators, B* **2006**, *113*, 445-453.

Persönliche Daten

Name   Johannes Georg Kobler

Geboren   am 29.12.1978 in München

Studium

seit 11/2004   Promotion an Ludwig-Maximilians-Universität München im Arbeitskreis

von Prof. Bein: Thin Films from Porous Nanoparticles

03/2004 – 09/2004   Diplomarbeit in physikalischer Chemie an der Ludwig-
                                  Maximilians-Universität München im Arbeitskreis von
                                  Prof. Bein: Kolloidale Lösungen mesoporöser Silica-
                                  Nanopartikel mit funktionalisierter Oberfläche

02/2004   Diplomhauptprüfung an der Ludwig-Maximilians-
                                  Universität München

10/1999 – 02/2004   Chemie-Studium an der Ludwig-Maximilians-Universität
                                  München

Wehrdienst

07/1998 – 04/1999   Gebirgsjägerbatallion 231, Bad Reichenhall

Schulausbildung

09/1989 – 06/1998   Maximilian-von-Montgelas   Gymnasium   Vilsbiburg

Publications and Poster Presentations

Publications

1.   K. Moeller, J. Kobler, T. Bein, *Colloidal Suspensions of Nanometer-Sized Mesoporous Silica*, Adv. Funct. Mater., **2007**, *17*, 605-612.

2.   K. Moeller, J. Kobler, T. Bein, Colloidal Suspensions of Mercapto-Functionalized Nanosized Mesoporous Silica, J. Mater. Chem., **2007**, 17, 624-631.

3.   J. Kobler, K. Moeller, T. Bein, Colloidal Suspensions of Functionalized Mesoporous Silica Nanoparticles, ACS Nano, **2008**, 2, 791-799.

4.   J. Kobler, H. Abrevaya, S. Mintova, T. Bein, *High-Silica Zeolite-β: From Stable Colloidal Suspensions to Thin Films*, J. Phys. Chem. C, **2008**, *112*, 14274–14280.

5.   J. Kobler, T. Bein, Porous Thin Films of Functionalized Mesoporous Silica Nanoparticles, ACS Nano, **2008**, 2, 2324–2330.

6.   J. Kobler, B. Lotsch, G. Ozin, T. Bein, Vapor-Sensitive Bragg Mirrors and Optical Isotherms from Mesoporous Nanoparticle Suspensions, submitted.

Poster Presentations

1.   J. Kobler, K. Moeller, T. Bein, *Colloidal Functionalized Mesoporous Silica*, 17. Deutsche Zeolithtagung, **2005**, Giessen, Germany.

2.   J. Kobler, S. Mintova, T. Bein *Films of Pure-Silica Zeolites*, 3. International FEZA Conference, **2005**, Prague, Czech Republic.

3.   J. Kobler, S. Mintova, T. Bein, *Thin Microporous Films with Variable Optical Properties*, Catalytic processes on advanced micro- and mesoporous materials, **2005**, Nessebar, Bulgaria.

4.   J. Kobler, T. Bein, *Transparent Sols of Mesoporous Silica Nanoparticles*, 19. Deutsche Zeolithtagung, **2007**, Leipzig, Germany.

5.   M. Hallermann, D. Georgiadou, J. Kobler, D. Fattakhova-Rohlfing, A. Susha, T. Bein, *Electron Transfer Processes in the Electrochemical Solar Cell – Comparison of Dye and Dot Sensitized Titania*, **2007**, CeNS Winterschool, Mauterndorf, Austria.

6.   J. Kobler, T. Bein, *Transparent Sols of Mesoporous Silica Nanoparticles for the Preparation of Thin Films for Chemical Sensors*, Catalytic processes on advanced micro- and mesoporous materials, **2007**, Varna, Bulgaria.